

UNIVERSITY OF THE WITWATERSRAND

DOCTORAL THESIS

Multi-wavelength emissions from dark matter annihilation processes in galaxy clusters using cosmological simulations

Author:

Remudin Reshid MEKURIA

Supervisors:

Prof. Sergio COLAFRANCESCO

Prof. Andreas FALTENBACHER

*A thesis submitted in fulfilment of the requirements
for the degree of Doctor of Philosophy*

in the

SKA Chair Research Group
School of Physics

July 2017



Declaration of Authorship

I, Remudin Reshid MEKURIA, declare that this thesis titled, 'Multi-wavelength emissions from dark matter annihilation processes in galaxy clusters using cosmological simulations' and the work presented in it are my own. I confirm that:

- This work was done wholly or mainly while in candidature for a research degree at this University.
- Where any part of this thesis has previously been submitted for a degree or any other qualification at this University or any other institution, this has been clearly stated.
- Where I have consulted the published work of others, this is always clearly attributed.
- Where I have quoted from the work of others, the source is always given. With the exception of such quotations, this thesis is entirely my own work.
- I have acknowledged all main sources of help.
- Where the thesis is based on work done by myself jointly with others, I have made clear exactly what was done by others and what I have contributed myself.

Signed:



Date: July 05, 2017

“Look deep into nature, and then you will understand everything better.”

Albert Einstein

UNIVERSITY OF THE WITWATERSRAND

Abstract

Science Faculty
School of Physics

Doctor of Philosophy

Multi-wavelength emissions from dark matter annihilation processes in galaxy clusters using cosmological simulations

by Remudin Reshid MEKURIA

Based on the Marenostrum-MultiDark Simulation of galaxy Clusters (MUSIC) we develop semi-analytical models which provide multi-wavelength emission maps generated by dark matter (DM) annihilation processes in galaxy clusters and their sub-halos. We focus on radio and gamma-ray emission maps from neutralino DM annihilation processes testing two different neutralino masses, $M_\chi = 35$ GeV and 60 GeV along with two different models of the magnetic fields. A comparison of the radio flux densities from our DM annihilation model with the observed diffuse radio emission from the Coma cluster shows that they are of the same order of magnitude. We determine the DM densities with a Smoothed Particle Hydrodynamics (SPH) kernel. This enables us to integrate the DM annihilation signal along any given line-of-sight through the volume of the cluster. In particular it allows us to investigate the contribution of sub-halos to the DM annihilation signal with very high resolution. Zooming in on a subset of high mass-to-light ratio (M/L) DM sub-halos, i.e. DM sub-halos with very low baryon content, we demonstrate that such targets can generate prominent annihilation signals. The radial distribution of high M/L DM sub-halos is more strongly peaked at $R_{200\text{crit}} \approx 1$ compared to the distribution of all sub-halos which may suggest that the search for DM annihilation signals from sub-halos in clusters is most promising at $R_{200\text{crit}}$. The radio flux densities from DM sub-halos are well within the sensitivity limit of the Square Kilometer Array (SKA) with an integration time of 1000 hours, and unlike clusters their gamma-ray spectrum is seen to be dominated by pion decay over a wide range of gamma-ray energies. Our model makes clear predictions for future radio and gamma-ray observations of the DM annihilation signals in clusters and their sub-halos.

Acknowledgements

Firstly, I would like to express my sincere gratitude to my PhD research supervisors Prof. Sergio Colafrancesco and Prof. Andreas Faltenbacher for the continuous guidance, motivation and great support they provided me through out my PhD study over the last three years.

I would like to thank: the Wits School of Physics for hosting me in this nice research environment and for answering to my problems during the last three years; to my friends and colleagues at wits whom I can not finish listing here such as, Paolo, Suleyman Abi (zigana), Ali Abi, Abdullah Abi, Nebiha, Amare, Khaled, Tahir Abi (haji fishfish), Fatih Abi, Geoff, Claudio, Ayman, Asha, Jeffery, Emirrete, Matthew, Siphiwe, Charles, Jemal, Brehanu, Dave, Ali, Peri (John), Dereje and many others for creating a very conducive work environment and for being very nice to me and for treating me with kindness in many occasions.

With out my family and relatives support this would have been impossible, in this regard I am very thankful to my wife Inat (Workinesh) for being great mother and father to my kids Sena and Segni during my long absence from home. Thank you Imaye and Abaye (my mother and my father) your prayers has always kept me tight and neat, thank you my brother (Remedan) and sisters (Rehima, Rawuda and Remla (shutuni)) and all my relatives for supporting me spiritually throughout writing this thesis and in life in general.

Last but not least, I would like to acknowledge the South African Research Chairs Initiative of the Department of Science and Technology and National Research Foundation of South Africa for the financial support and Prof. Gustvo Yepes for providing raw data of MUSIC clusters simulation.

Contents

Declaration of Authorship	i
Abstract	iii
Acknowledgements	iv
Contents	v
List of Figures	viii
List of Tables	xiii
Abbreviations	xiv
Physical Constants	xv
Symbols	xvi
1 Standard Model of Cosmology: A Brief Review	1
1.1 Introduction	1
1.2 The Concordance Model	3
1.2.1 Cosmological Equations	3
1.3 Supporting Evidences to the Concordance Model	5
1.3.1 Cosmic Expansion and Redshift	5
1.3.2 The Cosmic Microwave Background Radiation	7
1.3.3 The Big Bang Nucleosynthesis (BBN)	7
1.4 Limitations of the Standard Model of Cosmology	9
1.4.1 The Flatness Problem	10
1.4.2 The Horizon Problem	10
1.5 Additions to the Standard Model of Cosmology	11
1.5.1 Solutions Provided by Inflation	11
1.5.2 Dark Matter	11
1.5.3 Dark Energy	12
2 Dark Matter in Modern Cosmology	14

2.1	Introduction	14
2.2	The DM Problem	15
2.2.1	DM in Galaxies	15
2.2.2	DM in Galaxy Clusters	15
2.2.3	DM Through Gravitational Lensing	18
2.3	Basic Properties of DM	19
2.4	DM Candidates	20
2.4.1	Neutrinos	21
2.4.2	Axions	21
2.4.3	Weakly Interacting Massive Particles	21
2.5	DM Detection strategies	23
2.5.1	Particle Colliders	24
2.5.2	Direct Detection Strategies	26
2.5.3	Indirect Detection Strategies	26
2.6	Summary	30
3	Galaxy Clusters in Modern Cosmology	32
3.1	Introduction	32
3.2	Formation and Evolution of Galaxy Clusters	33
3.3	Multi-wavelength Properties of Galaxy Clusters	36
3.3.1	Optical Properties	36
3.3.2	X-Ray Properties	37
3.3.3	Radio Properties	39
3.3.4	Magnetic Fields	40
3.3.5	Gravitational Lensing	41
3.3.6	Gamma-ray Properties	42
3.3.7	Extreme Ultra-Violet	43
3.3.8	Hard X-ray Emission	43
3.3.9	Sunyaev Zeldovich Effect	44
3.4	Origin of Radio Halos in Galaxy Clusters	45
3.4.1	Primary Electrons	45
3.4.2	Re-accelerated Electrons	46
3.4.3	Secondary Electrons	47
3.4.4	Secondary Electrons from DM Annihilation Process	48
3.5	Summary	51
4	Modeling Multi-wavelength Emissions from DM Annihilation Processes	53
4.1	Introduction	53
4.2	MultiDark Simulation of galaxy Clusters	54
4.3	The DM Density Square Maps	55
4.4	Magnetic Field Models	56
4.5	Electrons Equilibrium Spectra	58
4.5.1	Synchrotron Emission Processes	59
4.5.2	Gamma-ray Emission Processes	60
4.6	Summary	62

5 Multi-wavelength Emission from DM Annihilation Processes in Galaxy Clusters	63
5.1 Introduction	63
5.2 Radio Emission from DM Annihilation Processes in Galaxy Clusters . . .	63
5.3 Gamma-ray Emissions from DM Annihilation Processes in Galaxy Clusters	69
5.4 Summary	73
6 Statistical Studies and Multi-wavelength Emissions from DM Annihilation Processes in DM Dominated Sub-halos	74
6.1 Introduction	74
6.2 Statistical Study of High M/L DM Sub-halos	76
6.3 Representative Samples of High M/L DM Sub-halos	78
6.4 High M/L Sub-halos and the Radio Emission from DM Annihilation Processes.	79
6.5 High M/L Sub-halos and the Gamma-ray Emission from DM Annihilation Processes.	81
6.6 Summary	83
7 Concluding Remarks	85
Appendix A	87
Appendix B	88
Appendix C	89
Appendix D	91
Bibliography	92

List of Figures

1.1	Hubble's plot, showing correlation between the recession velocity and distance. In this case, the galaxy distances have been determined using Cepheid variable stars as standard candles (Freedman et al., 2001).	6
1.2	Spectrum of the Cosmic Microwave Background Radiation as measured by the FIRAS instrument on COBE and a black body curve for $T = 2.7277K$. Note, the error flags have been enlarged by a factor of 400. Any distortions from the Planck curve are less than 0.005% (Fixsen et al., 1996).	8
1.3	The CMB temperature fluctuations observed with Planck over the full sky.	8
1.4	Predicted abundances of 4He (mass fraction), D , 3He , and 7Li (relative to hydrogen) as a function of the baryon density. The width of the bands indicates the uncertainty in the predictions. The vertical bands show the range compatible with observations of which the broader ones denote the concordance interval based upon all four light elements. The narrower, darker band highlights the determination of the baryon density based upon a measurement of the primordial abundance of the most sensitive of these deuterium (Burles and Tytler (1998a); Burles and Tytler (1998b)), which implies $\Omega_B h^2 = 0.02 \pm 0.002$ [Image Credit: Turner and Tyson (1999)].	9
1.5	Magnitude vs redshift result of supernovae type Ia observation (Riess et al. (1998), Perlmutter et al. (1999)).	13
2.1	The observed rotational speed of M33 galaxy in comparison with what is expected from its luminous disk (Roy, 2000).	16
2.2	The temperature map of the Coma cluster (Watanabe et al., 1999).	17
2.3	Multiple image of galaxy due to strong gravitational lensing.	19
2.4	Graphical representation of gravitational lensing process (Luković et al., 2014).	20
2.5	The comoving number density Y (left) and resulting thermal relic density (right) of a 100 GeV, P-wave annihilating DM particle as a function of temperature T (bottom) and time t (top). The solid contour is for an annihilation cross section that yields the correct relic density, and the shaded regions are for cross sections that differ by 10, 10^2 , and 10^3 from this value. The dashed contour is the number density of a particle that remains in thermal equilibrium (Feng, 2010).	23
2.6	Schematic representation of the possible DM detection channels Marrodán Undagoitia and Rauch (2016). The DM and the standard model particles are denoted by χ and P	24
2.7	Constraints in the (m_χ, Ω_χ) plane from the LHC and the International Linear Collider, and from the WMAP (Baltz et al., 2006) and Planck satellites (Feng, 2005).	25

2.8	Overview of signal indications and exclusion limits from various experiments for spin-independent WIMP-nucleon cross-section for low WIMP masses (left) and high WIMP masses (left) (Marrodán Undagoitia and Rauch, 2016).	27
2.9	Figure from Beck and Colafrancesco (2016) showing the annihilation cross-section constraints from Planck (blue) and Fermi-LAT (yellow). As well as regions favored by positron excesses (green) and GC γ -ray excesses (red). f_{eff} refers to the DM annihilation energy deposition efficiency factor (note that $b\bar{b}$ and $\tau^+\tau^-$ annihilation channels have $f_{eff} \sim 0.2 - 0.3$).	28
2.10	Constraints on WIMP DM models from selected indirect search analyses for annihilation to $b\bar{b}$. Gamma-ray constraints are shown from a H.E.S.S. analysis of the Galactic Center (GC) halo, together with various analyses of Fermi LAT data. Also constraints obtained using radio observations of the GC and constraints from the PAMELA anti-proton data are shown in this figure which is taken from Gaskins (2016).	29
3.1	Large-scale structure in the universe traced by bright galaxies: a 2-D slice through our universe showing galaxies up to two billion light years away, where each dot represents a galaxy. Credit: M. Blanton and the Sloan Digital Sky Survey.	33
3.2	A 3D visualisation of non-linear structure formation from the Millennium Simulation at redshift $z = 0.0$. Credit: Max Planck Institute for Astrophysics.	35
3.3	Central part of the Coma cluster in optical band showing a pronounced central concentration of galaxies. Image Credit: NASA/SDSS.	37
3.4	The Coma cluster in X-ray band showing the bright central region occupied by the X-ray emitting hot gas. Image Credit: MPE.	37
3.5	Image of radio halo and relic of the Coma cluster taken from Brown and Rudnick (2011). This is a GBT total intensity image with all NVSS emission subtracted out (see Brown and Rudnick, 2011, for detail.).	40
3.6	Composite image showing the distribution of matter in the Bullet Cluster.	42
3.7	A plot of the life time of electrons as a function of their energy, for magnetic field $B = 1 \mu\text{G}$ and an electron density of $n_e = 10^{-3} \text{ cm}^{-3}$ (solid curve) and with $B = 5 \mu\text{G}$ (dashed curve) as well as updated $n_e = 10^{-4} \text{ cm}^{-3}$ (dot-dashed curve) taken from Sarazin (1999).	46
3.8	The observed radio halo spectrum of the Coma cluster (Thierbach et al., 2003).	50
3.9	Comparison of the observed spectrum of the Coma Cluster with the best fits of DM model by Colafrancesco et al. (2011a).	51
4.1	Graphical representation of multi-wavelength emission from neutralino annihilation processes (Colafrancesco et al., 2006).	54
4.2	The density profile of DM, gas and stars in red, green and blue, respectively.	56
4.3	The DM density square map of one representative sample of clusters obtained using SPH kernel.	57
4.4	Magnetic field profiles of the two magnetic field models: Model A and Model B are shown in red dotted line and green solid line, respectively.	58
5.1	Radio emission map at 110 MHz using magnetic field of Model A and neutralino mass of 60 GeV.	64

5.2	Radio emission map at 1.4 GHz using magnetic field of Model A and neutralino mass of 60 GeV.	64
5.3	Flux profiles at 110 MHz (solid lines) and 1.4 GHz frequencies (dotted lines) obtained using magnetic field Model A (in red color) and Model B (in dark color) for neutralino mass of 60 GeV.	65
5.4	Radio emission map at 110 MHz with SKA-low sensitivity using magnetic field of Model A and neutralino mass of 60 GeV.	65
5.5	Radio emission map at 1.4 GHz with SKA-mid sensitivity using magnetic field of Model A and neutralino mass of 60 GeV.	65
5.6	Radio emission map at 110 MHz using magnetic field of Model B and neutralino mass of 60 GeV.	66
5.7	Radio emission map at 1.4 GHz using magnetic field of Model B and neutralino mass of 60 GeV.	66
5.8	Radio emission map at 110 MHz with SKA-low sensitivity using magnetic field of Model B and neutralino mass of 60 GeV.	66
5.9	Radio emission map at 1.4 GHz with SKA-mid sensitivity using magnetic field of Model B and neutralino mass of 60 GeV.	66
5.10	Flux density from synchrotron emission, taking mass of neutralino 60 GeV, with magnetic field Model A in red color and Model B in cyan color. The blue data points are the observational data of radio emission of Coma cluster from Thierbach et al. (2003).	67
5.11	Flux density from synchrotron emission is compared with measured result of Thierbach et al. (2003), taking mass of neutralino 60 GeV, dotted lines and 35 GeV, solid lines. Magnetic field models used are indicated in red and cyan color for Model A and B, respectively.	68
5.12	Flux density of synchrotron emission process for neutralino mass of 35 GeV (solid lines) is compared with observational result of the Coma Cluster (blue data points) from Thierbach et al. (2003). Magnetic field models used are indicated in cyan, magenta and red colors for Model A, Model B, and Model B constrained, respectively.	70
5.13	Gamma-ray from non-thermal bremsstrahlung process at 100 MeV using radially varying thermal electron density from reference Sembolini et al. (2013) in units of $\langle \sigma V \rangle$	71
5.14	Gamma-ray from non-thermal bremsstrahlung process at 100 MeV using a constant average thermal electron density of the Coma Cluster. We have produced this emission map only for comparison.	71
5.15	Gamma-ray from pion decay processes at 100 MeV in units of $\langle \sigma V \rangle$	71
5.16	Gamma-ray emission from IC scattering process at 100 MeV in unit of $10^{-10} \langle \sigma V \rangle$	71
5.17	Gamma-ray from pion decay processes at 1 GeV in unit on the relic cross-section	72
5.18	Gamma-ray from pion decay processes at 10 GeV in unit on the relic cross-section.	72
5.19	Differential gamma-ray flux densities from pion decay, non-thermal bremsstrahlung and IC scattering processes is given in the plot with blue, green and pink colors, respectively.	72
6.1	Identifying the DM sub-halos filled black dots on the top of the synchrotron emission.	75

6.2	Synchrotron emission map at 110 MHz for the DM dominated sub-halo indicated by the arrow in Fig. 6.1.	75
6.3	Radio flux density from the DM dominated sub-halo indicated by the arrow in Fig. 6.1 is compared with the host cluster and observational data of the Coma Cluster.	76
6.4	Slope comparison of the flux density for synchrotron emission of the best DM dominated halo with the host cluster and observational data of the Coma Cluster.	76
6.5	Scatter plot of DM sub-halos based on M/L and the ratio of their radial distance (R) to radius of their clusters (R ₂₀₀ or R _{200crit}).	77
6.6	Scatter plot DM sub-halos based on M/L and star mass.	77
6.7	Scatter plot of DM sub-halos based on the star mass at M/L of 50.	77
6.8	Scatter plot of DM sub-halos based on the star mass at M/L of 100.	77
6.9	The probability distribution function of sub-halos based on their M/L at a relative distance r (R/R _{200crit}), the ratio of distances of each sub-halo from the center of the host cluster to the radius of the host cluster at 200 times the critical density of the Universe. Sub-halos with M/L above 1, 50 and 100 are shown in blue, green and red color, respectively.	78
6.10	Synchrotron emission map of DM sub-halo 1 at 110 MHz.	79
6.11	Synchrotron emission map of DM sub-halo 2 at 110 MHz.	79
6.12	Synchrotron emission map of DM sub-halo 3 at 110 MHz.	80
6.13	Synchrotron emission map of DM sub-halo 4 at 110 MHz.	80
6.14	Comparison of the radio flux density of DM sub-halo 1 and 2 (Halo ID 03108 and 02569) and their spectral features with observational data of the Coma Cluster.	80
6.15	Comparison of the radio flux density of DM sub-halo 3, 4 and 5 (Halo ID 01714, 00824 and 02783) and their spectral features with observational data of the Coma Cluster.	80
6.16	The radio flux densities of the five high M/L DM sub-halos.	81
6.17	Scaled comparison of spectral feature of the five DM sub-halos with observational data of the Coma Cluster.	81
6.18	Gamma-ray emission map from pion decay at 100 MeV for DM sub-halo 1.	82
6.19	Gamma-ray emission map from pion decay at 100 MeV for DM sub-halo 2.	82
6.20	Gamma-ray emission map from pion decay at 100 MeV for DM sub-halo 3.	82
6.21	Gamma-ray emission map from pion decay at 100 MeV for DM sub-halo 4.	82
6.22	Gamma-ray emission map from pion decay process at 100 MeV for DM sub-halo 5.	83
6.23	Gamma-ray emission map from non-thermal bremsstrahlung process at 100 MeV for DM sub-halo 5.	83
6.24	Differential gamma-ray flux densities of the five high M/L DM sub-halos from pion decay and non-thermal bremsstrahlung processes.	84
A.1	Radio emission map at 110 MHz using magnetic field of Model A for DM model 35 GeV.	87
A.2	Radio emission map at 1400 MHz using magnetic field of Model A for DM model 35 GeV.	87
A.3	Radio emission map at 110 MHz using magnetic field of Model B for DM model 35 GeV.	87

A.4	Radio emission map at 1400 MHz using magnetic field of Model B for DM model 35 GeV.	87
C.1	DM density square of DM sub-halo 1 integrated along the line-of-sight.	89
C.2	Gas density square of DM sub-halo 1 integrated along the line-of-sight.	89
C.3	DM density square of DM sub-halo 2 integrated along the line-of-sight.	89
C.4	Gas density square of DM sub-halo 2 integrated along the line-of-sight.	89
C.5	DM density square of DM sub-halo 3 integrated along the line-of-sight.	90
C.6	Gas density square of DM sub-halo 3 integrated along the line-of-sight.	90
C.7	DM density square of DM sub-halo 4 integrated along the line-of-sight.	90
C.8	Gas density square of DM sub-halo 4 integrated along the line-of-sight.	90
D.1	Gamma-ray emission map from non-thermal bremsstrahlung process at 100 MeV for DM sub-halo 1.	91
D.2	Gamma-ray emission map from non-thermal bremsstrahlung process at 100 MeV for DM sub-halo 2.	91
D.3	Gamma-ray emission map from non-thermal bremsstrahlung process at 100 MeV for DM sub-halo 3.	91
D.4	Gamma-ray emission map from non-thermal bremsstrahlung process at 100 MeV for DM sub-halo 4.	91

List of Tables

5.1	Comparison of the spectral index for radio flux densities using neutralino annihilation final product of $b\bar{b}$ species.	67
5.2	Gamma-ray upper limits set by Fermi for energies above 0.1 GeV (Ackermann et al. (2014)), 1 and 10 GeV (Ackermann et al. (2016)) and the comparison with our flux calculation using neutralino mass of 35 GeV and $b\bar{b}$ species.	73
B.1	Halo ID, maximum DM density summed along the line of sight and total mass with in 30 kpc radius for the five high M/L DM sub-halos considered in our study.	88
B.2	Halo ID, fraction of gas, star and DM in the halo with in 30 kpc radius, and radial distance from the center of the cluster for the five high M/L DM sub-halos considered in our study.	88

Abbreviations

MUSIC	Marenostrum-MultiDark SI mulation of galaxy Clusters
SPH	Smoothed P article H ydrodynamics
MACHOs	M Assive C ompact H alo O bjects
BBN	Big B ang Nucleosynthesis
DM	Dark M atter
WIMPSs	Weakly Interacting Massive P articles
IC scattering	Inverse C ompton scattering
SM	S tandard M odel
ICM	Intra C luster M edium
CDM	Cold D ark M atter
HDM	Hot D ark M atter
HXR	Hard X - R ay
SZ effect	Sunyaev Z el'dovich effect
RM	Rotation M easure
SKA	Square K ilometer A rray
MHD	Magneto H ydro D ynamics

Physical Constants

Speed of Light	c	$= 2.997\ 924\ 58 \times 10^8\ \text{m s}^{-2}$
Mass of an Electron	m_e	$= 9.10938356 \times 10^{-28}\ \text{g}$
Mass of a Proton	m_p	$= 1.67262178 \times 10^{-24}\ \text{g}$
Mass of the Sun	M_\odot	$= 1.99 \times 10^{33}\ \text{g}$
Kiloparsec	kpc	$= 3.08568025 \times 10^{21}\ \text{cm}$
Planck's Constant	h	$= 6.6261 \times 10^{-27}\ \text{cm}^2\ \text{g s}^{-1}$
Boltzmann Constant	k	$= 1.3806505 \times 10^{-23}\ \text{J K}^{-1}$
Thomson Cross-section	σ_t	$= 6.652 \times 10^{-25}\ \text{cm}^2$
Classical Radius of an Electron	r_0	$= 2.82 \times 10^{-13}\ \text{cm}$

Symbols

S_{synch}	Radio Flux	Jy
$\frac{dF}{dE}$	Differential Flux	ph. cm ⁻² s ⁻¹ GeV ⁻¹
M_χ	Neutralino's or DM Mass	GeV
ρ_{DM}	DM Density	M_\odot kpc ⁻³
ρ_{GAS}	Gas Density	M_\odot kpc ⁻³
n_{el}	Number Density of Electrons	cm ⁻³
B	Magnetic Field	μ G
T_0	CMB Temperature	2.728 K
D_L	Luminosity Distance of the Coma Cluster	96000 kpc
Y_{He}	Helium Fraction	0.25
z	Redshift of Coma Cluster	0.028
$\nu_0 = 2.8 \times 10^{-6} \mathbf{B}$	Gyro-frequency	MHz
$\nu_p = 8980 \times 10^{-6} (n_{el})^{0.5}$	Plasma-frequency	MHz

*To my father Reshid Mekuria Negesso and my mother Kedija
Ebisso Dekebo*

Chapter 1

Standard Model of Cosmology: A Brief Review

Readers which are familiar with the Standard Model of Cosmology can proceed to Chapter [2](#).

1.1 Introduction

Cosmology is the study of the Universe which attempts to make sense of the large-scale nature of the material world around us using scientific methods. It thus tries to provide answers to fundamental questions such as: How and when did the Universe originate? How is it evolving? What will be its fate? etc.

A scientific based search for answers to such fundamental questions led to the development of the current standard model for the Universe called the “Hot Big Bang” model. According to the “Hot Big Bang” model the whole Universe was once in the form of a singularity, this being an extremely hot and dense state which evolve into a cool and tenuous state as a result of expansion that is still going on today.

Before the advent of this model, just a century ago, many scientists believed that the Universe was infinite and eternal and it was not apparent whether the Milky Way was the only large collection of stars in the Universe. A revolution in our understanding happened when Edwin Hubble measured the distance of the Andromeda Galaxy providing evidence that our galaxy is among many more galaxies in the Universe.

From the rate of expansion of the Universe we now know that it began roughly 14 billion years ago in the hot and dense state of the “Hot Big Bang”. Additionally, it has become evident that the Universe is comprised of some extremely interesting structures such as galaxies, clusters, superclusters, voids and great walls which we had not previously have thought about. Einstein’s theory of General Relativity (e.g., [Weinberg, 1972](#)) has provided the theoretical tools that are required to develop this model. As a result of this model we are able to explain successfully the structures visible in the Universe today back to its primeval composition when it is only fraction of a second old. In time, the attractive force of gravity acted upon very small inhomogeneities in the distribution of primordial matter and gave rise all structures we observe today.

There have been great achievements in the techniques involved in observing the Universe following tremendous subsequent advancements in the theoretical studies of the

last century. Up until a century ago, observations were limited to telescopes that operate in the optical/visible spectra. Information about the nature and environment of astronomical objects beyond our solar system were largely carried to us by photons with some contribution obtained from Cosmic rays and neutrinos. Consecutively, extending our observations beyond optical frequencies to other spectral bands was made possible using ground- and space-based modern telescopes. Information obtained through full electromagnetic spectrum, ranging from radio to gamma ray using both ground- and space-based modern telescopes provided new insights and began to reveal previously hidden structures in the Universe and made it possible to study the structure, dynamics, stellar populations and interstellar medium of external galaxies in great detail.

Significant improvements in our observations were also the fruits of remarkable technological advances. In the early days, telescopes with small collecting areas were used with photographic plates fitted onto them to take images of astronomical objects. Later on, at optical wavelengths, photographic plates were replaced with Charge Coupled Devices (CCDs) which improved the detection sensitivities by a factor 10 to 100. This has also brought great improvements in the techniques of handling and processing the data, as well as in analyzing and manipulating the output images of astronomical objects revealing many new details. Such innovative techniques combined with a great improvement in spatial resolution that was provided by the Hubble-Space-Telescope and other 10 m class telescopes opened up a golden age for cosmology.

The aforementioned improvements in technology made possible the study of very complex structures and gave insight in understanding the properties of newly discovered objects. The involved phenomena in these objects are now explained more effectively and efficiently than achieved previously. As a result of which, it was made possible to measure the tiny fluctuations (one part in 10^5) in temperature and density of the cosmic microwave background and discover galaxies and quasars to redshifts of 5 and beyond.

Observations based on supernovae measurements now give indications that the Universe is not only expanding but also its rate is accelerating. At present the most suggested cause of which is the barely known component of the universe called ‘Dark Energy’ which is sometimes referred as the cosmological constant. Cosmology enters a precision era when the cosmic microwave background (CMB) is mapped with high accuracy by WMAP. As a result of which the curvature and matter budget of the Universe were able to be determined accurately. Observations of large-scale structure put constraints on the dark matter density below critical levels, and the Hubble constant is measured with ever better accuracy and the evolution of galaxies is observed out to 1 Gyr after the Big Bang.

To date the “Hot Big Bang” model is the most acceptable model of cosmological paradigm. It beautifully explains key phenomena in the Universe providing satisfying solutions to the fundamental questions such as: How and why the Universe expands? How the CMB is originated and evolved? How the light elements were synthesized leading to the formation of the first stars and galaxies? How the large-scale structures we observe today came about? In the following sections supporting observational evidences to this standard model of cosmology, also known as the concordance model, will be presented followed by discussions on a list of its limitations and the developed additions to the model.

1.2 The Concordance Model

A leap in the development of modern cosmology came about following Einstein's celebrated work on the general theory of gravity in 1915 (e.g., [Einstein, 1915](#)). Einstein constructed the theory of gravity, based on his reasonings from his thought experiment, i.e., mass & energy are equivalent ($E = mc^2$), space and time form space-time. Hence he concluded that the source of gravity is mass/energy and it bends/warps space-time.

1.2.1 Cosmological Equations

Einstein's field equations are most commonly formulated as

$$G_{\alpha\beta} = \frac{8\pi G}{c^2} T_{\alpha\beta} + \Lambda g_{\alpha\beta}, \quad (1.1)$$

where $G_{\alpha\beta}$ is the Einstein tensors constructed from the curvature tensor, which involves the metric tensor $g_{\alpha\beta}$ and its derivatives. The description of the cosmic fluid is contained in the energy-momentum tensor ($T_{\alpha\beta}$) term. The cosmological constant Λ was originally invented and introduced by Einstein in order to allow static cosmological models as he initially accepted neither an expanding nor a contracting Universe. General relativity is non-linear, as the structure of space-time determines the motion of matter and energy, and the latter determine the structure of space-time; for this reason obtaining exact solutions to Einstein's field equation is very difficult.

The metric tensor $g_{\alpha\beta}$ has ten independent components due to its symmetry, the time-time component g_{00} , the three space-time components g_{0i} , and the six space-space components g_{ij} . The cosmological principle, which states "when averaged over sufficiently large scales the Universe is isotropic and homogeneous", is the fundamental assumption that greatly simplifies the metric. The metric of spacetime is given generally as

$$ds^2 = g_{\alpha\beta} dx^\alpha dx^\beta.$$

By introducing comoving coordinates, spatial coordinates attached to fundamental observers, the spatial hyper-surfaces can then be scaled by a function $a(t)$ which is the cosmological scale factor parameter that carries information on the relative expansion of the Universe. The metric of spacetime then reduces to

$$ds^2 = c^2 dt^2 - a^2(t) dl^2, \quad (1.2)$$

where dl is the line element for the three-space coordinates. Equation 1.2 can be reduced to the so-called Minkowski space metric for an Euclidean line element.

We have spherical symmetry implied from isotropy for which we introduce polar coordinates (r, θ, ϕ) (e.g., [Bartelmann, 2010](#)).

$$dl^2 = dr^2 + f_K^2(r)[d\theta^2 + \sin^2 \theta d\phi^2], \quad (1.3)$$

the metric expressed by the line element 1.3 is manifestly isotropic. It can be shown that the ($t = \text{constant}$) space sections are surfaces of homogeneity and have maximal symmetry: thus $f_K(r)$ can be either trigonometric, linear, or hyperbolic in r with constant

curvature

$$K = k/a^2(t), \quad (1.4)$$

where k is the sign of K (+1, 0 or -1) which represent a closed, flat or an open Universe, respectively.

The $f_K(r)$ term in its generic form can be put as

$$f_K(r) = \begin{cases} K^{-1/2} \sin(K^{1/2}r) & \text{for } K > 0 \\ r & \text{for } K = 0 \\ |K|^{-1/2} \sinh(|K|^{1/2}r) & \text{for } K < 0 \end{cases},$$

where K is a constant parameterizing the curvature of spatial hyper-surfaces as in 1.4. Using *Robertson-Walker metric* given in the equation 1.3, Einstein's equations (1.1) reduce to two differential equations:

$$\begin{aligned} \left(\frac{\dot{a}}{a}\right)^2 &= \frac{8\pi G}{3}\rho - \frac{Kc^2}{a^2} + \frac{\Lambda}{3}, \\ \frac{\ddot{a}}{a} &= \frac{-4\pi G}{3}\left(\rho + \frac{3p}{c^2}\right) + \frac{\Lambda}{3}. \end{aligned} \quad (1.5)$$

The two equations in (1.5) are called Friedmann's equations (see for e.g., Friedmann, 1922). They will determine the change in the scale factor once its reference value at a fixed instant t is chosen (common value used is at the present time, i.e., $a = 1$).

The energy density ρ evolves giving the well known conservation equation in the form

$$\dot{\rho} + 3\left(\rho + \frac{p}{c^2}\right)\frac{\dot{a}}{a} = 0, \quad (1.6)$$

where p is the pressure. The evolution of the density in terms of scale factor a can be determined with a suitable prescription of the equation of state function $\omega = p/\rho c^2$. For example, Cold Dark Matter (dust) is pressure-less and hence $\omega_d = 0$ whereas radiation has $\omega_\gamma = 1/3$. Thus according to the conservation equation one obtains

$$\rho_d \propto a^{-3} \quad \& \quad \rho_\gamma \propto a^{-4}.$$

Thus the evolution of the density of each species together with equation (1.5) in turn give us with a unique determination of the variation of scale factor a with time. The Hubble parameter can be defined as the ratio of time derivative of \dot{a} and a (i.e., $H \equiv \dot{a}/a$). Now using the critical density $\rho_c \equiv \frac{3H^2}{8\pi G}$ I can determine H at a given time by

$$\frac{H(t)}{H_0} = \left[\frac{\rho_c(t)}{\rho_c(t_0)} \right]^{1/2}, \quad (1.7)$$

where $H_0 \equiv \dot{a}_0/a_0$ is its value at t_0 . We can defining density (ρ_k) to the curvature term by

$$\rho_k \equiv -\frac{3Kc^2}{8\pi Ga^2} \implies \Omega_k = -\frac{Kc^2}{H^2 a^2}, \quad (1.8)$$

where Ω_k is the density parameter for the curvature term which is obtained by dividing ρ_k with ρ_c . The critical density ρ_c can be given as the sum of densities from all individual components i.e.,

$$\rho_c = \rho_k + \rho_m + \rho_\gamma + \rho_\Lambda,$$

where the subscripts k , m , γ , and Λ represent curvature, matter, radiation and vacuum energy, respectively. Substituting this in equation (1.7) gives:

$$\frac{H(t)}{H_0} = [\Omega_{\gamma,0}a^{-4} + \Omega_{m,0}a^{-3} + \Omega_{k,0}a^{-2} + \Omega_{\Lambda,0}]^{1/2},$$

where $\Omega_{x,0}$ represents the density parameters for species x at time t_0 . The time t can then be evaluated as

$$t = \int \frac{da}{aH} = \frac{1}{H_0} \int \frac{da}{a[\Omega_{\gamma,0}a^{-4} + \Omega_{m,0}a^{-3} + \Omega_{k,0}a^{-2} + \Omega_{\Lambda,0}]^{1/2}}. \quad (1.9)$$

As all density contributions in square brackets scale with different powers of a ; their relative importance also changes over time. For instance, in the early Universe the temperature is so high that the radiation component of the universe is dominant contributor to the over all density, however, at the present time the radiation density is much smaller than that of matter. This also imply that there has been a time t_{eq} before which radiation dominates which can be expressed alternatively by the scale factor a_{eq} , which is given by

$$a_{eq} = \frac{\Omega_{\gamma,0}}{\Omega_{m,0}}.$$

Therefor before t_{eq} the Universe is called radiation-dominated; and later matter-dominated while curvature is still negligible; finally curvature becomes important and Ω_Λ may take over. Moreover equation (1.9) can be integrated easily in a situation where we have one single species dominating the mass-energy content. In this case we obtain for radiation $a \propto t^{1/2}$; matter $a \propto t^{2/3}$; curvature $a \propto t$ and vacuum or cosmological constant $a \propto e^{Ht}$.

1.3 Supporting Evidences to the Concordance Model

In the following sub-sections I will discuss briefly the supporting observational evidences which serves as pillars to the standard cosmology theory of the Universe.

1.3.1 Cosmic Expansion and Redshift

In the year 1900 to 1910 astronomers began measuring radial speeds of galaxies by measuring Doppler shift of spectral lines expecting the radial velocities to be random (a state of rest in Milky Way). However, measured result showed radial velocities are not random. The redshift z of an object emitting a wavelength λ_e (and a frequency ν_e) and observed with wavelength λ_0 (and a corresponding frequency ν_0) is defined to be the fractional Doppler shift of its emitted light (photons) due to its radial motion. As a photon of frequency ν passes freely through space it experiences a “stretching” of its wavelength (Peebles, 1993). This stretch/increase in the wavelength or shrinking/declining in the frequency of the photon is proportional to the expansion factor from time

of photon emission (a_e) to the time of photon observation (a_o) which can be expressed as

$$\frac{\nu_e}{\nu_o} = \frac{a_o}{a_e} = 1 + z, \quad (1.10)$$

where ν_e and ν_o are the frequencies of the photon at the time of emission and observation, respectively. Thus, photon is red- or blueshifted by the same amount as the Universe expanded or shrank between emission and observation. Observation of the thermal spectrum of the CMB is the most straightforward evidence proving that cosmic expansion causes redshifts in the wavelengths of photons (Fixsen et al., 1996).

In 1929 Hubble measured distances to several galaxies using Cepheid variable stars. He discovered that the measured redshift z follows a linear dependence on the distance d between the source and us. The interpretation he gave for this redshift was the common Doppler shift caused by the relative radial motion with a radial velocity given by $v = zc$ correlated with the distance away from Earth as shown in Fig. 1.1. In fact this interpretation was later on shown to be valid only as a first approximation to (the first term of) the expression of redshift due to cosmic expansion.

Hubble's Law thus takes the form

$$v = H_0 d, \quad (1.11)$$

where $H_0 \equiv \frac{\dot{a}_0}{a_0}$ is proportionality constant relating galaxy's proper distance d and its recession velocity v . The dimensionless factor h is usually used to express the Hubble constant i.e.,

$$H_0 = 100 h \text{ km s}^{-1} \text{ Mpc}^{-1},$$

$h = 0.72 \pm 0.08$ based on the final Hubble Space Telescope Key Project. Thus, expansion

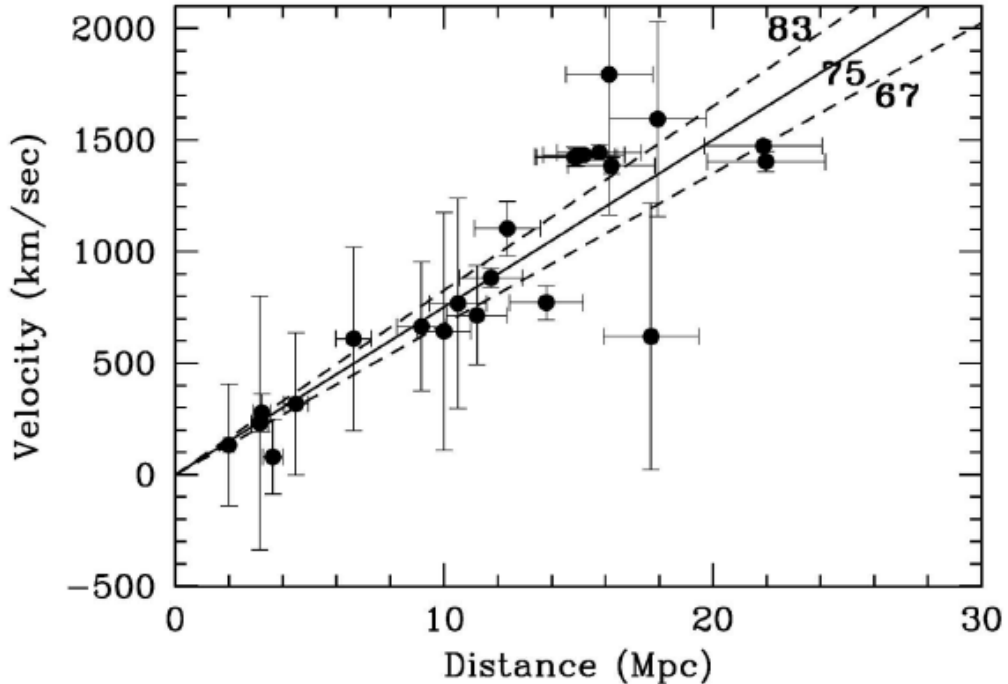


FIGURE 1.1: Hubble's plot, showing correlation between the recession velocity and distance. In this case, the galaxy distances have been determined using Cepheid variable stars as standard candles (Freedman et al., 2001).

of the Universe became an observational evidence and it is also in perfect agreement with one of the predictions of Einstein's general theory of relativity.

1.3.2 The Cosmic Microwave Background Radiation

Most of the photons of light produced by various sources in the Universe which are collectively detected on earth by various instruments or telescopes are not from stars, but from the Cosmic Microwave Background (CMB). In 1965 Penzias and Wilson detected some radiation at a microwave wavelength which was coming from all points in the sky. Initially, having failed to avoid this radiation appearing in the telescope they thought it due to some kind of defect in the instrument or faulty measurement. However, when they learnt that there has been theoretical predictions of relic radiation that should be left over from the Big Bang, it became a discovery (Penzias and Wilson, 1965).

CMB radiation is a relic radiation that is left over from the early Universe which is predicted in the “Hot Big Bang” model. It is deduced that if the Universe started from a hot and dense state, it should now be filled with radiation in the microwave range due to redshift. With an experimental measurement made outside the atmosphere of the Earth, the CMB spectrum was first measured accurately over a wide range of wavelengths by the COsmic Background Explorer (COBE) satellite, launched in 1989 (Mather et al., 1990). It showed that the CMB has nearly perfect thermal black body spectrum at a temperature of 2.7277 K (see Fig. 1.2) with a close resemblance to isotropy with tiny variations of 30 microkelvins in temperature across the sky (Fixsen et al., 1996).

The expected temperature fluctuations of anisotropy in the CMB assuming weakly interacting dark matter components are in the order of $\frac{\delta T}{T} \approx 10^{-5}$ (see for e.g., Mather et al., 1990). This value falls in the regime of microkelvins which were finally detected at the same level by COBE in 1992 (see Fig. 1.3). Further substantially improved measurements has led to a conclusion that the structures formed in the Universe that we observe today are the results of these anisotropies where the attractive force of gravity acted upon them.

1.3.3 The Big Bang Nucleosynthesis (BBN)

One very strong falsification test suggested by the “Hot Big Bang” model during the early stage of the Universe is its prediction of the big bang nucleosynthesis (BBN). It is believed that the Universe in its early stage is very hot and thus filled with very energetic photons and particles. For temperature kT higher than 1 MeV, which is roughly the amount of binding energy of a stable nuclei, bombardment by energetic photons and particles prevent stable nuclei from forming. When the Universe cools due to its expansion and reaches a temperature range of $kT \ll 1$ MeV fusion of neutrons and protons will be able to form light nuclei. The faster the expansion, the less time there is for nucleosynthesis, thus the light-element abundances measure the rate of expansion of the Universe in its early stage. Thus only few light elements (D , 3He , 4He and 7Li) form through fusion of neutrons and protons during BBN.

The calculated abundance of the light elements for example predicts that about 25% of the Universe is made of 4He (see Fig. 1.4) which agrees well with abundance obtained in current stellar observations (Sarkar, 1996). Moreover, elements heavier than 7Li

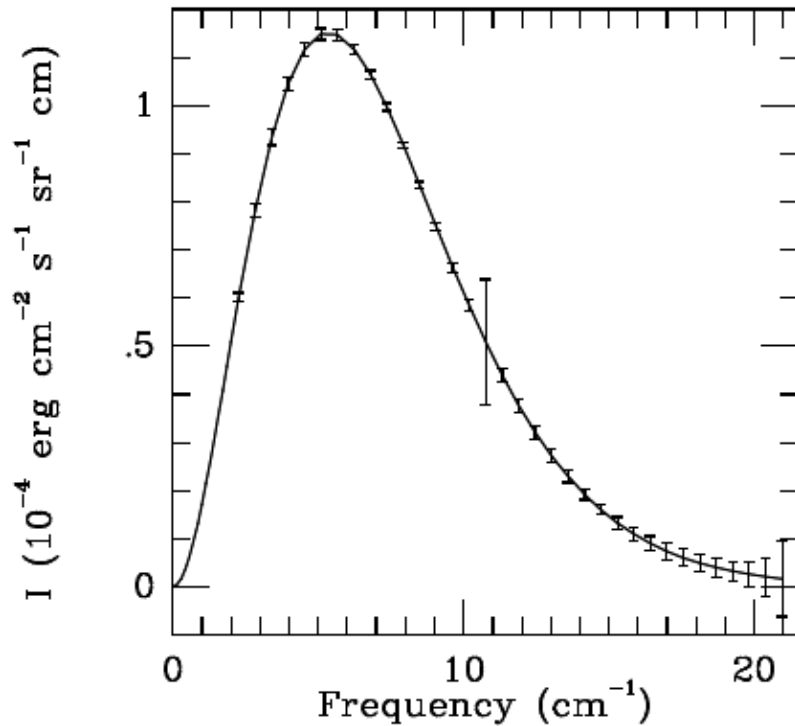


FIGURE 1.2: Spectrum of the Cosmic Microwave Background Radiation as measured by the FIRAS instrument on COBE and a black body curve for $T = 2.7277K$. Note, the error flags have been enlarged by a factor of 400. Any distortions from the Planck curve are less than 0.005% (Fixsen et al., 1996).

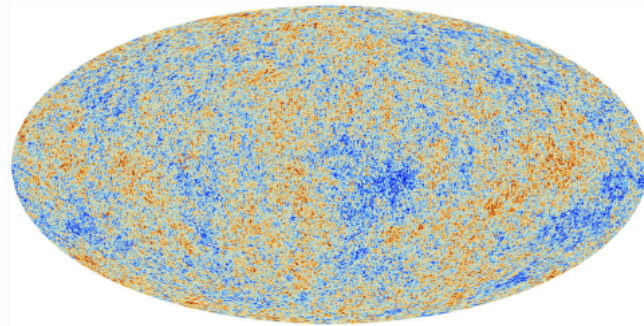


FIGURE 1.3: The CMB temperature fluctuations observed with Planck over the full sky.

are only able to be produced through nuclear burning process in stars. And much heavier elements will only be formed through neutron capture process during supernova explosions during which they shed most of their content to the inter-stellar medium.

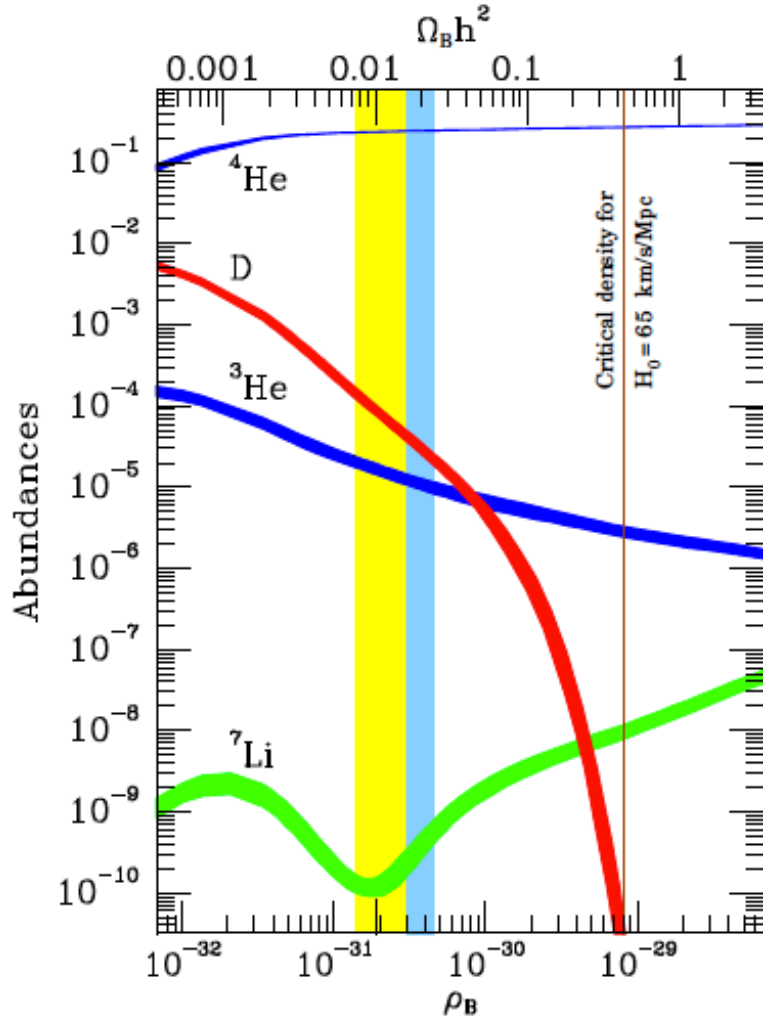


FIGURE 1.4: Predicted abundances of ^4He (mass fraction), D , ^3He , and ^7Li (relative to hydrogen) as a function of the baryon density. The width of the bands indicates the uncertainty in the predictions. The vertical bands show the range compatible with observations of which the broader ones denote the concordance interval based upon all four light elements. The narrower, darker band highlights the determination of the baryon density based upon a measurement of the primordial abundance of the most sensitive of these deuterium (Burles and Tytler (1998a); Burles and Tytler (1998b)), which implies $\Omega_B h^2 = 0.02 \pm 0.002$ [Image Credit: [Turner and Tyson \(1999\)](#)].

1.4 Limitations of the Standard Model of Cosmology

From the previous sections we have seen that the “Hot Big Bang” model successfully explains, the expansion of the Universe, the CMB radiation, the origin of light elements in the Big Bang nucleosynthesis, and a framework for understanding the formation of galaxies and large-scale structures. Hence we deduce that the “Hot Big Bang” scenario is by far the most successful cosmological paradigm among the models suggested to explain the origin of the Universe and its evolution.

However, this model also leaves many serious puzzles unanswered. Some of these puzzles have their origins in the early Universe, whereas others emerge only in late-time cosmology. In this section, I explore some of the most serious shortcomings of the standard Big Bang cosmology.

1.4.1 The Flatness Problem

Current results of type Ia supernova observations and CMB anisotropy measurements put the present day density parameter Ω_0 in the range between 0.8 and 1.2 i.e.,

$$|1 - \Omega_0| \leq 0.2. \quad (1.12)$$

If we instead consider the early stage of the Universe we obtain

$$|1 - \Omega_{rm}| \leq 2 \times 10^{-4}, \quad (1.13)$$

and

$$|1 - \Omega_{BBN}| \leq 3 \times 10^{-14}. \quad (1.14)$$

ranges for the density parameter at time of radiation-matter equality (Ω_{rm}) and BBN (Ω_{BBN}), respectively.

Eqn. (1.12) to (1.14) show that the deviation of the density parameter from unity (value on right-hand-side of these equations) gets smaller and smaller (the density parameter Ω gets closer and closer to unity). Further more, if we consider the case of Planck epoch these deviation becomes 10^{-60} . For instance had the deviation been 3×10^{-2} rather than 3×10^{-14} at the time of BBN, the Universe would have collapsed to a BigCrunch or expanded to a low-density with in only a few years time, as a result of which no object would have had time to form (Ryden, 2003). Thus we deduce that this is quite significant fine-tuning that the “Hot Big Bang” model alone does not address, and is often referred to as the flatness problem.

1.4.2 The Horizon Problem

The horizon distance during the matter-dominated stage of the Universe is given in Peacock (1996) as

$$D_{hor} \simeq \frac{6000h^{-1}}{\sqrt{\Omega(z)}} h^{-1} \text{Mpc}. \quad (1.15)$$

Thus at last scattering the particle horizon was only 100 Mpc in size and subtending an angle of 1 degree in the sky. However, this is in contradiction with the large number of causally disconnected patches subtending an angle > 1 degree we see on the CMB sky, all at the same temperature.

The question how can these two regions in the sky which are far apart from each other (> 100 Mpc) that they would not have enough time to share information with each other show similar physical properties can not be addressed with the “Hot Big Bang” model alone hence called the horizon problem.

1.5 Additions to the Standard Model of Cosmology

In the previous sub-section I have discussed the flatness and horizon problems among few other shortcomings of Standard Model of Cosmology. Now I will introduce and discuss some of the suggested solutions that have been introduced to fix this model.

1.5.1 Solutions Provided by Inflation

Inflationary model of cosmological rests on the assumption that there existed a period in the early stage of the Universe where the matter energy density was dominantly contributed by a new scalar field. This scalar field is a form of matter having negative pressure which expands the Universe outward at an accelerated rate. This great expansion is believed to last only for a brief time of order of 10^{-34} seconds. As a result of this great expansion the Universe is believed to pass through exponential growth of approximately 10^{34} times its size just before the onset of inflation.

The deviation of the density parameter at the initial ($\Omega(t_i)$) and final stage of inflation ($\Omega(t_f)$) are related by

$$|1 - \Omega(t_f)| = |1 - \Omega(t_i)| \times e^{-2N}. \quad (1.16)$$

Taking 100 e-folding of inflation ($N=100$) and considering the extreme case of curvature ($|1 - \Omega(t_i)| \sim 1$) for example will give

$$|1 - \Omega(t_f)| \sim e^{-2N} \sim e^{-200} \sim 10^{-87} \quad (1.17)$$

which leads to extreme flattening of the Universe (Ryden, 2003), which thus resolve the flatness problem (Guth, 1981). As this epoch of exponential growth causes the horizon size to grow exponentially it is also able to resolve the horizon problem. This can be understood as regions that existed prior to inflation from which the CMB photons were emitted were close enough to interact with each other. Introducing inflation thus resolve both the flatness and horizon problems, a detailed review on the inflationary theory of cosmic expansion can be found in Liddle (1999).

The other additions required to the “Hot Big Bang” model of cosmology are the “dark sectors” of the Universe called dark matter and dark energy which will be presented in the following sub-sections.

1.5.2 Dark Matter

Recent advances in precision cosmology have explored the energy and matter content of the Universe confirming that there is more mass required (“the missing mass”) which contribute to the present day density parameter of $\Omega_0 = 1$. Measurements from CMB anisotropy, analyses of large scale structure and Big Bang nucleosynthesis have enabled exact determination of not only the energy and matter content of the Universe but also its constituents. They provide that non-relativistic matter contribute roughly 30 % of the total energy budget of the Universe. And only less than 15 % of this is known to exist in the form of baryonic matter, whereas the remaining 85 % is in the form of non-baryonic dark matter (e.g., Planck Collaboration et al., 2015).

The “missing mass” problem was first pointed out by Fritz Zwicky in the 1930’s. He measured the radial velocity of a number of galaxies in the Coma cluster for which he found value of 1000 km s^{-1} (Zwicky, 1933) which is in agreement with a more recent value of 1082 km s^{-1} (Colless and Dunn, 1996). This value was very large to be obtained if the mass in the cluster were only due to the individual stars and gas content observed within its galaxies. This led him to the conclusion that there must be a large amount of “missing mass” (dark matter) in the cluster which hold the cluster together by providing sufficient amount of gravitational attraction. Subsequently similar observations in galaxies and gravitational lensing studies have also suggested the existence of dark matter.

Measurement of the temperature fluctuations in the CMB indicates anisotropies in the matter distribution of 1 part by 10^{-5} . These anisotropies are too small to account for the large scale structures we see today (Padmanabhan, 1996). It is believed that having non-baryonic dark matter allows the Universe an earlier start of structure formation than the case of having only baryonic matter which can only take effect at the recombination epoch. Moreover, if dark matter is dominantly non-relativistic, (i.e., with velocity $v \rightarrow 0$) in which case it is called “cold dark matter” (CDM). The Jeans length, λ which is the critical length attained when self gravity and pressure are in equilibrium approaches zero ($\lambda_J \rightarrow 0$), hence structures can grow on all scales compared to “hot dark matter” (HDM) models such as neutrinos where the velocity of particles is finite. For a detailed discussion of dark matter see chapter 2.

1.5.3 Dark Energy

The cosmological constant Λ given in Eqn. (1.1) was first added to the formalism of general theory of relativity by Albert Einstein to ensure a static Universe. This stationary solution obtained using “Friedmann equations” (1.5) requires Λ to be positive. However, the cosmological constant was later rejected when it was first shown, by Friedmann in 1922 (Friedmann, 1922), that this solution is unstable and rather they describe an expanding Universe. From then on the cosmological constant has been taken in and out of the cosmological equation until it was finally retained when observational evidence emerged in the 1998 from supernovae Ia observation showing the Universe is undergoing an accelerated expansion (Perlmutter et al., 1999) as shown in Fig 1.5. This acceleration in the expansion of the Universe is believed to be the result of another component of the Universe, which is unclustered and invisible form of cosmic stuff that permeates all of space, called dark energy.

The nature of dark energy and its dynamics is hardly understood at present as it is only a phenomenological addendum whose existence has not been predicted from the Big Bang as well as inflationary cosmology. The leading candidates emerging from theoretical models for dark energy are “the vacuum energy” or “quintessence”. This would be possible if the Universe is dominated by a component “fluid” which exerts a negative pressure. With a suitable representation of the equation of state as $p = \omega \rho c^2$ in the “Friedmann equations” (1.5) an accelerated expansion is obtained for $\omega < -1/3$, and the cosmological constant fulfills this relation as the new component fluid with $\omega = -1$ which is thought of as the energy associated with vacuum, the space absolutely void of particles. A more general form of this relation with $-1 < \omega < -1/3$ has been proposed to be described by “quintessence” that might cause the expansion of the Universe to accelerate with time.

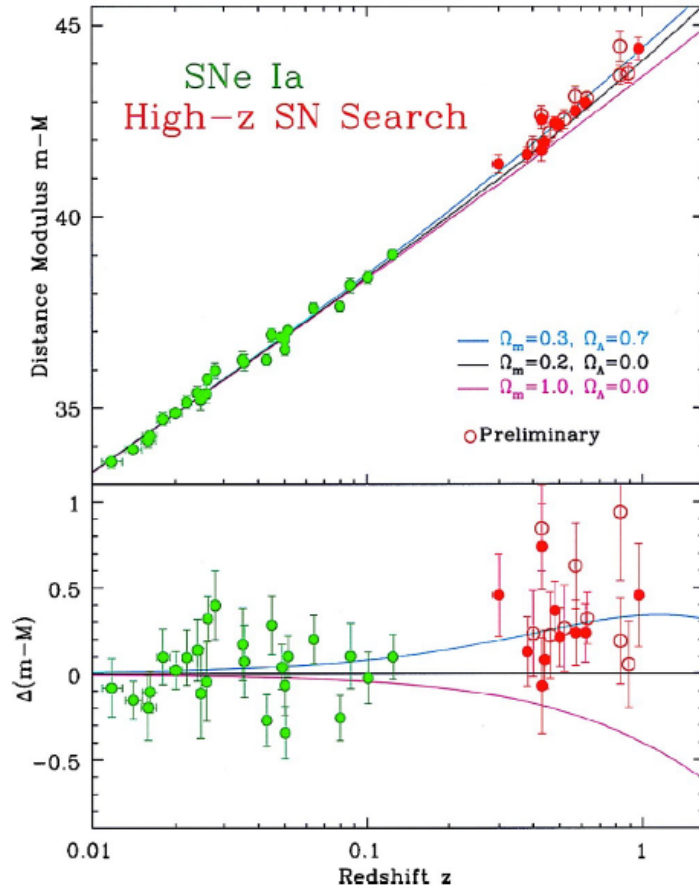


FIGURE 1.5: Magnitude vs redshift result of supernovae type Ia observation (Riess et al. (1998), Perlmutter et al. (1999)).

A cosmological constant dominating at late times can cause cosmic acceleration; however, this model raises problems of its own. The value of Λ observed today is ~ 120 orders of magnitude lower than that predicted by quantum field theory considering the primordial inflationary Λ this problem is called the cosmological constant problem.

In the next chapter I will provide a more detail discussions on the concept of dark matter which manifest itself solely through its gravitational influence on the standard matter. We dedicate some sections to discuss the dark matter problem, the methods that are involved to reveal its existence, the search for its candidates and ultimately its detection mechanisms.

Chapter 2

Dark Matter in Modern Cosmology

2.1 Introduction

Quite a number of evidences exist in modern cosmology to inform us that the ordinary baryonic matter, which is the usual form of matter in diffuse gas, stars and galaxies, make up only 5% of the Universe. The remaining 95% of the matter in the Universe is still in an unidentified form. Of this nearly 70% is contributed by dark energy and the remaining 25% by dark matter (DM), the later being the subject for discussion in this and subsequent chapters.

Historically the study conducted by Jan Oort in 1932 on the motion of neighboring stars is believed to provide the first hint for the existence of DM ([Oort, 1932](#)). The gravitational effect received from the stars within the Galaxy's disk allowed him to provide a measure of the disk's mass. The mass of the disk he obtained was twice the mass in stars and nebulae, which led him to conclude that there has to be more mass than is seen as bright stars. However, Jan Oort concluded the unseen mass to belong to stars that are too dim to be seen. A year after, Fritz Zwicky observed the Coma Cluster and examined its dynamics by assuming that galaxies would be virialized. His study gave evidence for the total mass required to keep the galaxy cluster gravitationally bound to be more than 100 times that of the stars in all its galaxies ([Zwicky, 1933](#)) (see section [1.5.2](#)). Three decades later the missing mass in the Local Group was published by Kahn & Woltjer, ([Kahn and Woltjer, 1959](#)) where they have shown the necessity of having appreciable amount of intergalactic matter to achieve gravitational stability of the Local Group. The renaissance of DM truly began with the “Santa Barbara Conference” on the instability of galaxies in 1961. By that time enough research was done for the community to see that the missing mass anomaly was not going to go away, the uncertainty on the nature of DM remained.

In the mid 1970's a shift in paradigm emerged to interpret observations that seemed to support the ubiquitousness of “missing matter” in the Universe. Various independent sources have confirmed the presence of DM directly at the beginning of 1980's. Furthermore the cold DM model with axions or other Weakly Interactive Particles (WIMPs) was proposed as an alternative to neutrino models which falls under the hot DM models. The existence of DM as a main ingredient of the cosmic fluid as well as its distribution

in clusters was made possible in the 1990's by the gravitational lensing and anisotropies of CMB studies. Current data given the Planck Collaboration put the amount of matter in the Universe to 30% (Planck Collaboration et al., 2015). Despite these overwhelming observational evidences obtained and accumulated for more than 80 years, the challenge still remains as we know quite little about the nature and composition of DM (Muñoz, 2004).

2.2 The DM Problem

In the previous section I have shown that information gathered about the existence of DM is obtained only indirectly from its gravitational effect on the visible matter, radiation and large-scale structure of the Universe. On small (microscopic) scales DM is believed to show weak interactions and this gives hope that it may be detected in low-energy particle physics experiments. So far there is no direct observation of DM and exactly how much there is, and what it is made of is still under investigation, hence the DM problem remains. In the following sub-sections I will present the standard methods of detecting DM.

2.2.1 DM in Galaxies

Among the most common methods of detecting DM is the gravitational influence it has on the baryonic (visible) matter, which provide us with some useful information regarding its content and distribution.

Stars residing in the disk of spiral galaxy (for example galaxies in the local group which the Galaxy and M33 are the member) follow circular path around the center of their host galaxies. Let us consider one of these stars and represent its radius and orbital (rotational) speed by R and v , respectively. Then its acceleration due to the gravitational potential of its host galaxy is given by

$$a = \frac{v^2}{R} = \frac{GM(R)}{R^2}. \quad (2.1)$$

The rotational speed v of the star will then be $\sqrt{\frac{GM(R)}{R}}$, which depends on the radius of the orbit R and the mass $M(R)$ accommodated in the spherical region of radius R .

If we assume that the stars are contributing dominantly to the mass contained in the galaxy, the orbital velocity is expected to fall off at large radii $\propto R^{-1/2}$. However, it has been observed that the velocity rises towards a constant value. For example the rotational speed in the case of M33 is in the range between $\sim 100 - 200$ km s $^{-1}$ as shown in Fig. 2.1. We deduce that this observed flat rotation curve can only be explained with the presence of some other form of matter “dark matter” which has extended distribution in the halos of the galaxy.

2.2.2 DM in Galaxy Clusters

Mass determinations are very important as they measure the amount and distribution of DM in clusters indirectly. The mass of a galaxy cluster can be determined from the

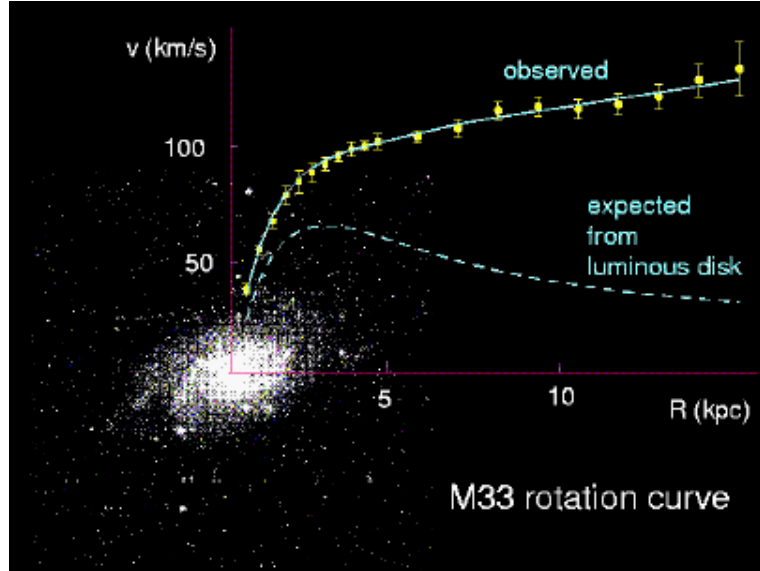


FIGURE 2.1: The observed rotational speed of M33 galaxy in comparison with what is expected from its luminous disk (Roy, 2000).

“virial theorem” ¹ once the three-dimensional mean square velocity $\langle v^2 \rangle$ is obtained from the redshift measurements of a large number of its galaxies, for example for the case of the Coma Cluster we have

$$M_{\text{Coma}} = \frac{\langle v^2 \rangle r_h}{\alpha G} \approx 2 \times 10^{15} M_{\odot}, \quad (2.2)$$

where r_h and α are the half-mass radius of the Coma Cluster and a constant of value ~ 1.0 which depends on the density profile of the cluster, respectively. Comparison of the total mass of Coma Cluster with its luminosity ($8 \times 10^{12} L_{\odot, B}$) gives a ratio of $M_{\text{Coma}}/L_{\text{Coma}, B} \approx 250 M_{\odot}/L_{\odot, B}$. This value shows the vast presence of some non-luminous form of matter in the Coma Cluster. This point is also supported by the fact that the hot gas in the central region of the cluster which is observed to emit X-rays is still in place. In other words, if the hot gas was not to be gravitationally bound by the DM, it would have expanded beyond the region of the Coma Cluster on much shorter time scales than the age of the Universe (Ryden, 2003).

Observations from the X-ray emitting gas can also be used to trace the gravitational potential in clusters, which thus provide an indirect measure of the amount and distribution of DM in clusters. Let us assume that the hot ICM gas is in hydrostatic equilibrium and it has spherical symmetry. This simplification will allow us to express the mass $M(r)$ contained in the radius r of the cluster only in terms of two quantities, namely the gas temperature T and gas density ρ . Both T and ρ can be inferred from X-ray observations, are used to determine the gas pressure, P , using the ideal gas law

$$P = \frac{\rho k T}{\mu m_p}, \quad (2.3)$$

where μ is the gas particle mass in terms of proton mass m_p .

¹Virial theorem states that the average kinetic energy of a self-gravitating system in steady state equals half of the average negative potential energy.

Quantities such as gas temperature and density as well as chemical content can be well determined by fitting the observed X-ray spectrum with theoretical models. An example of this is the temperature map shown in Fig. 2.2 for the case of the Coma Cluster which clearly identifies both relatively hot and cool regions of about $kT \sim 12$, and 5 keV, respectively with a mean temperature of around 9 keV (Watanabe et al., 1999).

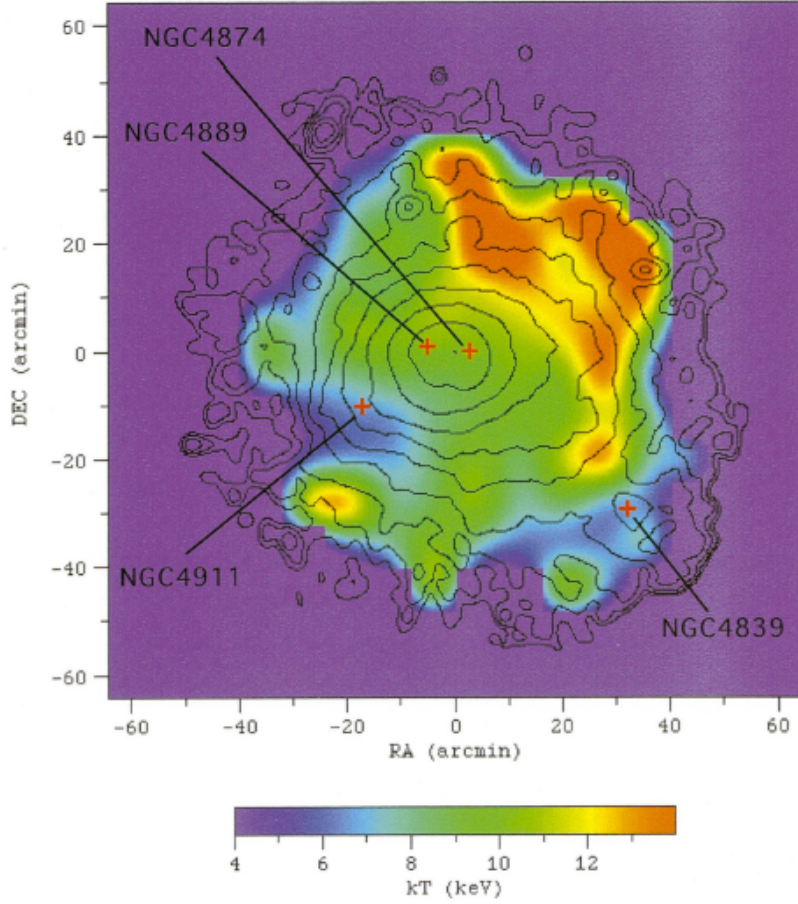


FIGURE 2.2: The temperature map of the Coma cluster (Watanabe et al., 1999).

In hydrostatic equilibrium, the outward force due to the gas pressure balances the force from its gravity infall to give

$$\frac{1}{\rho} \frac{dP}{dr} = -\frac{GM(r)}{r^2}. \quad (2.4)$$

If we substitute the gas pressure P , from Eqn. 2.3 in Eqn. 2.4, we obtain the total gravitational mass in the form

$$M(r) = -\frac{kT(r)r}{G\mu m_p} \left[\frac{d \ln \rho(r)}{d \ln r} + \frac{d \ln T(r)}{d \ln r} \right]. \quad (2.5)$$

Numerical simulations play vital role in advancing our understanding of halo and large-scale structure formation. Their results suggest that the distributions of DM in clusters follow density profile that is power-law. One most commonly used profile is the NFW

profile (Navarro et al., 1996) which has the form

$$\rho_{DM}(r) = \rho_s \left[\left(\frac{r}{r_s} \right) \left(1 + \frac{r}{r_s} \right)^2 \right]^{-1}, \quad (2.6)$$

which has flatter appearance at small radii, and a characteristic scale radius r_s (and density ρ_s) past which they show a sharp decline at large radii. Based the NFW profile we can express the DM mass $M_{DM}(r)$ contained inside radius r in the cluster by

$$M_{DM}(r) = 4\pi \rho_s r_s^3 \left[\ln \left(1 + \frac{r}{r_s} \right) - \left(\frac{r}{r + r_s} \right) \right]. \quad (2.7)$$

Observationally the DM mass in the cluster is obtained by subtracting out the mass contained in the form of gas and individual galaxies in the cluster from the total mass of the cluster, i.e.,

$$M_{DM}(r) = M(r) - M_{gas}(r) - M_{gal}(r), \quad (2.8)$$

where $M_{gal}(r)$ is the mass of the galaxies which can be obtained from optical observations and $M_{gas}(r)$ is the mass of the gas, which can be obtained from Eqn. 2.9 once the gas density, $\rho(r)$, is determined by either model fitting or de-projection

$$M_{gas}(r) = 4\pi \int_0^r \rho(r') (r')^2 dr'. \quad (2.9)$$

Results of the mass of the Coma Cluster based on the assumption that the gas is in hydrostatic equilibrium (i.e., using Eqn. 2.5) gives $1 - 2 \times 10^{15} M_\odot$ within 3.6 Mpc radius. We see that this value agrees well with what is determined by applying virial theorem (Eqn. 2.2) on its galaxies (Ryden, 2003). Following the same procedure on a large number of clusters it has been found that the typical “mass-to-light ratios” for clusters lie in the range $\langle M/L_B \rangle \approx 200 - 300 M_\odot/L_{\odot,B}$. This indicates the ubiquitous existence of DM in galaxy clusters.

2.2.3 DM Through Gravitational Lensing

Gravitational lensing is the gravitational bending of light emitted from an object (the source) by an object between the observer and the source (the lens). There are different types of gravitational lensing namely strong lensing, weak lensing, and microlensing. They are classified depending on the positions of the source, lens and observer, and the mass and shape of the lens which controls how much light is deflected and where.

Strong gravitational lensing occurs when the lens is massive and the source is close enough to the lensing object, a schematic representation of a strong gravitational lensing is shown in Fig. 2.3. Strong gravitational lensing will cause light to take different paths to the observer thus more than one image of the source will appear.

Measurement of matter distributions in galaxies and galaxy clusters obtained using strong gravitational lensing effect has provided strong evidence for the ubiquitous existence of DM with in the Universe. The cores of galaxy clusters are dense enough to produce strong gravitational lensing, giving rise to strongly distorted images of background galaxies, so-called arcs (Bartelmann, 2010). If the source, lensing object and observer are aligned, then the observer will see the light from the source smeared in a

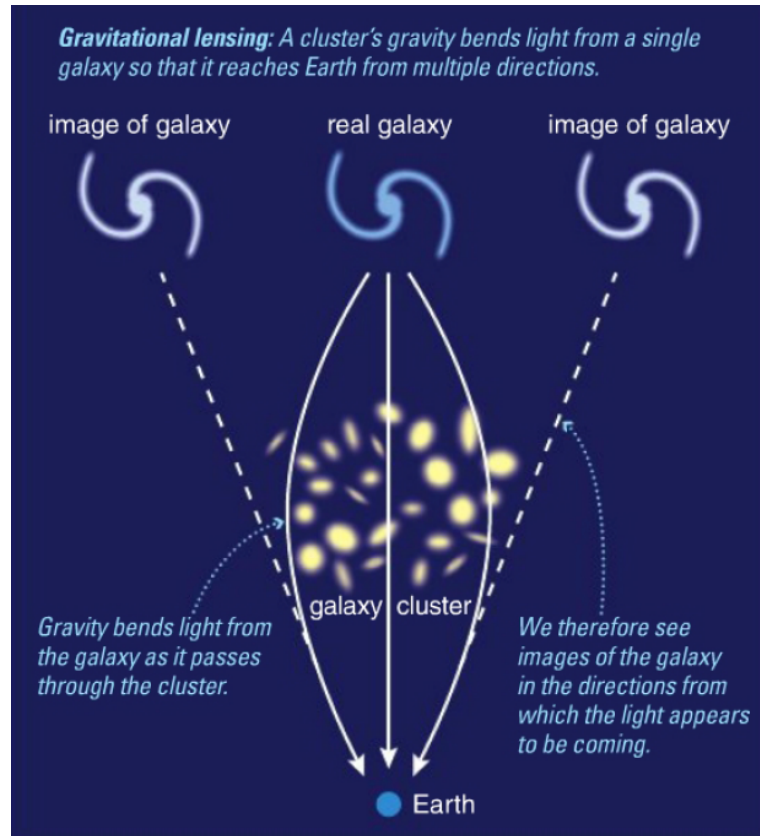


FIGURE 2.3: Multiple image of galaxy due to strong gravitational lensing. Image Credit: [Bennett et al. \(2010\)](#)

circle with the lens in its centre which is known as ‘Einstein ring’. From measurement of position and strength of the lensing object one can determine the angular radius of the ‘Einstein ring’ θ_E using the relation:

$$\theta_E = \sqrt{\frac{4GM}{c^2} \frac{D_{LS}}{D_L D_s}}, \quad (2.10)$$

where D_L , D_S and D_{LS} are the angular diameter distance to the lensing object or deflector, background source, and between them, respectively as shown in the Fig. 2.4.

Thus the measurement of the distance to the lensed object and the source will allow an estimate for the total mass, M , of the lensing object. Once the total mass of the lensing object is determined, it can be used directly to obtain an estimate for the amount of DM within galaxy and galaxy clusters.

2.3 Basic Properties of DM

From observational evidences accumulated so far on the existence of DM a list of its properties can be inferred, some of its basic properties are listed below. i) DM is “dissipationless” which means it involves only in a very weak electro-magnetic interaction. ii) DM is

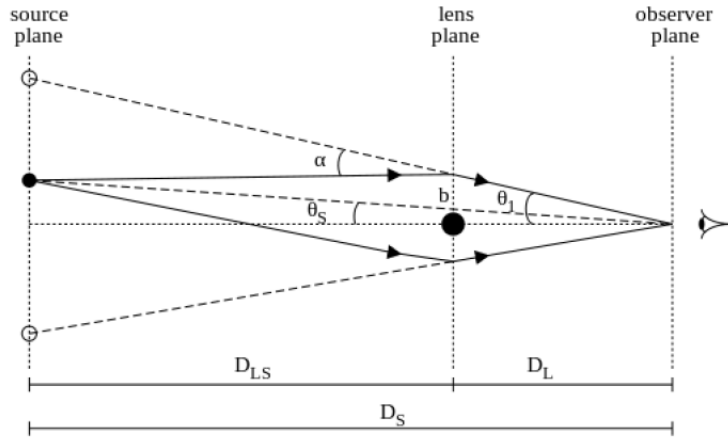


FIGURE 2.4: Graphical representation of gravitational lensing process (Luković et al., 2014).

“nearly collision-less” i.e., the interaction cross-section between DM and baryonic matter for densities found in DM halos is so small to be considered negligible. This also means that its particles are only gravitationally bound to one another and travel unimpeded in orbits in the halos with a broad spectrum of eccentricities. iii) DM is “cold”, which means that they move at non-relativistic speed as they enter matter-dominated era and to cluster effectively and produce the observed intricate structures we observe today; iv) DM is “stable” which means that its lifetime must be comparable to or greater than the age of the Universe. Moreover DM behaves classically to be confined on galaxy scales through attractive gravitational interactions; and as a fluid on galaxy scales as its discreteness is not proved yet (Colafrancesco (2010), Ostriker and Steinhardt (2003)). Thus it goes without saying that these properties of DM which are known so far are to be used as a reference point (to compare with) in the search for the right candidates.

2.4 DM Candidates

One commonly suggested possibilities for DM is to assume astrophysical bodies which are of baryonic form called MAssive Compact Halo Objects (MACHOs) as the main candidates (see for e.g., Sadoulet, 1999, for a review). Some examples of MACHOs include Jupiter-like objects, brown dwarfs (failed stars that are unable to start nuclear reaction), low mass stars and dead stars such as white dwarfs, neutron stars, stellar black hole remnants.

Statistics acquired based on experiments using gravitational microlensing effect which are sensitive enough to monitor low mass objects to a mass of $10^{-7} M_{\odot}$ show that MACHOs contribute less than 25% of the mass of DM in the halo of a galaxy (Afonso et al., 2003). Moreover the amount of baryonic matter predicted from the big bang nucleosynthesis (BBN) sets an upper limit of $\Omega_B h^2 \sim 0.02$ (Burles and Tytler (1998a,b)), which is in agreement with a more recent measurement by Planck experiment of CMB anisotropy (Planck Collaboration et al., 2015). Hence, some of DM could be ordinary matter (MACHOs), but there does not appear to be enough to explain it all, so most

of the DM is probably extraordinary matter, of non-baryonic form, consisting of undiscovered particles. A consensus view thus suggests to us to look for candidates which are of non-baryonic type. In the following sections I will provide a brief discussion for the three most considered ones, among many others which have also been proposed, namely neutrinos, axions and WIMPs.

2.4.1 Neutrinos

Among the zoo of non-baryonic DM candidates neutrinos are the only particles which are certain to exist in nature (Bergström, 2009). A robust result on the mass constraint of neutrino has emerged from tritium β -decay experiment, which point toward an upper limit of $m_\nu \leq 2$ eV (Weinheimer, 2003). Neutrino oscillations on the other hand have determined the mass difference Δm between each species (i.e., the electron, muon and tau neutrino) to be $\Delta m^2 \sim 3 \times 10^{-3}$ (Aliu et al., 2005). These two results are then combined to provide the following upper limit for their relic density:

$$\Omega_\nu h^2 \lesssim 0.07, \quad (2.11)$$

this value thus clearly shows that neutrinos cannot be a dominant component of DM (Bertone et al., 2005). Their mass limit also implies they are relativistic collision-less particles that they would freely stream on scale of about 40 Mpc, as a result of which they would erase the observed density fluctuations on such scale (Komatsu et al., 2009). Moreover simulation results have also shown that the clustering we see today in the Universe cannot fit this picture (White et al., 1983).

2.4.2 Axions

Axions are among well motivated candidates for non-baryonic DM, they were in fact initially proposed not as DM candidates but motivated to solve what is known as the “strong CP-violation” in QCD (Peccei and Quinn, 1977). Constraint from various searches in the laboratory and astronomical bounds (such as analysis from supernova observation and stellar cooling) set the mass of axions below 0.01 eV (Raffelt, 2008).

Several theoretical models suggest that axions should be produced non-thermally in the early universe by mechanisms like the “vacuum realignment” (see for e.g., Feng, 2010, and references therein). They are expected to have small free-streaming length and interact very weakly with other matter which put them among cold DM candidates. So far masses of axions which pass various cosmology and astrophysical constraints are in a range between $10^{-5} - 10^{-2}$ eV (see for e.g., Bertone et al., 2005). A comprehensive review on this topic can be found in Bergström (2000), Bergström (2009) and references therein.

2.4.3 Weakly Interacting Massive Particles

The most viable non-baryonic DM candidates are the Weakly Interacting Massive Particles (WIMPs). A comprehensive review on this topic can be found in Jungman et al. (1996) and references therein. WIMPs are the largest class of cold DM candidates, which are stable particles that arise in extensions of the standard model of electroweak

interactions. WIMPs are believed to exist in thermal equilibrium in abundance in the early universe when

$$K_B T \gg m_\chi c^2,$$

where T and m_χ are the temperature of the Universe and WIMP mass, respectively. WIMPs are generally considered to be self-annihilating, and their abundance was preserved as the number of forward process, i.e., annihilation of the particle χ with their anti-particle $\bar{\chi}$ producing lighter particles l was equal to the backward process:

$$\chi \bar{\chi} \rightleftharpoons l \bar{l}. \quad (2.12)$$

However, as the temperature falls (i.e., $T < m_\chi$) the equilibrium abundance also falls exponentially until the rate of forward process falls below the Hubble expansion rate, $H = \dot{a}/a$. At this point, the WIMPs cease to annihilate, they fall out of equilibrium, and a relic cosmological abundance remains.

Based on the above presented basic concept from [Jungman et al. \(1996\)](#), let us now calculate the relic abundance of WIMPs. The time evolution of the number density $n_\chi(t)$ of WIMPs is given by the Boltzmann equation ([Lisanti, 2017](#)),

$$\frac{dn_\chi}{dt} + 3H n_\chi = - < \sigma_A v > [(n_\chi)^2 - (n_\chi^{eq})^2], \quad (2.13)$$

where the first term in brackets on the right-hand side of Eq. 2.13 accounts for depletion of WIMPs due to annihilation, and the second term arises from creation of WIMPs from the inverse reaction. The equilibrium abundance is obtained when the rate for depletion is equal to creation of particles.

The flux of the DM particles per unit time from a unit volume V containing them is given by

$$\Gamma_{ann} = \left(\int \frac{\rho_{DM}^2}{m_\chi^2} dV \right) \times (\sigma_A v) \times N_{SM}, \quad (2.14)$$

which is a product of three terms, the number of DM particle pairs in the volume V , the DM pair annihilation rate, and the flux of SM particles per annihilation event respectively. In equilibrium the DM annihilation rate can be understood to be $\Gamma = n_\chi^{eq} < \sigma_A v >$, where n_χ^{eq} is the equilibrium WIMP number density and $< \sigma_A v >$ is the DM pair annihilation rate.

The condition at which DM annihilation rate is comparable to the expansion rate of the universe ($\Gamma \sim H$) is known as the “freez-out” condition after which the particles can no longer find each other fast enough compared to the expansion rate of the universe, and thus their abundance per comoving volume asymptotically approaches a constant, their thermal relic density. Note that “freez-out”, also known as chemical decoupling, is distinct from kinetic decoupling; after thermal “freez-out”, interactions that change the number of DM particles become negligible, but interactions that mediate energy exchange between DM and other particles may remain efficient ([Feng, 2010](#)).

Using the “freez-out” condition along with the equilibrium WIMP number density ($n_\chi^{eq} \sim (m_\chi T)^{3/2} \exp^{-\frac{m_\chi}{T}}$) it is possible to determine the present day mass density in units of the critical density, ρ_{cr} , contributed by the DM ([Lisanti, 2017](#)). For typical values of

temperature, $T \simeq m_\chi/20$ and $\langle \sigma_A v \rangle \sim \alpha^2/m_\chi^2$, we obtain the present day mass density in units of the critical density to be

$$\Omega_\chi h^2 = \frac{n_\chi m_\chi}{\rho_{cr}} \simeq \frac{3 \times 10^{-27} \text{ cm}^3 \text{ s}^{-1}}{\langle \sigma_A v \rangle} \simeq 0.1 \left(\frac{0.01}{\alpha} \right)^2 \left(\frac{m_\chi}{100 \text{ GeV}} \right)^2. \quad (2.15)$$

Equation 2.15 shows that a weakly interacting DM particle (i.e., $\alpha \sim 0.01$ and mass $m_\chi \sim 100$ GeV) gives the correct abundance today as measured for example by Planck [Planck Collaboration et al. \(2016a\)](#). This match which is known as the “WIMP miracle” will thus give a possibility to set limit on the annihilation cross-section or lifetime of the WIMP. The most commonly referenced limit of this sort is that the thermal velocity-averaged cross-section must be such that $\langle \sigma V \rangle \simeq 3.0 \times 10^{-26} \text{ cm}^3 \text{ s}^{-1}$ (see for e.g., [Jungman et al., 1996](#), and references therein). The evolution of a thermal relic’s number density is shown in Fig. 2.5. In the plot, Y is the comoving DM number density defined as $Y = n_\chi/s$, and s is the total entropy density of the universe, and Y is rescaled to remove the effects of the universe’s expansion in the above formulation (Eqn. 2.13).

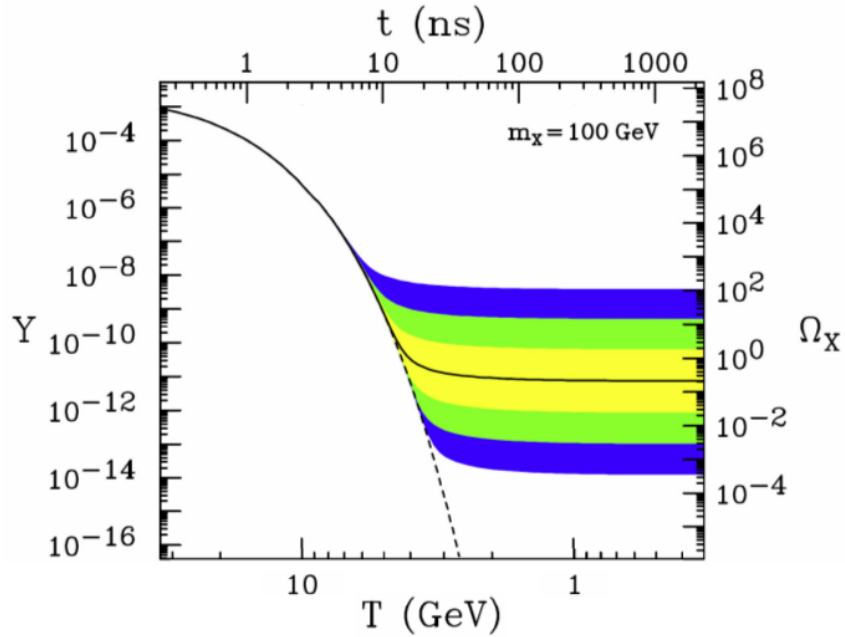


FIGURE 2.5: The comoving number density Y (left) and resulting thermal relic density (right) of a 100 GeV, P-wave annihilating DM particle as a function of temperature T (bottom) and time t (top). The solid contour is for an annihilation cross section that yields the correct relic density, and the shaded regions are for cross sections that differ by 10, 10^2 , and 10^3 from this value. The dashed contour is the number density of a particle that remains in thermal equilibrium ([Feng, 2010](#)).

2.5 DM Detection strategies

We have seen that a correct amount of DM budget in the universe as observed today can be obtained from a model-independent analysis at the weak scale using WIMPs as

a prime candidate. This result has given a strong motivation to the scientific society, which has initiated the development of robust experimental techniques and theoretical frameworks for DM search. A cross-fertilization of these views is thus essential to reach the common goal of detecting DM (Cirelli, 2015). In this section I will review the current and projected experiments for detecting WIMPs.

For WIMPs χ to have the right relic density, they must annihilate to other particles. Assuming that these other particles are standard model (SM) particles, three most promising detection channels have been put forward. These are, production of DM at the colliders, direct and indirect detection of DM which will be described briefly in the following sub-sections. Schematic representation of these three possible DM detection strategies taken from Marrodán Undagoitia and Rauch (2016) is given in Fig. 2.6.

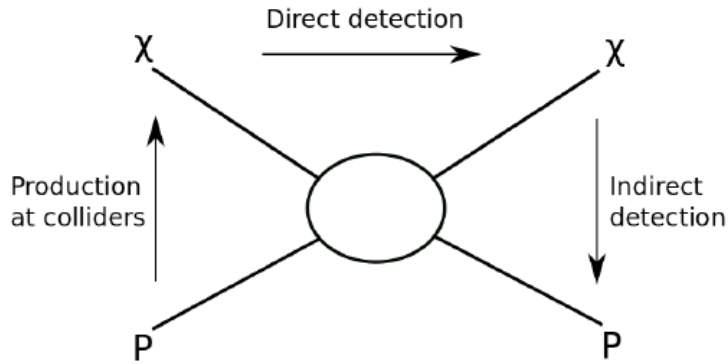


FIGURE 2.6: Schematic representation of the possible DM detection channels Marrodán Undagoitia and Rauch (2016). The DM and the standard model particles are denoted by χ and P .

2.5.1 Particle Colliders

The production channel at particle collider looks like $P + P \rightarrow \chi + \chi$, which is indicated by the arrow pointing upward direction of Fig. 2.6. However, such events are undetectable, but are expected to produce “mono-jet” or “mono-photon” which can provide signatures of WIMPs (Feng, 2010). Information on WIMPs can only be obtained indirectly from the signature of missing transferred energy and momentum. Although the observation of missing particles is consistent with the production of DM, it is far from compelling evidence. The discussions given in the remaining parts of this sub-section are based on (Feng, 2010).

Particle physics experiments at the LHC may stringently constrain cross sections involving DM and related particles. Along with the assumption of a cooling and expanding Universe, this microscopic data allows one to predict the DM relic density, basically by following the relic density curves of Fig. 2.5. This thermal relic density may be compared to the observed density of DM, and their consistency would give us confidence that DM is actually produced in this way and is made of the particles produced at the collider. So far important ranges of the parameter space has been explored by LHC which are in agreement with standard model expectations (Marrodán Undagoitia and

Rauch, 2016). A future facility known as International Linear Collider (ILC) is expected to provide improved results on DM mass and relic density constraints.

Several qualitative studies, such as given in Allanach et al. (2004); Moroi et al. (2005); Birkedal et al. (2005); and Baltz et al. (2006), have investigated the capacity of LHC to determine the ranges of the parameter space depending on various conceivable DM scenario. To this end, these studies have marked precisely the range of values for the cold DM relic abundance which is in agreement with the expected precision measurements for both experiments at the LHC and the ILC. Here I take one case to show this which is given in Fig. 2.7. The WMAP satellite together with other cosmological observations (yellow shaded region) have constrained the DM relic density Ω_χ to a fractional uncertainty of $\pm 8\%$. This uncertainty is expected to be narrowed down to $\pm 2\%$ by its successor, Planck (green shaded region). It is also shown that while the WMAP and Planck can constrain Ω_χ , they are insensitive to the DM mass m_χ ; however, collider experiments are keen to perform both. Moreover, precision studies at the LHC (cyan shaded region) are believed to determine so many of the super-symmetric model parameters that the neutralino mass can be determined to ± 5 GeV and the thermal relic density can be predicted to $\pm 20\%$. Measurements at the ILC (blue shaded region) could improve these constraints on mass and relic density to ± 50 MeV and $\pm 3\%$, respectively.

Notably, the search of both nature and properties of the DM, is believed to provide robust result when there is consistency between the particle physics predictions and the cosmological observations. This would provide compelling evidence that the particle produced at the LHC is indeed DM. The mass, spin, and many other properties of the DM will also be determined at the same time at the colliders. Thus, colliders may finally help solve the question of the microscopic identity of DM.

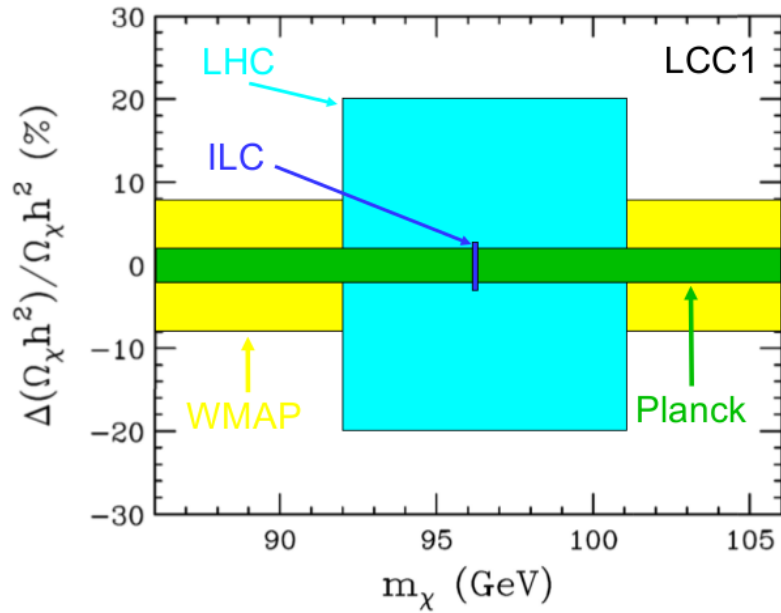


FIGURE 2.7: Constraints in the (m_χ, Ω_χ) plane from the LHC and the International Linear Collider, and from the WMAP (Baltz et al., 2006) and Planck satellites (Feng, 2005).

2.5.2 Direct Detection Strategies

Direct detection mechanisms of WIMPs involves an elastic scattering of WIMPs off normal matter through the interaction $\chi + P \rightarrow \chi + P$ as shown in the Fig. 2.6 with an arrow pointing in the horizontal direction. This process is expected to deposit some recoil energy which may be detected. For example, considering parameters of weak interaction, i.e., taking the allowed WIMP mass between $10 - 1000$ GeV the expected recoil energies induced by WIMPs will be in the range of $1 - 100$ keV (Lewin and Smith, 1996). This will thus require a very sensitive detector placed deep in the ground to avoid contaminating radiations.

The spectral shape of signal candidate-events is used to constrain DM interactions most commonly with the assumption of spin-independent cross-section (derived from a scalar interaction operator) compared to the spin-dependent case (derived from an vector/axial-vector interaction operator). The signal indications and exclusion limits for spin-independent WIMP-nucleon cross-section for both, low WIMP masses (left) and high WIMP masses (right) are given Fig. 2.8. The closed contours show signal indications given by several experiments and the curves show limits excluding the parameter space above the curves. Only a few experiments analyzed the data for an annual modulation of the event rate, mainly due to the requirements to achieve a long-term stability of the detector (Marrodán Undagoitia and Rauch, 2016). The DAMA experiment which uses low-radioactivity sodium iodide crystals for example has observed a signal modulation. The solid red contours show the derived signal regions from DAMA experiment. If this is to be interpreted as a result of elastic scattering with WIMPs, it favors $10 - 15$ GeV WIMPs if the scattering is from sodium, and $60 - 100$ GeV for iodine (Bernabei et al., 2008). The need of confirmation experiments is pointed out in order to eliminate the possibility of unforeseen systematics in Bernabei et al. (2008). Moreover, from these results shown in the two panels of Fig. 2.8 it is apparent that it is difficult to reconcile the DAMA events with a WIMP, due to inconsistency primarily between DAMA (solid red contour), LUX (solid violet curve), CRESST (solid green curve) and Xenon100 (dashed blue curve).

Even though, the presence of various DM indications in the region around 10 GeV gave some excitement, improved results from several experiments indicate that probably in most cases, background was responsible for the observed events. This emphasizes the relevance of the background prediction and the quantification of its uncertainty (Marrodán Undagoitia and Rauch, 2016). Overall, various direct detection experiments have been designed over the last decades. While there is no concrete evidence for DM detection, great progress has been achieved in direct DM searches (Bertone and Hooper, 2016). Moreover, it is expected that future experiments will increase the target masses to achieve an even higher sensitivity which will allow them perform a high statistics measurement of the DM particle properties. A detailed discussion on this topic is provided in Marrodán Undagoitia and Rauch (2016).

2.5.3 Indirect Detection Strategies

DM cannot only be detected directly in dedicated experiments searching for nuclear recoils from the scattering of DM particles or produced in particle accelerators such as the LHC, but it can also reveal its existence indirectly. An indirect detection mechanism

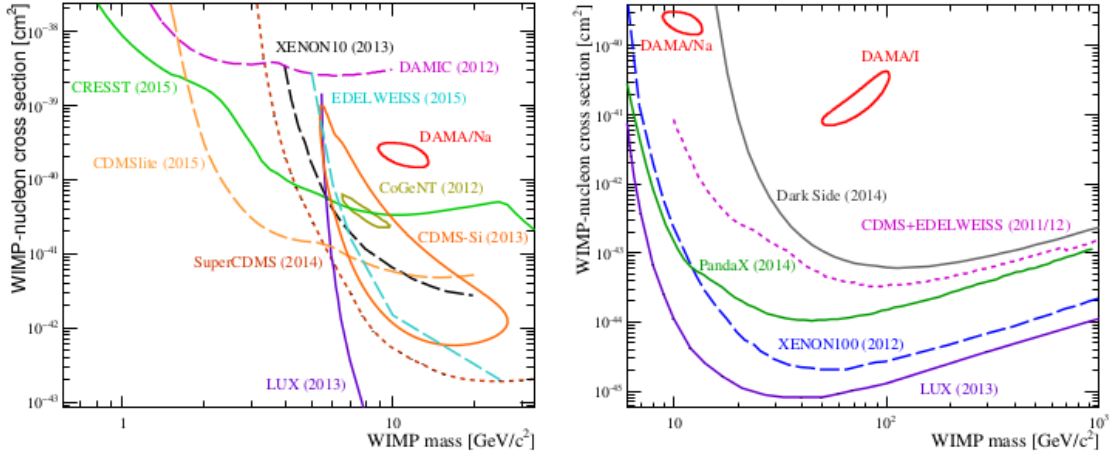


FIGURE 2.8: Overview of signal indications and exclusion limits from various experiments for spin-independent WIMP-nucleon cross-section for low WIMP masses (left) and high WIMP masses (left) (Marrodán Undagoitia and Rauch, 2016).

involves annihilation of WIMPs to produce SM particles. The process is indicated in Fig. 2.6 by the arrow pointing in the downward direction (i.e., $\chi + \chi \rightarrow P + P$).

The total number of DM particles does not change significantly after “freez-out” (see Section 2.4.3) in the early universe, but their spatial distribution changes considerably during structure formation. The very self-annihilation that plays a central role in this “freez-out” can give rise to a significant flux of γ -rays, neutrinos, and even antimatter such as antiprotons and positrons, especially in regions with large DM density. The energy of the secondary particles can reach up to the mass of the DM particle, which typically would be a few hundred GeV. Since DM annihilation scales with the square of its density, indirect detection is more sensitive to cosmological and astrophysical processes than is direct detection (Klasen et al., 2015). Therefore, it is necessary to look for an observable consequences of DM in the emission of the DM annihilation products and their signals in objects of the cosmic structures such as halos of galaxies, dwarf galaxies and galaxy clusters which are characterized by their large DM densities. For example, dwarf spheroidal galaxies which are close satellites of the Galaxy are known for having a large value of mass-to-light ratio thus containing large portion of DM. They are also known for not showing intense star formation and non-thermal high-energy gamma-ray emission which make them a promising search sites for signals from DM annihilation process (see for e.g., Abramowski et al., 2014).

While direct detection is the cleanest technique to unambiguously study the nature and composition of DM; it is also expected that some of the fundamental particles nature of DM can be probed with the detection of photons, neutrinos or charged cosmic rays that are produced by DM. These signals can be studied across multi-wavelength spectrum (see for e.g. Colafrancesco et al. (2006), Colafrancesco et al. (2015) and references therein). The spectrum will be found as combination of synchrotron, IC scattering, bremsstrahlung, and direct photon emission. And all of these emission forms are non-thermal as they depend on the energy distributions of the products of prompt WIMP

annihilation/decay processes. As a result a search for such non-thermal emissions via γ -rays, X-rays, or radio would stand a chance at detecting the signatures of WIMP annihilation. Moreover, detectors for cosmic rays and γ -rays, neutrino telescopes, and radio telescopes can be used for indirect detection of signals from DM annihilation process (Klasen et al., 2015).

Some of the current limits obtained from an indirect detection mechanisms on the WIMP annihilation cross-section is given in Beck and Colafrancesco (2016) which is displayed in Fig. 2.9. The limit obtained by the Planck experiment (Planck Collaboration et al., 2016b) are displayed in blue for two values of the DM energy deposition efficiency parameter f_{eff} . The plot also shows the limits from the Fermi-LAT observations of dwarf spheroidal galaxies (Drlica-Wagner et al., 2015) for WIMP annihilations via b quarks and τ leptons. Comparison should be made between the Fermi-LAT curves and the $f_{eff} = 0.2$ line for Planck (this matches the efficiency of the $b\bar{b}$ and $\tau^+\tau^-$ channels). It is evident that the constraints of Fermi-LAT, though spanning a smaller region, are considerably stronger than those of Planck for masses above 10 GeV. The sensitivity of Fermi-LAT weakens considerably for lower mass WIMPs, where Planck produces superior results. The green region shows the area favored by models accounting for the AMS/Fermi/PAMELA positron excesses (Cholis and Hooper, 2013). While the red area shows the region favored by Fermi-LAT observations of excess γ -rays from the Galactic Centre (GC) (see for. e.g., Hooper and Linden (2011), Hooper et al. (2015), Calore et al. (2015)). This result together with the limits on the WIMP annihilation cross-section derived from radio observation of dwarf spheroidal galaxies using the Australian Telescope Compact Array (ATCA) (Regis et al., 2014) demonstrate the great potential of the indirect γ -ray and radio observation, both having potential which is better than Planck in different parts of the WIMP mass range.

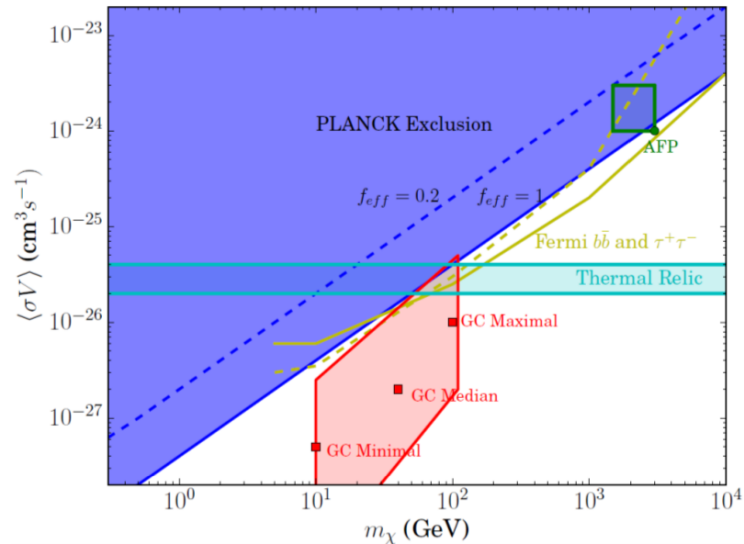


FIGURE 2.9: Figure from Beck and Colafrancesco (2016) showing the annihilation cross-section constraints from Planck (blue) and Fermi-LAT (yellow). As well as regions favored by positron excesses (green) and GC γ -ray excesses (red). f_{eff} refers to the DM annihilation energy deposition efficiency factor (note that $b\bar{b}$ and $\tau^+\tau^-$ annihilation channels have $f_{eff} \sim 0.2 - 0.3$).

In Fig. 2.10 I show another set of constraints taken from [Gaskins \(2016\)](#) which are obtained for WIMP DM models from various selected indirect search analyses for DM annihilation channel $b\bar{b}$. The parameter space above each curve is excluded at 95% confidence level. The limits obtained from H.E.S.S. analysis of the GC halo from [Abramowski et al. \(2011\)](#) (dark solid curve) give the the strongest bounds at the very highest masses. From analyses of the Fermi LAT data, limits spanning an entire range of WIMP masses are obtained both with and without (“inclusive”) modeling non-exotic contributions from the background for the GC. Even though, models with the background (blue dotted curve) from [Hooper et al. \(2013\)](#) are somewhat more “realistic”, they are model dependent. Robust upper limits are thus for those obtained for an “inclusive” models, which are shown for GC (blue solid curve) ([Gomez-Vargas et al., 2013a](#)), the isotropic gamma-ray background (IGRB) intensity spectrum (cyan solid curve) ([Abdo et al., 2010](#)), and the IGRB anisotropy (cyan dashed curve) ([Gomez-Vargas et al., 2013b](#)). The limits from a recent analysis of Fermi LAT observations of satellite galaxies are also displayed (green solid curve) from [Hou et al. \(2016\)](#).

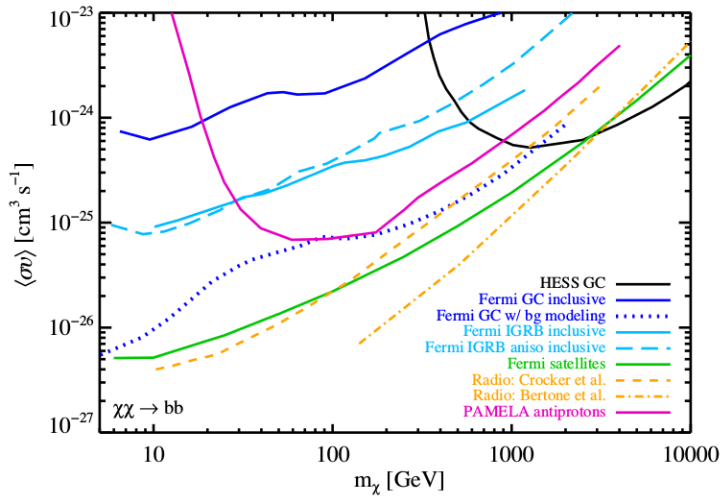


FIGURE 2.10: Constraints on WIMP DM models from selected indirect search analyses for annihilation to $b\bar{b}$. Gamma-ray constraints are shown from a H.E.S.S. analysis of the Galactic Center (GC) halo, together with various analyses of Fermi LAT data. Also constraints obtained using radio observations of the GC and constraints from the PAMELA anti-proton data are shown in this figure which is taken from [Gaskins \(2016\)](#).

Fig. 2.10 also shows some of the strongest bounds on the DM annihilation cross section for the $b\bar{b}$ channel obtained from radio observations by [Bertone et al. \(2009\)](#) (yellow dash-dot curve) and [Crocker et al. \(2010\)](#) (yellow dashed curve). However, as the price limits of these two bounds are highly dependent on the assumptions made in determining the Galactic magnetic field profile, which is poorly known especially at small radii, these limits cannot be taken as robust ([Gaskins, 2016](#)). Also the limits obtained from PAMELA anti-proton data (magenta solid curve) ([Cirelli and Giesen, 2013](#)) are dependent on the assumed propagation model. Thus, an improved understanding of the Galactic environment could help make observations of secondary emission and local cosmic-ray measurements more robust indirect search tools ([Gaskins, 2016](#)).

As shown in Figs. 2.9 and 2.10, the current limits obtained are getting close to constrain the thermal relic annihilation cross section for WIMPs (see for example cyan

shaded region in Fig. 2.9), and the reach of upcoming experiments is expected to improve drastically. With possible detections of different candidates already claimed in gamma rays and X-rays, and suggestive anomalies reported in cosmic rays and the radio background, sensitive indirect searches in multiple targets as well as multi-wavelength and multi-messenger searches will be necessary to support or rule out these claims. Hope has raised to not only robustly detect DM through its annihilation or decay signals, but also to characterize its distribution, and determine its exact particle nature and property in the very near future ([Gaskins, 2016](#)).

2.6 Summary

We have seen that quite a number of independent evidences gathered over the last 80 years favors the existence of a large amount of non-baryonic, non-luminous matter component in the mass-energy budget of the universe known as “dark matter” (DM). However, its particle nature is still unknown thus remains to be one of the most significant problems of modern physics. Also, the current observational data give us very little information as to what form DM might take. One seemingly simple solution to this problem is that DM is constituted by some yet undiscovered particle.

A class of DM particles which are cold weakly interacting particles (WIMPs) are the most viable candidates among large number of proposed particle candidates for DM. This is because they have several important particle properties such as mass, stability (lifetime), scattering cross-section with nucleons, and cross-section for pair annihilation etc., which are both theoretically well motivated and begin to be constrained through various experiments. The final particle detail for WIMPs are obtained from the products into which they annihilate or decay. These particle properties will define whether or not we can observe WIMPs through their interaction with nucleons or their annihilation/decay into standard model particles. In this scenario of DM, WIMPs are produced thermally in the early universe and subsequently “freeze-out” of thermal equilibrium to leave an existing population of cold relic particles, and continue to annihilate/decay producing standard model particles. As a result, they leave an abundance that matches the present-day observations, the “WIMP miracle”.

Being massive, WIMPs interact gravitationally leading to the formation of dense DM halos, providing the gravitational potential wells within which baryonic structure attains stability and forms. The presence of the DM halo around visible structure accounts for the problem of the missing mass which was noticed for e.g., by studying the dynamics of the baryonic matter in galaxies, galaxy clusters (i.e., from flat rotation curves at large radii), and using techniques of gravitational lensing effects. The properties of these halos are highly significant as the increase in WIMP density means that the probability of pairs of WIMPs annihilating in this structure is considerably higher than in a smooth medium, as this will be proportional to the square of the DM density.

Having discussed particle solutions to the problem of DM, three different strategies were explored to find out how WIMPs might be detected. These being direct detection mechanism through WIMPs scattering off (interaction with the) nuclei, detection at the colliders through pair production of WIMPs, and an indirect detection mechanism through the search for annihilation/decay by-products within cosmic structures. Towards the end of this chapter, constraints obtained so far through these detection

mechanisms were given with an emphasis given to an indirect detection of WIMPs as these are the subject of this thesis. We have also seen that these constraints are already starting to constrain the thermal relic annihilation cross-section which are also expected to improve greatly in the very near future, which has an implication not only for the detection of WIMPs but also to characterize their distribution, and determine their exact particle nature and properties.

As the prime objective of this work is to study multi-wavelength emissions from DM annihilation processes in galaxy clusters and sub-halos, which are promising indirect detection search targets, in Chapter 3 I will review galaxy clusters in modern cosmology so as to make connection with our study of the expected multi-wavelength emissions from DM annihilation processes in galaxy clusters. I will thus focus on the discussions of the morphology of galaxy clusters probed at multi-wavelength spectrum with an emphasis given to the study of the non-thermal emissions observed in galaxy cluster. This is because secondary electrons produced by the DM annihilation process are among the possibilities which produce the extended non-thermal emissions observed in galaxy clusters. The various emission mechanisms which are employed in this work will be presented in Chapter 4 along with the discussion on the modeling of the multi-wavelength signals from DM annihilation processes based on high-resolution cosmological simulations of galaxy clusters.

Chapter 3

Galaxy Clusters in Modern Cosmology

3.1 Introduction

Gravitational attraction is believed to bring galaxies together into gravitationally bound structures. Observations show smaller groups of galaxies, with a number of galaxies less than a few hundred, as well as larger groups which have thousands of galaxies, known as clusters of galaxies. Rich clusters have thousands of galaxies, however, since they are relatively rare only about 5 – 10% of galaxies live inside clusters (Dekel and Ostriker, 1999). Observation have also shown grouping among galaxy clusters which are the biggest gravitationally bound structures forming superclusters.

Recent large surveys such as the “2 degree Field Galaxy Redshift Survey (2dFGRS)” (Colless et al., 2001), and the “Sloan Digital Sky Survey (SDSS)” (Eisenstein et al., 2011) have characterized not only the spatial clustering, but also the physical properties of low-redshift galaxies much more accurately than ever before.

These surveys are currently the best large-scale structure maps which show deep multi-color images of 1/3 of the sky as shown in Fig. 3.1. The surveys reveal a “sponge-like pattern” in the distribution of galaxies, and other interesting features such as voids (regions of low density containing very few galaxies) of $30 \text{ h}^{-1} \text{ Mpc}$ are also clearly seen. Large-scale filaments bigger than $30 \text{ h}^{-1} \text{ Mpc}$ surrounding voids as well as denser regions containing galaxy groups, and clusters have also been observed where the filaments intersect. The “great walls of galaxies” that extends across a significant portion of the sky also appear to be separated by about $100 \text{ h}^{-1} \text{ Mpc}$.

Jeans theory in an expanding Universe, also known as “Linear (Perturbation) Theory” explains the formation of structures from gravitational collapse. For example, the pressure of a cloud of an ideal gas opposes collapse of the cloud under its own gravity by the thermal movement of the atoms or molecules comprising the cloud. However, as the cloud cools there will come a point when the internal pressure is no longer able to prevent collapse. As the cloud contracts, it will reach a point where the configuration is in equilibrium.

Structures could have formed in the Universe through two competing scenarios namely, the “top-down” and “bottom-up” scenario. The “top-down” scenario also known as the

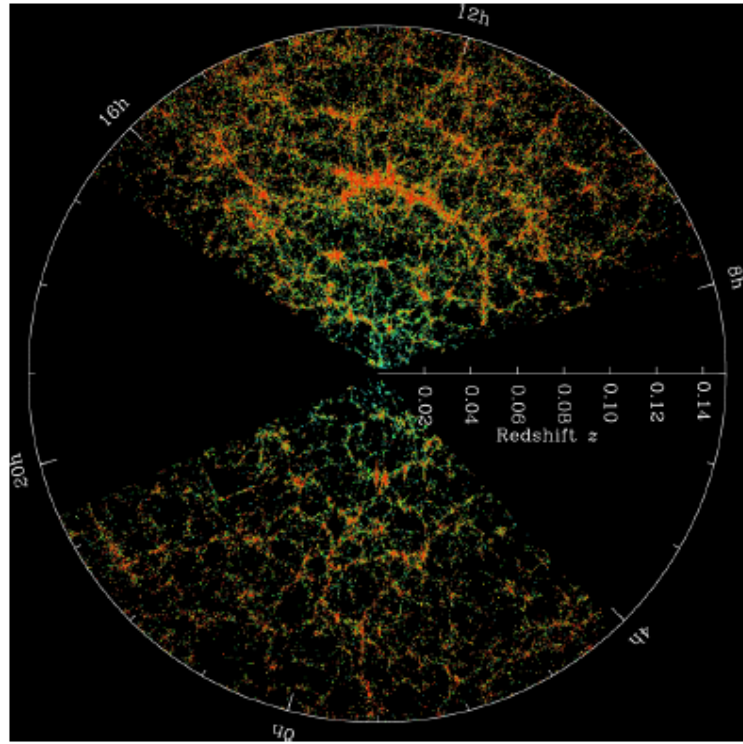


FIGURE 3.1: Large-scale structure in the universe traced by bright galaxies: a 2-D slice through our universe showing galaxies up to two billion light years away, where each dot represents a galaxy. Credit: M. Blanton and the Sloan Digital Sky Survey.

“adiabatic” scenario predicts smaller structure will be formed via the fragmentation of large-scale pancake-like structures. However, it also predicts an enormous amount of anisotropies in the CMB which is inconsistent with recent observations. The “bottom-up” scenario, also known as the “isothermal” scenario, on the other hand is one where smaller objects, with density enhancements roughly about the size of present day dwarf galaxies, were formed first and bound/merge together to form bigger and bigger structures due to gravitational attraction.

Both theoretical frameworks for cosmological structure formation and present day observations are in support of the “bottom-up” framework where DM is believed to be the core agent glueing the structures. In the section 1.5.2 it was discussed that the non-baryonic “Cold Dark Matter” model is more preferable than “Hot Dark Matter” model as it allows structures in the Universe to grow on all scales and dominates its matter content (see for e.g., [Kolb and Turner, 1990](#)).

3.2 Formation and Evolution of Galaxy Clusters

Small irregularities on a wide range of different length scales that were originated at the end of inflationary era are believed to be seeds for structure formation. These initial small irregularities are then acted up on by gravitational instabilities and grow as they evolve to be able to form galaxies and galaxy clusters at a later stage ([Liddle, 2003](#)).

These process of structure formation can be described by linear perturbation theory when the density contrast $\delta_c = \frac{\rho - \rho_0}{\rho_0} \ll 1$, where ρ_0 is the mean density of the Universe (Padmanabhan, 1993). Linear perturbation theory breaks down once $\delta_c = 1$, i.e., particles trajectories will start to cross and their further interactions will be ignored and the equations describing their dynamics will be nonlinear which requires a complex solution. Semi-analytical approaches and/or full numerical simulations will be used to overcome this problem (see for e.g., Bagla and Padmanabhan, 1997, for a pedagogical description).

I will now use the following simplified approach to obtain some important parameters which will be able to describe DM halos and their density contrast. Thus I consider a gravitational collapse of a spherical density perturbations in an expanding Universe by decomposing its density, ρ , into the density of homogeneous background, ρ_0 , and small perturbations, $\delta\rho$ (see for e.g., Bartelmann, 2010, for a pedagogical description). These simple spherical collapse models in general show that an initial spherical overdensity embedded in an expanding background Universe will expand to a maximum radius, and then it turn-around and collapse when the overdensity is gravitationally unstable. This occurs when the density contrast at the time of collapse for a flat Universe containing only non-relativistic matter, for example, is $\delta_c \approx 1.686$ as derived by Gunn and Gott (1972).

A useful approximation for the typical mass scale which is virialized at a given redshift is given by the well known “Press & Schechter mass function” (Press and Schechter, 1974). The number density of the objects at a given redshift z that have masses in range $(M, M + dM)$ is

$$N(M)dM = \sqrt{\frac{2}{\pi}} \frac{\rho}{M} \frac{\delta_c(z)}{\sigma^2} \frac{d\sigma}{dM} \exp\left(-\frac{\delta_c(z)^2}{2\sigma^2}\right) dM, \quad (3.1)$$

where $\sigma(M, z)$ is the standard deviation of the linear density fluctuations at redshift z , smoothed over the region containing mass M . Even though the Press-Schechter mass function is derived based on linear theory with an initial Gaussian spectrum, its predictions for the number of objects at a nonlinear stage is quite remarkable. Predictions of the Press-Schechter mass function at different redshifts show a good agreement with the results of cosmological simulations.

In numerical simulations, the problem of the formation and dynamics of cosmological objects is formulated as N-body problem. Summing up the contribution of all particles to the gravitational force however is computationally inefficient, scaling as $N(N - 1)$. This has lead to the development of techniques such as “particle-mesh (PM)” algorithm, the “particle-particle-particle-mesh” (P^3M) algorithm, Tree codes and other algorithms which make use of these algorithms¹.

Radiative processes, star formation, and supernova feedback also play an important role in building stars and shaping galaxies. Even though most of the time these processes are included in the simulations in a phenomenological way, numerical simulations are

¹PM algorithm computes the gravitational potential on a grid, solving the Poisson equation in Fourier space. Improvements were made possible through the P^3M algorithm which treats the contributions of nearby particles separately (Hockney and Eastwood (1981), Efstathiou et al. (1985)). Tree codes organize particles in groups, and treat the mass in distant groups as a point source (Appel (1985), Barnes and Hut (1986), Hernquist (1987)). In Adaptive Refinement Tree code (ART) automated refinement algorithm is used to refine overdens regions (Kravtsov et al., 1997).

still the best way to advance our theoretical understanding of structure formation deep into the nonlinear regime ([Bertschinger, 2001](#)).

Simulations of large scale structure formation show that, in the standard Λ CDM cosmology, clusters mainly form within filaments of enhanced density, and that the largest clusters often form at the intersection of these filaments. Galaxy clusters form through a mixture of more common mergers with small objects, called minor mergers, or “accretion”, and rarer mergers with larger clusters called “major mergers”.

One example of this is the Millennium Simulation, the largest N-body simulation ever ([Springel et al., 2005](#)). The simulation, containing 10 billion particles, was carried out by the Virgo Consortium using a cluster of 512 processors located at the Max Planck Institute for Astrophysics in Garching, Germany. The aim of this simulation was to trace the evolution of matter distribution in a cubic region of the Universe. The results of the simulation are in agreement with current observations and show that at the present time the structures are abundant in the Universe manifesting themselves as stars, galaxies and clusters. These result of the Millennium simulation showing the non-linear structure formation is shown in Fig. [3.2](#).

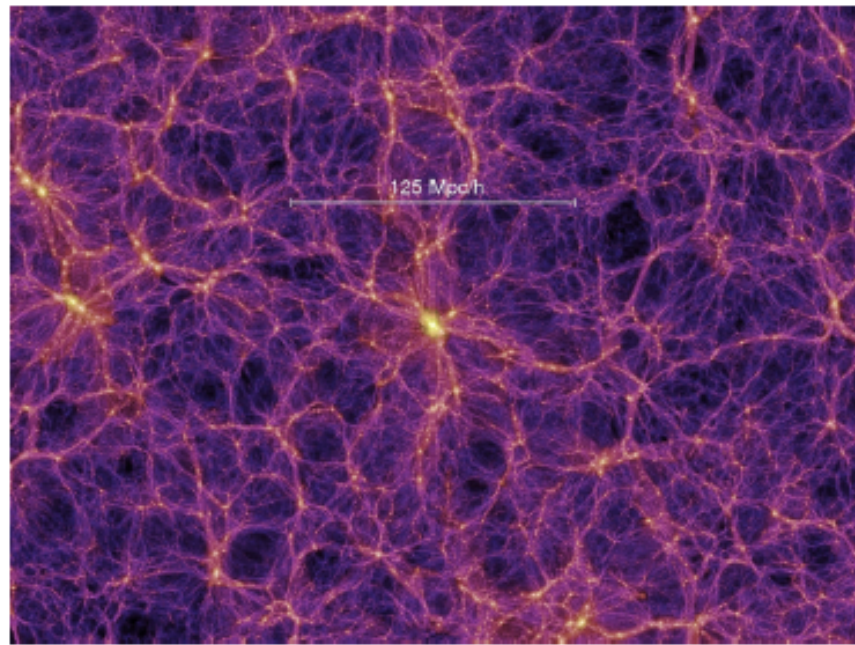


FIGURE 3.2: A 3D visualisation of non-linear structure formation from the Millennium Simulation at redshift $z = 0.0$. Credit: Max Planck Institute for Astrophysics.

Galaxy clusters are of great importance as they trace the most pronounced density peaks of large-scale structure that are localized close to their ongoing formation. They manifest the cosmological structure formation and DM in the Universe. Number counts in galaxy clusters based on mass and redshift are an effective tool to trace large-scale structures in the Universe. Therefore, studying formation, evolution, and distributions of these gravitationally bound structures will equip us with a wealth of useful information to understand properties of the Universe.

3.3 Multi-wavelength Properties of Galaxy Clusters

In the following sub-sections I will review some of the general properties of galaxy clusters probed at different wavelengths, emphasizing the thermal and non-thermal phenomena taking place in their intra-cluster media.

3.3.1 Optical Properties

Clusters are the largest collapsed objects in the Universe that keep tight together their contents by their gravitational potential. Fritz Zwicky (1933) observed clusters of galaxies and found that in general the mass required to keep a galaxy cluster gravitationally bounded is much higher than the sum of the masses of galaxies within the cluster (Zwicky, 1933). This has been accepted to be due to the non-luminous type of matter known as dark matter (DM) which serve as a key link between galaxy cluster and one of its constituents, the DM (see the discussions given in Chapter 2).

Galaxy clusters were first identified in the optical band by counting groups in their projected distribution of galaxies, seen to have some hundreds to thousands of galaxies within them. George Abell (1958) produced the first catalogs purely through visual inspection of photographic plates. They were initially placed into two categories based on their morphology, i.e., regular and irregular clusters. Regular clusters are spherically symmetrical with a pronounced central concentration of galaxies whereas irregular clusters lack symmetry and concentration of galaxies at the centre of the cluster. Later on they were further categorized based on various properties such as; their richness (the number of galaxies within detection aperture), and distance; and the level of dominance of the brightest galaxy/galaxies within them.

The Abell catalogue has been widely used to classify and characterize galaxy clusters (Abell, 1958). A typical example of a cluster that is regular and rich in galaxies is Coma. Virgo is an example of an irregular shaped cluster yet rich in galaxies. Figure 3.3 shows the optical view of cluster A1656 from the Abell catalogue best known as the Coma cluster. This image of the Coma cluster produced in the optical band shows, bright points in most of its volume where roughly each of them correspond to a galaxy, and a much denser concentration of galaxies around its central region.

The distribution of galaxies in a regular cluster is given through the general approximation commonly known as the “King profile”:

$$n(r) = n_0 [1 + (r/r_c)^2]^{-3/2}, \quad (3.2)$$

where r_c is the size of the central region of the cluster. Moreover, optical analyses show that several clusters contain subsystems of galaxies, suggesting that they are still in the phase of dynamical relaxation. Indeed, there is a growing evidence that these subsystems arise as the consequence of group/cluster mergers. Information on merging processes shown to be obtained from the distribution of these clumps, i.e., such as through characterization based on the positions and peculiar velocities of galaxies (Girardi and Biviano, 2002). In general an increasing amount of data has revealed that many clusters are very complex systems (see for e.g., Girardi and Biviano, 2002, and references therein).

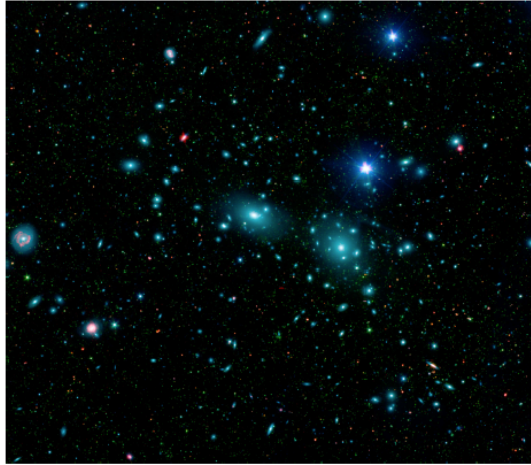


FIGURE 3.3: Central part of the Coma cluster in optical band showing a pronounced central concentration of galaxies. Image Credit: NASA/SDSS.

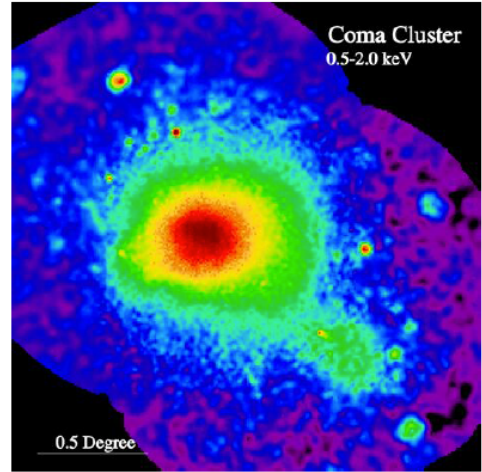


FIGURE 3.4: The Coma cluster in X-ray band showing the bright central region occupied by the X-ray emitting hot gas. Image Credit: MPE.

3.3.2 X-Ray Properties

The contents of clusters of course are not only galaxies and stars, in fact they have a minor contribution to the overall mass of cluster only around 3%. Almost four times as big contribution, amounting to about 12 – 15% of the total mass in galaxy clusters, comes from the hot intra-cluster gas, the remaining 85% being from DM (Vikhlinin et al., 2006). Observations show that galaxy clusters are one of the most luminous extended X-ray sources in the Universe, next to quasars, with luminosity which does not vary with time in the range between $\sim 10^{43}$ and 10^{45} erg/s, which is not associated with individual component of the cluster (Elvis, 1976). X-ray image of the Coma Cluster is given in Fig. 3.4 as an example for our point of discussion, which clearly shows the bright central region occupied by the X-ray emitting hot gas.

The deep gravitational potential well of clusters keep most of the visible baryonic matter in the central region of the cluster in what is known as the intra-cluster medium (ICM). The ICM is heated to a very high temperature, due to energy release from gravitational potential of the cluster, so that it is seen to be filled with thermal plasma and other components including energetic particles and magnetic fields. The typical temperatures and central number densities of this diffuse, hot and very rarefied plasma filling the space between galaxies in clusters is observed to be in the range of $\sim 10^7$ – 10^8 K and $\sim 10^{-3}$ – 10^{-1} cm $^{-3}$, respectively. The distribution of the thermal gas density $n_{th}(r)$ can be approximated well with the so called “isothermal beta model” Cavaliere and Fusco-Femiano (1976). This model assumes a constant temperature and a spherically symmetrical radial profile:

$$n_{th}(r) = n_{th,0} \left[1 + \left(\frac{r}{r_{c,th}} \right)^2 \right]^{-\frac{3}{2}\beta_{th}}, \quad (3.3)$$

where $n_{th,0}$ is the central thermal gas density, r is the radial distance from cluster center, $r_{c,th}$ the cluster core radius, and β_{th} is the gradient of descent for $r > r_{c,th}$. This is given by $\beta_{th} = \frac{\mu m_p \sigma_r^2}{kT}$, where μ is the molecular weight with units of atomic mass,

m_p is the mass of proton, T is temperature and σ_r is the galaxy velocity dispersion. X-ray emissions from the ICM of galaxy clusters which have attained relaxed morphology (i.e., clusters with no record of recent merger activity) show distribution in their surface brightness which shows a peak around their central regions (Parrish et al., 2009). In general, X-ray imaging results using modern instruments, such as ROSAT, Chandra and XMM-Newton, have shown that galaxy clusters exhibit rather a wide range of morphology, which varies from regular to complex systems containing multiple substructures (Jones and Forman, 1992).

The hot thermal plasma of the ICM is a strong X-ray emitting source through thermal bremsstrahlung, i.e., free-free scattering process of electrons by ions, where free electrons are accelerated in the Coulomb field of ionized nuclei and radiate energy. The total energy loss rate per unit volume is given by the expression:

$$-\frac{dE}{dt} \simeq [1.435 \times 10^{-27} Z^2 T^{1/2} \bar{g} n_e n_z] \text{ erg cm}^{-3} \text{s}^{-1}, \quad (3.4)$$

where Z is the charge of the ions and \bar{g} is a mean Gaunt factor which has value of roughly unity. The temperature T and the number densities (n_z for the ions and n_e for the electrons) are measured in Kelvins and cm^{-3} , respectively. Under the assumptions that $Z = 1$ and $n_z = n_e$, the thermal energy density of a fully ionized plasma will be $3n_e kT$. The expression for the characteristic cooling time for the gas can then be obtained by simply dividing the thermal energy density by the rate of radiative loss per unit volume which is given in Eqn. 3.4:

$$t_{cool} = \frac{3n_e kT}{|dE/dt|} = 10^4 \frac{T^{1/2}}{n_e} \text{ years.} \quad (3.5)$$

Thus, if the typical temperature of the gas is $\sim 10^7 - 10^8$ Kelvins, the cooling time is less than 10^{10} years if the electron density is greater than about $\sim 3 \times 10^{-3} - 10^{-1} \text{ cm}^{-3}$, the above formulations were taken from Longair (1994), and they have been rendered to ‘cgs’ units for consistency. It is apparent that the cooling time will be short towards the core of clusters simply because of having relatively large values of n_e in the denominator of the above relation (Eqn. 3.5). Being pushed by the pressure of the surrounding gas the cool gas is expected to flow inward at rates as high as $1000 \text{ M}_\odot/\text{yr}$, this process is known as “cooling-flow” (see for e.g., Peterson and Fabian, 2006).

However, the observed drop in temperature in the ICM of a cluster is less than what is expected from the “cooling-flow” process (Kaastra and Lockman, 1999). It is pointed out in Peterson et al. (2003) that the temperature of the cooling gas at the centre of a galaxy cluster is of order half of which is found further out in the cluster while the expected value is much lower. This has led to the currently debated “cooling-flow problem” where the gas is heated and the “cooling-flow” is greatly reduced. Various hypothesis has been given to solve this problem, the most popular one is that the activity of the central AGN is regulated by the infall of gas producing a feedback mechanism that keeps the gas temperature at roughly $1/3$ of the virial temperature value (see for e.g., McNamara and Nulsen, 2007). Other possibilities include the effect of heating of the gas produced by cosmic rays (CR) accelerated by bipolar jets produced in the explosion of supernovae (Colafrancesco et al., 2004) and that they act as warming rays (Colafrancesco and Marchegiani, 2008).

3.3.3 Radio Properties

Galaxy clusters are also characterized by their emission in the radio band in addition to their emission in optical and X-ray band which is discussed in the previous sections. Recent observations using sensitive radio telescopes have shown radio emission from individual galaxies which are often observed to extend beyond the galaxies' optical boundaries. Mpc-scale radio emissions are also observed in a fraction of galaxy clusters (Ferrari et al., 2008). As there is no clear connection between these sources and individual galaxies in the galaxy clusters; these observed radio emissions is expected to be the result of an interaction between the thermal ICM plasma and non-thermal components of a galaxy cluster (see for e.g., Feretti et al., 2012, and references therein).

Large-scale diffuse radio sources have been observed by sensitive radio telescopes in many clusters. Various observations have shown that these emissions follow a power-law spectrum, suggesting that these sources are of non-thermal origin due to synchrotron emission produced by relativistic particles in a magnetic field. The total intensity image of Coma cluster showing the large-scale diffuse radio sources such as radio halo and relic, which will be presented below, is given in Fig. 3.5. Comparison between the radio and X-ray observation have also revealed a similarity but not an exact identity between the morphology of the large-scale diffuse radio sources and the X-ray emission of their host clusters, see for e.g., Deiss et al. (1997); Liang et al. (2000).

A number of studies have also claimed correlations between radio powers and X-ray power (Bacchi et al., 2003), temperature (Liang et al., 2000), mass (Govoni et al., 2001), and Compton parameter (Colafrancesco et al., 2014). However, these claims, that the radio morphology follows the X-rays ones, are not always observed (see for e.g., Govoni et al., 2012). This is because, while clusters at same X-ray luminosity seem to be bimodal with respect to their radio luminosity, there are some clusters with similar X-ray luminosity that show the presence of a radio halo in some cases and do not show in other cases.

On the other hand, it is known that in the hierarchical structure formation scenario merging processes among cosmic structures such as sub clusters and clusters are common. They are believed to be characterized by shocks that compress the intra-cluster gas which result in an increase in the temperature of the ICM (see for e.g., Ryu et al., 2003). As a result a significant amount of the kinetic energy is converted into generating shock heating and compression of the ICM and possibly into accelerating particles. The latter phenomenon is supported by the detection of non-thermal radio emission observed from diffuse extended radio sources. These galaxy clusters which show diffuse synchrotron emission are in general divided into three main groups namely, “radio halos”, “radio relics”, “mini-halos” (see for e.g., Feretti et al., 2012, and references therein).

Radio halos are extended diffuse radio sources that are situated around the central Mpc^3 region of the cluster showing a low-surface brightness. They have regular radio morphology that follows the X-ray emitting thermal gas. Their low surface brightness ($< \mu \text{ Jy arcsec}^{-2}$ at 1.4 GHz) which is often lower than radio relics as well as their steep spectra and large angular sizes makes their detection quite difficult (see for e.g., Deiss et al., 1997).

Radio relics are irregularly shaped diffuse synchrotron sources observed in the outskirts of galaxy clusters. Like radio halos, relics has also been detected in both merging and cool-core systems. These detections are also suggestive of a possible connection with a

minor or off-axis mergers as well as major-merger events. Moreover, the intensity of the polarized signal is lower in radio halos than relics. This suggests that these two sources have different origin (see for eg. [Feretti et al. \(2012\)](#), [Ferrari et al. \(2008\)](#)).

Mini-halos are less extended diffuse radio sources of size ≤ 500 kpc which are observed in some relaxed, cool-core clusters (see for e.g., [Ferrari et al. \(2008\)](#), [Bravi et al. \(2016\)](#)). Their emission is usually observed encompassing the central radio source associated with the radio-loud brightest cluster galaxy ([Bravi et al., 2016](#)). Like the radio halos, mini-halos show both steep spectra and very low surface brightness (see for e.g., [Murgia et al., 2009](#)).

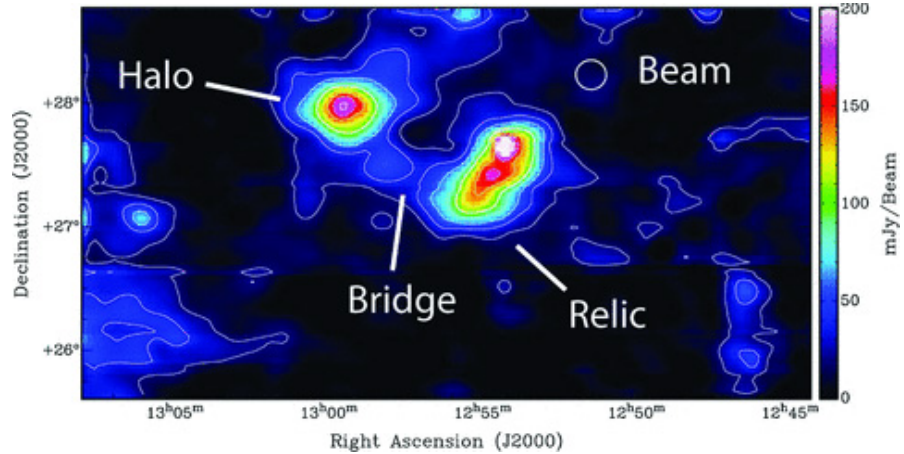


FIGURE 3.5: Image of radio halo and relic of the Coma cluster taken from [Brown and Rudnick \(2011\)](#). This is a GBT total intensity image with all NVSS emission subtracted out (see [Brown and Rudnick, 2011](#), for detail.).

At present the origins of diffuse synchrotron emission in radio halos, relics and mini-halos are still not well understood. The most common theoretical models that have been suggested to describe the mechanism of energy transfer into the relativistic electron population as well as the origin of relativistic electrons, which are the key components to the above mentioned non-thermal processes, will be presented and with the discussion on both their strength and demerit in Section 3.4.

3.3.4 Magnetic Fields

The origin and evolution of a magnetic field in galaxy cluster and the Universe as a whole is one of the big puzzle in astrophysics. Even though observations in radio band have provided evidence for a magnetic field strengths of up to a few μG in galaxy clusters and galaxies (see for e.g., [Ryu et al., 2012](#), and references therein), its origin remains unclear ([Kulsrud and Zweibel, 2008](#)). Primordial magnetic field strengths at the epoch of CMB radiation have had their strength limited below 10^{-10} G (see for e.g., [Neronov and Vovk, 2010](#)). One way to generate the seed magnetic field is by the battery mechanism ([Biermann, 1950](#)), which uses the fact that electrons and ions have very different masses. When pressure gradients develop in the plasma, the particles get accelerated differently, electrons being accelerated more strongly due to their smaller masses will lead to charge separation which generates an electric field. As a result, a varying electron density in space produces an electric current which gives rise to a corresponding magnetic field.

The seed magnetic field generated through this and similar mechanisms ranges from 10^{-19} to 10^{-16} G. Once the seed magnetic field is generated, various mechanisms tend to amplify it. It has been argued that turbulent motions can be maintained in the ICM and its dynamo action can prevent a decay, and amplify a random seed magnetic field (Subramanian et al., 2006).

There are various methods to determine magnetic field strength in galaxy clusters some of these include: analysis from equipartition between electrons and magnetic fields in radio halos, comparison between synchrotron and inverse Compton emissions, inference from study of cold fronts, and the Faraday rotation measure. Faraday rotation measure is one most popular technique which is used to determine the strength and distribution of a magnetic field directly. It is produced when linearly polarized radiation, emitted by background sources, interacts with magnetic fields in the plasma. When this linearly polarized radiation propagates through a magnetized plasma its plane of polarization rotates, consequently two modes of circular polarization, each having different value of phase velocity, emerge.

The intrinsic polarization angle ϕ_0 is rotated from the source polarization angle ϕ by an amount $\Delta\phi = \phi - \phi_0$. It has been observed that the position angle difference $\Delta\phi \propto \lambda^2$ (Gardner and Whiteoak, 1963). By integrating this position angle difference in the line-of-sight we can determine the Rotation Measure RM (i.e., $RM \equiv \Delta\phi/\lambda^2$), which is related to the parameters of the magneto-ionic medium between the source and the observer using the expression:

$$RM = \left[0.812 \int_0^l (n_e/10^{-3} \text{cm}^{-3}) (B_{\parallel}/\mu\text{G}) (dl/\text{kpc}) \right] \text{rad m}^{-2}, \quad (3.6)$$

where n_e is the number of electrons per unit volume in the plasma measured in units of 10^{-3} cm^{-3} , B_{\parallel} the component of magnetic field parallel to the line-of-sight in units of μG , the integral is performed along the line-of-sight with l in units of kpc (Carilli and Taylor, 2002). Thus Eqn. 3.6 will provide us with a direct measure of the magnetic field values once the electron number densities are well determined from observation such as X-ray emission in the ICM of a galaxy cluster. From RM observations the magnetic field strengths of radio halo in galaxy clusters has been deduced to be a few μG on average (see for e.g., Kim et al. (1990), Feretti et al. (1995), Bonafede et al. (2010)).

Magnetic fields strength can be estimated from the total synchrotron emission provided by a source while uniformity and structure of the fields can be used to obtain information about the degree of polarization. In general the magnetic field strength through out the cluster on average shows a very large variation with complex structures, fluctuating over spatial scales of a few kpc up to hundreds kpc. Moreover, it has been suggested that the mean magnetic field strength and density of relativistic electrons in the cluster can be determined directly if the non-thermal emission has its origin in Compton scattering of relativistic electrons by the CMB photons (Rephaeli, 1979).

3.3.5 Gravitational Lensing

Important information about galaxy cluster such as mass and distribution of matter can be deduced from gravitational lensing (more discussion on gravitational lensing is given under sub-section 2.2.3). A famous example in which gravitational lensing provides us with information on the mass and distribution of matter is the case of

“Bullet Cluster” also known as “1E 0657-558”. The “Bullet Cluster” is composed of two massive clumps of differing mass, that have undergone collision. As shown in Fig. 3.6 we see a smaller cluster (right region in blue color) emerging from larger cluster (left region in blue color) after a high-speed collision which has separated the X-ray emitting hot gas (indicated in red color) from that of the galaxies (Markevitch et al., 2002). A map of the system’s overall mass (indicated in blue color) made from gravitational lensing observations (Clowe et al., 2006), does not coincide with the location of the system’s hot gas which is obtained through X-ray observations (indicated in red color) (Markevitch et al., 2002). This fact is difficult to explain without the inclusion of DM, because the gas contains several times as much mass as all the cluster’s stars combined. An easiest explanation for this morphology of Bullet Cluster is, however possible, if DM is to be included, i.e., the collision has simply stripped the hot gas away from the DM on which it was previously centered. Moreover, the “Bullet Cluster” is not the only galaxy cluster where the distribution of DM derived using the gravitational lensing technique is found to be quite different from the X-ray one, another case for example is that of A1914 (Barrena et al., 2013).

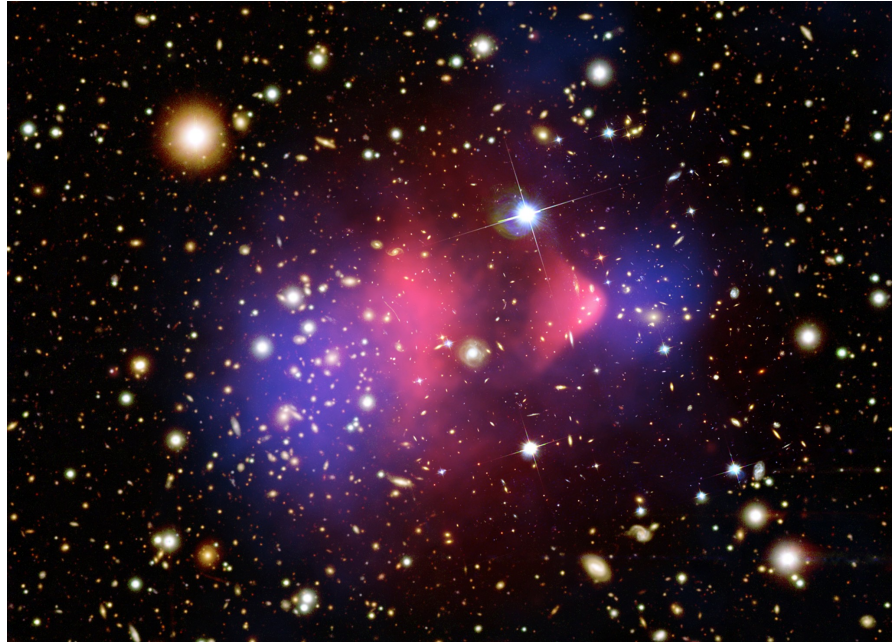


FIGURE 3.6: Distribution of matter in the Bullet Cluster. The smaller cluster (blue region on the right) is seen to emerge from the larger cluster (blue region on the left) consequently stripped the system’s hot gas (red color). Composite Image Credit: (Gravitational lensing by Clowe et al. (2006); X-ray and optical by Markevitch et al. (2002)) taken from Bullet Cluster (2017).

3.3.6 Gamma-ray Properties

It is believed that most of the cosmic rays produced in clusters of galaxies remain confined for a long time within the cluster potential wells and consequently produce high energy gamma-rays through their interactions with ICM (Blasi et al., 2007). The emission of γ -rays from galaxy clusters is expected to be high, for example, due to IC Scattering and non-thermal bremsstrahlung by relativistic electrons (Blasi and Colafrancesco, 1999).

Moreover relativistic protons, being the dominant non-thermal component of galaxy clusters, enhance the probability of hadronic interactions between thermal and non-thermal protons (Colafrancesco and Blasi (1998); Marchegiani et al. (2007)) that produce γ -ray emissions through the decay of pions and inject secondary particles. The emission of γ -rays from galaxy clusters is also expected to be the result of the DM annihilation processes Colafrancesco et al. (2006); Marchegiani and Colafrancesco (2016).

Although a γ -ray signal from the cluster volume is expected to arise through interactions of cosmic ray protons with the ambient plasma, currently there is no clear evidence for the detection of emissions in the γ -ray band in galaxy clusters (Ackermann et al. (2014), Huber et al. (2013)). Therefor, this is suggestive of the presence of some problems with the current models or observations. Moreover, the recent derived Fermi-LAT upper limits on the content of cosmic rays (e.g., Huber et al., 2013) is a severe problem for all the known models (Vazza and Brüggen (2014), Vazza et al. (2016)), except possibly for the DM ones (Marchegiani and Colafrancesco, 2016).

In addition to the optical, radio, and X-ray, and γ -ray bands, galaxy clusters are also expected to emit in the extreme ultraviolet, hard X-ray, and microwave frequencies. In the next few sections I will discuss some of the possible detections claimed for the non-thermal emission across these spectral bands in galaxy clusters.

3.3.7 Extreme Ultra-Violet

Advanced instruments such as the Extreme Ultra-Violet Explorer (EUVE) Satellite and XMM-Newton have recently been able to provide very important information down to low X-ray energies. From two largest samples of galaxy clusters with soft X-ray excesses Bonamente et al. (2002) have shown that around 30% of the galaxy clusters exhibit excess emission over the extrapolation of the usual thermal emission from the hot ICM to the extreme ultraviolet and soft X-ray ranges. However, currently these detections and their interpretation of the soft X-ray excess is not conclusive (see for e.g. Bowyer (2004), Bregman and Lloyd-Davies (2006)).

The soft excess emission in Coma for example has been interpreted to be, of thermal origin by Lieu et al. (1996), or due to IC scattering of CMB photons by relativistic electrons (Sarazin and Lieu, 1998a). Moreover, Bowyer (2004) has suggested this radiation in Coma to be of secondary origin from hadronic interactions. However, the latter claim has been ruled out owing to the upper limits made by EGRET of the excess in gamma-ray emission Marchegiani et al. (2007).

3.3.8 Hard X-ray Emission

Non-thermal hard X-ray (HXR) emission from galaxy clusters have long been proposed to be produced from Compton scattering of CMB photons (Rephaeli, 1977). Possible detection of an excess in HXR emission have been claimed to be observed in some clusters (see for e.g., Blasi and Colafrancesco, 1999). However, it is uncertain whether these excess HXR emissions are detected or emanated from faulty data analyses (Rossetti and Molendi, 2004).

In a similar way to the case of EUV, various models have been put forward for the mechanisms producing these excess emissions in HXR band. These include models

suggesting the possibility that the HXR excess comes, from peripheral high-temperature regions (Eckert et al., 2007), due to IC scattering by relativistic electrons (Blasi and Colafrancesco (1999); Sarazin and Lieu (1998b)), and via a non-thermal bremsstrahlung process by supra-thermal tail of thermal electron spectrum (Enßlin et al. (1999); Sarazin and Kempner (2000); Blasi (2000)).

The interpretation of bremsstrahlung emission has been questioned by Petrosian (2001), because it would require unreasonably high energy input for electrons. The IC Scattering interpretation taking the electrons to be of secondary origin has been excluded by Blasi and Colafrancesco (1999) as these should produce strong gamma-rays. At present, the most plausible non-thermal process believed to produce this excess is the IC scattering of the CMB photons by the same population of relativistic electrons responsible for the radio/synchrotron emission. However, recent observations (Ajello et al. (2009); Gastaldello et al. (2015)) seem to indicate the HXR excess previously claimed was not real.

3.3.9 Sunyaev Zeldovich Effect

Galaxy clusters are also observed to emit in the microwave band through the process known as the Sunyaev-Zeldovich effect. The Sunyaev-Zeldovich (SZ) effect is produced when the CMB photons are shifted to higher energies due to the ICS process with the hot electrons passing through the ICM of a galaxy cluster (Sunyaev and Zeldovich, 1970). The effect depends on the pressure produced by the cluster plasma along the line of sight, and hence on its density. SZ effects have been observed in several clusters. A great deal of information on thermal as well as non-thermal properties of galaxy clusters can be obtained from the SZ effect measurements employing full relativistic formalism (see for e.g., Colafrancesco et al. (2003); Colafrancesco et al. (2011b)).

SZ effect is redshift independent thus can be used more suitably, for example, to make statistical studies of galaxy clusters (Colafrancesco et al. (1994); Colafrancesco et al. (1997)). SZ effect surveys will therefore be able to detect all clusters above a mass limit, independent of the redshift of the clusters, offering an ideal tool for determining the cluster density evolution which in turn can be used to constrain cosmological parameters like the Hubble constant (see for e.g., Birkinshaw (1999), Carlstrom et al. (2001)). Some new possible applications of SZ effect include, the study of the non-thermal SZ effect in radio galaxies Colafrancesco et al. (2013), the possibility to measure the structure of the temperature in a galaxy cluster (see for e.g., Colafrancesco and Marchegiani (2010); Prokhorov and Colafrancesco (2012)), the CMB anisotropies through the polarization of SZ effect (Shehzad Emritte et al., 2016), and the history of cosmic reionization through the SZ effect of the 21 cm background (Colafrancesco et al., 2016).

Moreover, along with the X-ray observations, high-resolution SZ observations of single clusters can be used to study properties of the ICM. And these can be used to study the outskirts of clusters where there is still a traceable signal from SZ effect, which may allow for the investigation of the shocks that are believed to be responsible for the non-thermal radio emission observed in many clusters.

3.4 Origin of Radio Halos in Galaxy Clusters

At present the nature and properties of large-scale radio halos and relics are poorly understood due to the present observational limits. Additionally, because of the synchrotron and inverse Compton energy losses, the typical lifetime of the relativistic electrons in the ICM is expected to be relatively short $\sim 10^8$ yr. As a result, the electrons suffer from difficulties to diffuse over a Mpc-scale region within their radiative lifetime (Feretti et al., 2004). To resolve these several models have been proposed which describe the mechanism of energy transfer into the relativistic electron population as well as the origin of relativistic electrons. In general, these models can be put in to two main categories, i.e., models which involve the “primary electrons” and “secondary electrons”.

3.4.1 Primary Electrons

In the primary electrons model of the origin of relativistic electrons, relativistic particles such as cosmic ray electrons and protons are believed to be injected in galaxy clusters volume by the energetic sources during the cluster dynamical history. These energetic sources are mainly due to AGN activity and radio galaxies Ensslin et al. (1997), as well as galactic winds from starburst galaxies and supernovae Völk et al. (1996); Völk and Atoyan (2000). Thus according to this model electrons can be accelerated in shocks Tribble (1993) by the mechanism of Diffusive Shock Acceleration (DSA) (Drury (1983); Blandford and Eichler (1987)) or emitted by galaxies Jaffe (1977).

However, it has been suggested that these populations of electrons needs to be re-accelerated in order to compensate for their radiative losses Petrosian (2001). Some of the shortcomings of the primary electrons model are the electrons have short lifetime as compared to the age of the cluster (see Fig 3.7) and, as a result of the energy losses, they travel short distance as compared to the size of a radio halo. The distance which the particles (i.e., the electrons) travel during their average lifetime through diffusion process in a magnetized plasma (the diffusion path of a particles $R_d(\gamma)$) can be approximated using the following expression,

$$R_d(\gamma) = \sqrt{4D(\gamma)t_{\text{loss}}}, \quad (3.7)$$

where $t_{\text{loss}} = \frac{\gamma}{b(\gamma)}$ is the life time of electrons (see for e.g., Brunetti (2003)). And γ , $b(\gamma)$, and $D(\gamma)$ terms in the above expressions are the Lorentz factor of the electrons, the loss factor, and the diffusion coefficient, respectively, which enter the diffusion equation (i.e, Eqn. 4.6) discussed under Section 4.5.

Using the above formula it can be shown that the approximate distance the electron will travel will be ~ 50 kpc which is far less in comparison with typical scale of a radio halo (\sim Mpc). Because of this the electrons will be confined to the region where they were initially accelerated and they will be limited to produce synchrotron emission for a short period of time. This phenomena, however, contradicts with the observed extended diffuse synchrotron emission at a larger scale as well as the relative abundance of the electrons.

Another problem with electrons accelerated at the shocks in the cluster, via the DSA process mentioned above, is the low efficiency of this process. The later is expected

to arise as most of its energy goes to heating of the thermal gas rather than to the acceleration of the particles (Wolfe and Melia, 2006).

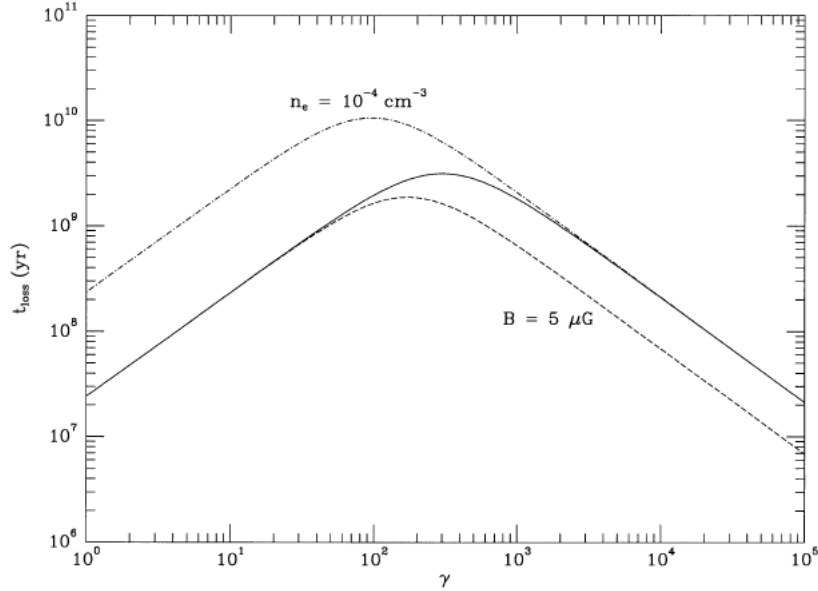


FIGURE 3.7: A plot of the life time of electrons as a function of their energy, for magnetic field $B = 1 \mu\text{G}$ and an electron density of $n_e = 10^{-3} \text{ cm}^{-3}$ (solid curve) and with $B = 5 \mu\text{G}$ (dashed curve) as well as updated $n_e = 10^{-4} \text{ cm}^{-3}$ (dot-dashed curve) taken from Sarazin (1999).

3.4.2 Re-accelerated Electrons

In the re-accelerated electrons model which is a sub-catalog of the primary electrons model, cosmic ray electrons that are injected by the above listed processes are expected to be accelerated again (re-accelerated) by turbulence processes which produce magnetohydrodynamic (MHD) waves during merging (Miniati et al. (2001a); Ryu et al. (2003)) or accretion events in clusters (Ensslin et al., 1998). The re-acceleration of particles by the turbulence processes can be achieved for the range of electron energies where the time scale of energy losses exceeds the time scale of re-acceleration. Thus the electrons that can be re-accelerated probably need to have Lorentz factor of the order of 10^2 to survive for several Gyrs, as this will allow them to be around during the period in which the re-acceleration process is effective.

However, even though there is a need for frequent re-acceleration of electrons at the centre of the cluster to suppress the energy loss and be able to form a radio halo, the observed regular morphology of radio halos is quite hard to be fitted with an intermittent re-acceleration of particles by turbulence predicted by this model.

Moreover, the stochastic particle acceleration by MHD turbulence (Brunetti et al. (2001); Fujita et al. (2003); Feretti et al. (2004)) is a second-order Fermi (Fermi-II) process (Fermi, 1949), and is a rather inefficient process that can accelerate electrons up to energies of a few GeV. For emissions at higher energies, inverse Compton and non-thermal bremsstrahlung from relativistic electrons are the only viable processes. As a result of this the γ -ray emission is expected to be generally low which also suppress the

synchrotron emission at higher radio frequencies. It has been suggested in [Ackermann et al. \(2014\)](#) that a lack of detection in γ -ray range from radio halo could be in support of this model.

Another possibility which is suggested in [Brunetti et al. \(2012\)](#) to account for the low efficiency mentioned above take the electrons which are re-accelerated to be of secondary origin, i.e., the electrons are produced by the hadronic interactions such as that given in Eqn. 3.8. In this case the protons should also be re-accelerated which will thus increase the γ -ray emissions ([Brunetti et al., 2004](#)). Consequently a lack of γ -rays detection will be a problem for the re-acceleration models.

3.4.3 Secondary Electrons

Secondary electrons also called hadronic models are another set of models which suggest mechanisms for the origin of relativistic electrons in galaxy cluster. In this model relativistic electrons are believed to be produced as a result of interaction between non-thermal protons and the protons from the gas in the ICM ([Dennison \(1980\)](#); [Blasi and Colafrancesco \(1999\)](#)). The reactions that lead to the production of secondary electrons are described by the secondary electron model:

$$p + p \rightarrow \pi^\pm + X,$$

where X represents any reachable final state from the initial state. The charged pions (π^\pm) will decay into electrons, positrons and neutrinos via muons;

$$\pi^+ \rightarrow \mu^+ + \nu_\mu,$$

$$\pi^- \rightarrow \mu^- + \bar{\nu}_\mu,$$

and

$$\begin{aligned} \mu^+ &\rightarrow e^+ + \nu_e + \bar{\nu}_\mu, \\ \mu^- &\rightarrow e^- + \bar{\nu}_e + \nu_\mu. \end{aligned} \quad (3.8)$$

Similarly, the neutral pions (π^0) will decay predominantly into γ -rays:

$$\begin{aligned} p + p &\rightarrow \pi^0 + X, \\ \pi^0 &\rightarrow \gamma + \gamma. \end{aligned} \quad (3.9)$$

Having negligible energy loss, the protons can diffuse over large scales throughout the cluster volume unless their energy is of the order of 1 TeV, above which they can escape from the cluster [Berezinsky et al. \(1997\)](#). As a result, the protons will be able to produce non-thermal electrons continuously in their locality. In the presence of a magnetic field with strength of order of few μ G, these non-thermal electrons are expected to emit in the radio band, the intensity of this diffuse radio emission (which is characteristics of radio halos discussed under Section 3.3.3) is also proportional to the thermal gas density ([Miniati et al., 2001b](#)). Consequently the secondary electrons model predict radio spectra which do not show any features, i.e., a regular morphology in radio halos, which is expected as the cosmic ray protons will diffuse throughout the cluster (see for e.g., [Miniati et al. \(2001b\)](#), [Feretti et al. \(2012\)](#)). This model will thus face some difficulty in addressing radio halos with a complex morphology.

The secondary electrons model also predict strong correlation between radio and X-ray luminosity, because the non-thermal electrons are well correlated with the thermal gas. However, this strong scaling relation predicted by this model fails to account for the presence of a cluster with high observed X-ray luminosity and no radio halos (Enßlin et al., 2011). This model also predicts γ -rays from pion decay (Eqn. 3.9) as well as neutrinos (Eqn. 3.8), which can be tested with new generation γ -ray telescopes (Feretti et al., 2012).

Moreover, some other problems of the secondary model include, the steepening at high frequencies of the Coma radio halo spectrum (Thierbach et al., 2003) (see Fig. 3.8), the change of the spectral index along the cluster Giovannini et al. (1999), and the worst problem being the lack of gamma ray detection (see for e.g., Ackermann et al., 2014).

3.4.4 Secondary Electrons from DM Annihilation Process

Secondary electrons/positrons from DM annihilation process is the fourth model suggested as a possible source of relativistic particle in galaxy clusters. In this model DM annihilation/decay processes are believed to produce a wide range of standard particles and radiations such as electrons, positrons and gamma-ray radiations. Electrons and positrons will undergo energy losses through their interactions with the particles in ICM and will emit in a multi-wavelength spectrum after reaching equilibrium states through various emissions mechanisms Colafrancesco et al. (2006). These process of emission along with the standard formulas of the emissions from DM annihilation processes are given in Chapter 4. In the following I will focus my discussion to more advanced problems which I address in this work, which is connected with the spatial distribution of the DM and its impact on the radio emission and the importance of the boost factor provided by small substructures.

As has been mentioned at the end of last chapter, this work will focus upon one popular and most favored DM candidate called the neutralino. Neutralino is, a cold DM particle (as it moves with non-relativistic speed), and a member of a large group of DM particles, the Weakly Interacting Massive Particles (WIMPs) (see Section 2.4.3). Neutralino are also the lightest particle from the minimal super-symmetric extension of the standard model (MSSM) which are introduced by a minimal model of super-symmetry. According to this model particles occur in super-multiplets (also known as super-partners) which is often summarized as every boson is paired with a fermion and vice versa. Under super-symmetry transformations all of the quantum numbers are preserved, keeping the spin, which is changed by one half. Thus, a super-multiplet is a collection of particles related by super-symmetry transformations and differing only in their spins. Since the quantum numbers of the Higgs boson, photon, and Z boson are identical and all have a possible super-partner with the same quantum numbers and spin half, super-positions of these states will form a collection of neutralino mass eigenstates, with the lowest mass eigenstate being the neutralino of interest (see for e.g., Bertone et al., 2005, for a comprehensive review on this topic).

The neutralino forms an attractive model because it is neutral, weakly interacting, and has viable mechanisms for the production of a thermal relic population (see for e.g., Jungman et al., 1996). Additionally, while there is currently no experimental evidence in favor of super-symmetry, super-symmetric effects may manifest unambiguously in collider experiments (see Section 2.5.1). It is worth mentioning the fact that even-though

these gives an impression that DM should be stalked exclusively within the confines of particle accelerators or direct scattering experiments, the possibility of indirect detection through astrophysical signatures remains a promising alternative. This is primarily due to the weakly interacting nature of the neutralino which allows for mutual pair annihilation to produce a host of standard model particles which may then be ejected as cosmic rays or instead subsequently emit radiation themselves.

Neutralinos are believed to annihilate into neutral pions which then decay into high-energy γ -rays. In addition to this their annihilation/decay processes are also believed to produce a wide range of standard particles such as electrons, positrons, that are formed either directly or from charged pion decay. Electrons and positrons will undergo energy losses through their interactions with the particles in ICM and in the highly magnetized environment of cosmic structure to emit in a multi-wavelength spectrum after reaching equilibrium states through various emissions mechanisms [Colafrancesco et al. \(2006\)](#). These mechanisms which are synchrotron radiation process in radio band and neutral pion decay, IC scattering, and bremsstrahlung radiation processes in γ -rays will be modeled in Chapter 4 using data from high-resolution cosmological simulations. Neutralino annihilation would thus result in non-thermal emissions, characteristic of the DM particle, from any structure that played host to a concentration of such particles. Additionally, the increasing sensitivity of astronomical measurements and the limitations of current ground-based direct detection experiments combine to elevate indirect detection methods (see Section 2.5.3) to new levels of competitiveness when it comes to setting limits on the nature of DM.

Several authors have studied the astrophysical consequences of these assumptions laid on secondary electrons from DM annihilation process such as [Colafrancesco and Mele \(2001\)](#); [Colafrancesco et al. \(2006\)](#); [Pérez-Torres et al. \(2009\)](#) and many more. One common strength of these previous studies lies in their ability to reproduce the observed steepening in the flux spectrum, the spectral energy distribution, at higher radio frequencies of the Coma cluster shown in Fig. 3.8. This can be understood to be due to the fact that the spectrum of secondary electrons steepens when the energy of the electrons is comparable to the mass of neutralinos, as shown in the Fig. 3.9 ([Colafrancesco et al., 2011a](#)).

Even though, these studies based on DM models are able to match the observed spectral properties of the radio halo in the Coma cluster, they are unable to reproduce the shape of the radio halo structure (surface brightness) as they produce a shape that is too concentrated towards the center of the cluster. This is due to the way they model the DM distribution in Coma, i.e., they often consider the DM distribution as a single spherically symmetric halo, while the observed DM distributions show a complex shape and elongated structures (see for e.g., [Gavazzi et al. \(2009\)](#); [Okabe et al. \(2014\)](#)). In addition, these models will require 1 or 2 order of magnitude higher DM annihilation cross-section as compared to the recent upper limits of the order of $\langle \sigma V \rangle \sim 10^{-27} - \sim 10^{-26} \text{ cm}^3 \text{ s}^{-1}$ (see for e.g., [Ackermann et al. \(2014\)](#); [Calore et al. \(2015\)](#)) to produce the observed radio flux as was argued in [Colafrancesco et al. \(2015\)](#). Moreover, today the construction of modern and sensitive instruments such as SKA in radio band and CTA in γ -ray bands have raised hope that detailed information regarding the spatial distribution of the emissions are achievable.

Motivated by these observations, in this thesis I will study the effect of the realistic distribution of the DM sub-halos in the simulated Coma like cluster on its emission in

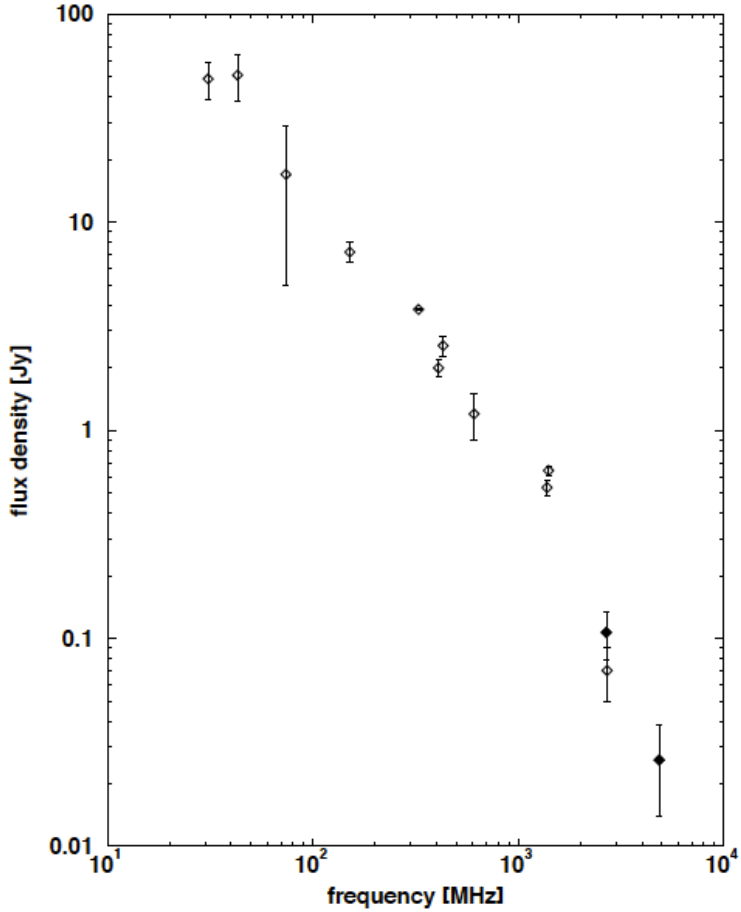


FIGURE 3.8: The observed radio halo spectrum of the Coma cluster (Thierbach et al., 2003).

the radio and gamma-ray bands. Thus, to address the above mentioned issues, I will take neutralino masses of 35 and 60 GeV with $b\bar{b}$ composition and DM annihilation cross-section of $1.0 \times 10^{-26} \text{ cm}^3 \text{ s}^{-1}$ to produce the multi-wavelength emission maps from DM annihilation processes. Based on a realistic modeling of the DM distribution using MUSIC-2 cosmological simulations data (see Section 4.2), it is possible to show that the signals from DM annihilation process are in the detection limits (see Section 5.2). This results will also reflect how well the DM distributions are represented in the simulations through a simple semi-analytical DM model of the emission processes presented in Chapter 4, which is able to incorporate the effects of the sub-structures in boosting the signals to provide radio flux densities from the DM annihilation processes to the level of the observed one, without invoking any boost factor due to sub-structures.

I will also demonstrate how the simulation of galaxy clusters and their DM content can be used to estimate the multi-wavelength emissions from these objects. In this way, not only the expected radio and γ -ray spectrum (see for e.g. Figs. 5.11 and 5.19) can be predicted but also the spatial distribution of the emissions (see for e.g. Figs. 5.4, 5.5 and 5.17, 5.18). Moreover, comparison of the results will be made with the radio data of the Coma cluster to test if the emissions from DM sub-halos are achievable with SKA. A similar steps will be followed to study this aspect in the γ -ray band, following which

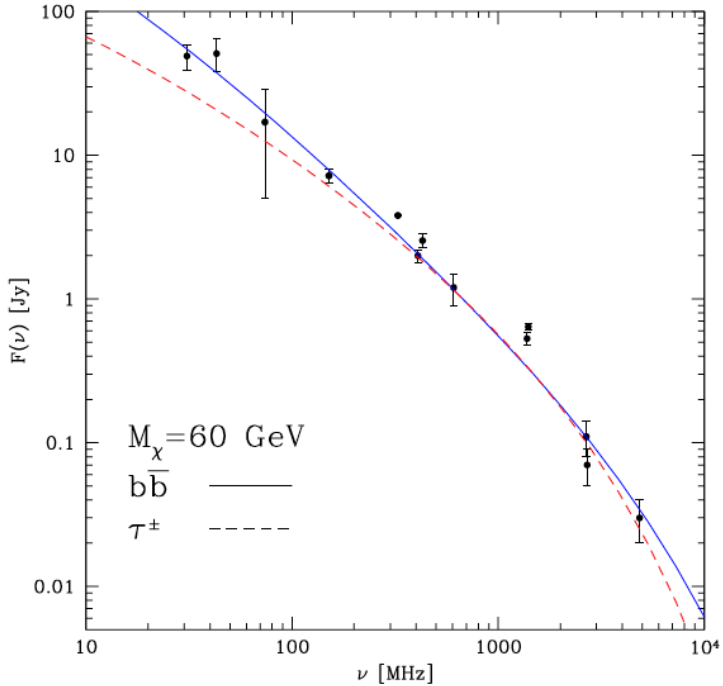


FIGURE 3.9: Comparison of the observed spectrum of the Coma Cluster with the best fits of DM model by [Colafrancesco et al. \(2011a\)](#).

DM sub-halos will be studied as a more suggestive environment to obtain signals from the DM annihilation processes.

3.5 Summary

In this chapter I have discussed the formation, evolution and phenomenology of galaxy clusters based our current understanding. A fraction of galaxy clusters exhibits diffuse cluster/sub-cluster scale non-thermal emissions across multi-wavelength bands which are not related to any particular galaxy, and manifest themselves through the relativistic electrons and magnetic fields in the ICM that resides along with the emissions from the hot gas. As a result, a complete understanding of the properties of galaxy clusters requires a comprehensive study of the non-thermal component of galaxy clusters, for which radio halos and relics are the main source of information.

However, at present the origins of these diffuse extended non-thermal emissions in galaxy cluster is still not well understood. On the theoretical side, the most common explanations believed to give rise relativistic particles responsible for these emissions and the mechanism by which the energy is transferred to sustain them were presented identifying their strength and weaknesses (see Section 3.4). The secondary electrons as gamma-rays produced, which this thesis is based on, are believed to be produced from DM annihilation/decay processes. These electrons are also expected to undergo energy losses through their interactions with the particles in ICM and magnetic field thus undergo energy losses to provide an equilibrium spectra which will emit in a multi-wavelength spectrum via various emissions mechanisms.

A number of researchers have studied the astrophysical implication of these processes. While previous works were able to reproduce successfully for example the observed spectral properties of the radio halo in the Coma cluster, they were unable to reproduce the spatial distribution of the emission as they often consider the DM distribution as a single spherically symmetric halo. To address this problem, I explore the effect of realistic representation of the spatial distribution of the DM and its impact on the radio emission, and the importance the small sub-structures in boosting the signals to the observed level in galaxy cluster and DM sub-halos. Therefore, in the subsequent Chapters of the thesis I will strengthen the study of these objects using a multi-wavelength approach, i.e., in both radio and gamma-ray bands.

The development of the remaining part of the thesis will be as follows. In Chapter 4 I use a number of high resolution cosmological simulations, containing dark matter, gas, star formation and feedback, to develop semi-analytical models which provide multi-wavelength emission maps from DM annihilation processes in galaxy clusters and sub-halos. I will then apply these models to the case of galaxy clusters and present the results obtained in Chapter 5. In Chapter 6 the properties of high mass-to-light ratio DM sub-halos which are promising targets to reveal the nature of DM will be studied, and results which are related both to their statistics and their multi-wavelength emissions will be given. Concluding remark will be given in Chapter 7 where I summarize the main results obtained in this work, present possible way of testing them, and mention future improvements required.

Chapter 4

Modeling Multi-wavelength Emissions from DM Annihilation Processes

4.1 Introduction

The previous chapters have clearly shown us that galaxy clusters are of great importance, as they manifest the large-scale structure formation of the Universe, non-thermal processes, and that of DM. Numerical simulations show that galaxy clusters form through grouping of smaller objects or “accretion” of clumps along the filaments and rarely through “mergers” with larger clusters which is also known as “bottom-up” scenario. The largest clusters often form at the intersection of the filamentary structures (Ryu et al., 2003). The formation of these structures is driven by DM (Kolb and Turner, 1990) (see Chapter 3 for a review on structure formation and galaxy clusters).

A type of cold DM particles which are weakly interacting massive particles (WIMPs) known as neutralinos are believed to constitute DM (see Section 3.4.4). The neutralinos are Majorana type particles, hence they are their own anti-particles. When two of these particles come close, it is expected that they annihilate each other, producing standard matter (SM) particles such as neutral and charged pions. As shown in Fig. 4.1, the neutral pion and charged pions will decay into gamma-rays and relativistic electrons/-positrons, respectively in relatively short time. These secondary electrons/protons (see Section 3.4.4) for example will produce radio signals from synchrotron emission processes, and gamma-rays from bremsstrahlung radiation and Inverse Compton Scattering (ICS) processes (Colafrancesco, 2010). Having said that, in the following sections I will describe the semi-analytical model, which is developed based on high resolution cosmological simulations of galaxy clusters, for these multi-wavelength emissions produced by neutralino DM annihilation processes in galaxy clusters and DM sub-halos.

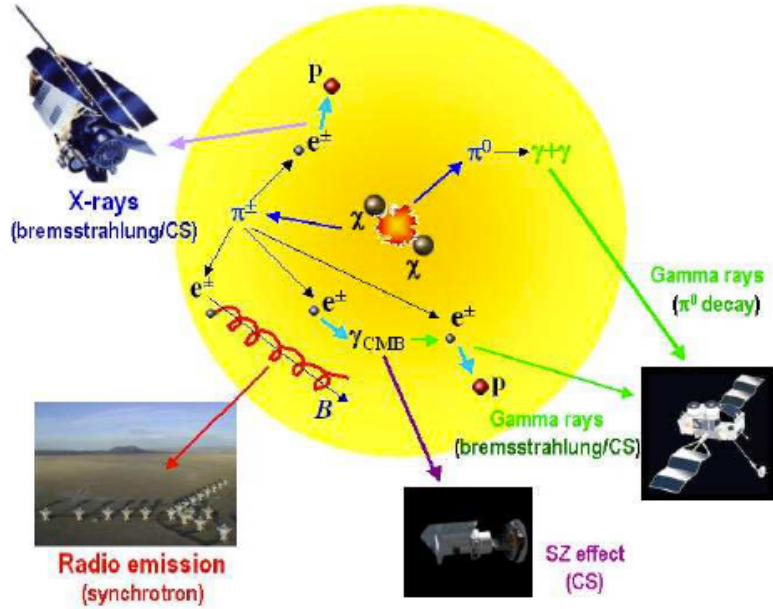


FIGURE 4.1: Graphical representation of multi-wavelength emission from neutralino annihilation processes (Colafrancesco et al., 2006).

4.2 MultiDark Simulation of galaxy Clusters

In this section I will provide a brief summary of the MultiDark SImulations of galaxy Clusters (MUSIC-2) dataset, which I have used in order to determine the DM annihilation flux from neutralino χ in galaxy clusters and sub-halos. The reader is referred to the original paper by Sembolini et al. (2013) for a full review on the Marenostrum-MultiDark SImulations of Galaxy Clusters (MUSIC).

What is known as MUSIC-2 simulation, which is used in this work, is a large subset of a mass limited sample of re-simulated clusters selected from the MultiDark Simulation. The MultiDark Simulation simulation is DM only N-body simulation which contains 2048^3 , i.e., about 9 billion, particles in a $(1 \text{ h}^{-1} \text{ Gpc})^3$ cube (Prada et al., 2012). This simulation was performed using the best-fit cosmological parameters to WMAP7 + BAO + SNI ($\Omega_M = 0.27$, $\Omega_b = 0.0469$, $\Omega_\Lambda = 0.73$, $\sigma_8 = 0.82$, $n = 0.95$, $h = 0.7$) (Komatsu et al., 2011).

All objects with masses above $10^{15} h^{-1} M_\odot$ at $z=0$ were first selected from a low resolution (256^3 particles) version of the MultiDark simulation to be re-simulated. A total of 282 objects were found to be above this mass limit. All these 282 massive clusters were then re-simulated both with and without radiative physics by producing the initial conditions of the re-simulated objects using the zooming technique (Klypin et al., 2001). That is, all particles within a sphere of 6 Mpc radius around the center of each selected object at $z=0$ from a low resolution version (256^3 particles) of the simulation were found first. This set of particles were then mapped back to the initial conditions to find out the Lagrangian region corresponding to a $6 h^{-1}$ Mpc radius sphere centered at the cluster center of mass at $z = 0$. The initial condition of the original simulation was generated in a finer mesh of 4096^3 , this has thus improved the mass resolution of the re-simulated objects by a factor of 8 as compared to the original simulations. The highest

mass-refinement level within the Lagrangian region of each cluster were kept and then covered with shells of increasing mass particles down to the lower resolution level of 256^3 . To avoid problems with periodic boundary conditions the simulations were re-centered, thus each re-simulated cluster always located at the center of the corresponding box. In this way the simulations were produced to have DM particles of 5 different mass refinements. The gas SPH particles were added only to the highest refinement level. The SPH particle positions were slightly displaced from their parent dark matter by 0.4 times the mean inter particle distance in the 3 spatial directions and they were given the same initial velocity as their dark matter counterparts.

The parallel TreePM+SPH GADGET code (Springel, 2005) was used to run all the re-simulations. The re-simulation has accounted for the effects of radiative cooling, UV photoionization, star formation and supernova feedback, including the effects of strong winds from supernova, in the same way as described in Springel and Hernquist (2003) model. The mass resolution of the simulation at the highest level is $9.01 \times 10^8 \text{ h}^{-1} \text{ M}_\odot$ and $1.9 \times 10^8 \text{ h}^{-1} \text{ M}_\odot$ for DM and SPH particles, respectively (Sembolini et al., 2013). In the following I will describe the semi-analytical model, which provides the multi-wavelength spectrum from neutralino DM annihilation processes in galaxy clusters and DM sub-halos, that is developed based on the MUSIC-2 simulations presented above.

4.3 The DM Density Square Maps

In order to determine DM annihilation flux from neutralino χ I have used MUSIC-2 simulation (Sembolini et al., 2013), which is a high resolution hydrodynamical, zoomed-in simulation of 282 galaxy clusters. Fig. 4.2 shows the density profile of one specific cluster. The density profiles for DM, gas and stars, are given in red (solid line), green (dotted line) and blue (dot dashed line), respectively. We compute the densities in terms of their mean density which will allow us to compare between the three species. At the outskirts of the cluster the slope of the DM and gas density profiles are very similar and stays above that of the stars, which is expected as the number of stars should decrease in the outer region (less galaxies). On the other hand, I observe a gradual increase in the number density of the stars, where almost each peak in the dot dashed line represents an encounter of a new galaxy, towards the inner region as most of the baryonic mass is going into forming the stars. The fact that the stars are the dominant component in the inner region of the cluster is a manifestation of the over-cooling problem, a well known feature in current cosmic simulations due to shortcomings in the prescription of feedback mechanisms.

The evaluation of DM annihilation flux from neutralino χ involves a product of two terms: the term A_{DM} , the particle physics part, that depends on the particle physics model of DM, and the cosmological part which involves a line of site volume integral of the density squares evaluated in each cube as given below (Gondolo and Gelmini, 1991)

$$\Phi = A_{DM} \int_{l.o.s} \rho_\chi^2 dV, \quad (4.1)$$

where ρ_χ is the neutralino DM density.

Taking the DM particle information at redshift of zero I determine the density ρ_i of the i^{th} DM particle using Smoothed Particle Hydrodynamics (SPH) kernel, which evaluates

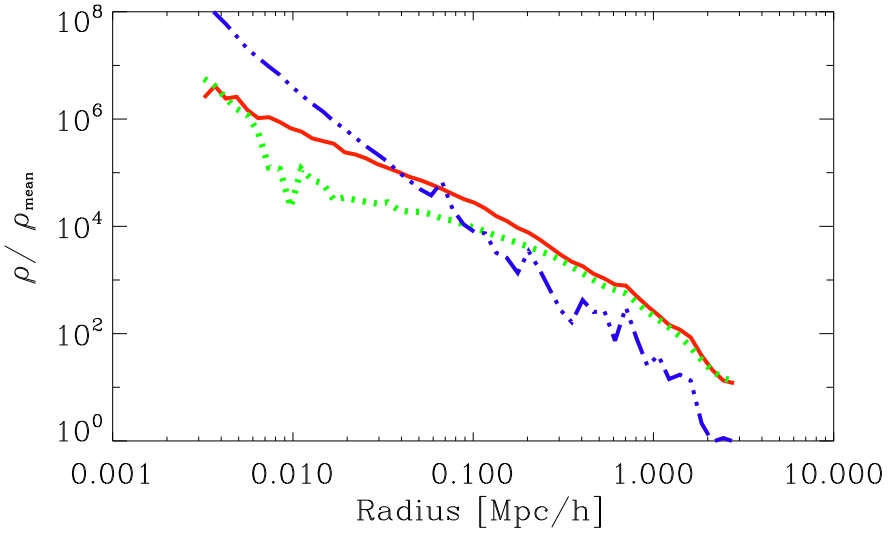


FIGURE 4.2: The density profile of DM, gas and stars in red, green and blue, respectively.

the density in a regular grid taking in to account the 44 neighboring particles (Springel, 2010). This allows us to easily compute the square of the DM densities integrated in the line-of-sight. In Fig. 4.3 I give the projected map of the DM density square values of a cluster 2 Mpc across that are obtained using SPH kernel. The brightest colors in the map clearly show enhanced DM density substructures which are required to correctly determine emissions from DM annihilation process in clusters.

4.4 Magnetic Field Models

In addition to the DM densities I also need to model the magnetic field (i.e., in case of synchrotron emission) to determine the DM annihilation signals. Thus I have considered using two magnetic field models in our work:

(i) Model A is a model that evaluate the magnetic field strength from DM particle densities. The magnetic field profile is given by

$$B(r) = B_0 \left(1 + (r/r_s)^2\right)^{-q_b}, \quad (4.2)$$

where B_0 is the central magnetic field strength, r is the radial distance from cluster center, r_s is the scale radius of the DM density profile and q_b is scaling exponent chosen to be 0.5 (Colafrancesco et al., 2015). As I wanted to determine the magnetic field strength in each cube of size 10 kpc, for each point in the simulation box I determine first their respective densities which will allow us to calculate the magnetic field as a function of the DM density in each cube.

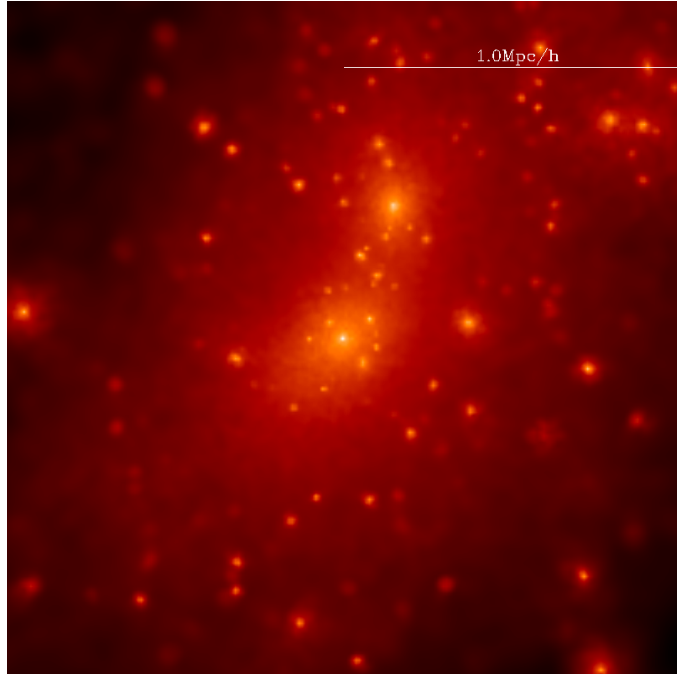


FIGURE 4.3: The DM density square map of one representative sample of clusters obtained using SPH kernel.

(ii) Models B is a magnetic field model which uses the best observational value for a central magnetic field in the Coma Cluster equal to $4.7 \mu\text{G}$ (at electron number density of $3.44 \times 10^{-3} \text{ cm}^{-3}$) from [Bonafede et al. \(2010\)](#). The magnetic field B of the galaxy cluster is related to the electron number density n_e by

$$B = 4.7 \mu\text{G} \left(n_e / 3.44 \times 10^{-3} \text{ cm}^{-3} \right)^{0.5}. \quad (4.3)$$

We evaluated the electron number density n_e in cm^{-3} as in [Sembolini et al. \(2013\)](#),

$$n_e = N_e \rho_{\text{gas}} (1 - Z - Y_{He}) / m_p, \quad (4.4)$$

where N_e , ρ_{gas} , Z , Y_{He} and m_p are the number of ionized electrons per hydrogen atoms, gas density, metallicity, helium concentration and proton mass, respectively.

The magnetic field profiles for these two magnetic field models discussed above are shown in Fig. 4.4. The radial profile of magnetic field Model A (dotted line in red color) shows a very close value to the central magnetic field value of $B_0 = 5.0 \mu\text{G}$ in the inner region of the cluster as it is constrained not to exceed this value. Because of over-cooling problem in the simulations, the central densities of baryon are unrealistically high, which cause unrealistically high magnetic field values from Model B (solid line in green color) in the inner region of the cluster. We will provide a more detailed discussion of this, in the light of synchrotron emission, in the next chapter (see Sec. 5.2). The two magnetic field models on the other hand show a fair agreement over a large volume of the cluster.

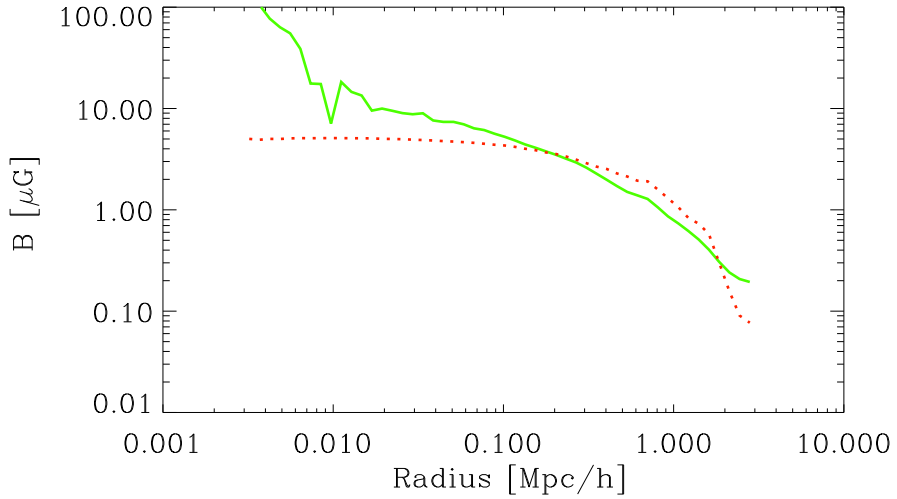


FIGURE 4.4: Magnetic field profiles of the two magnetic field models: Model A and Model B are shown in red dotted line and green solid line, respectively.

4.5 Electrons Equilibrium Spectra

In the above sections I have modeled the DM particle densities and the magnetic fields which are required to calculate the secondary electron/positron equilibrium spectra $\frac{dn_{e\mp}}{dE}$. Having said that, let us first describe the ‘source spectra’ on which the ‘electrons equilibrium spectra’ are based. The number of electrons and gamma-rays produced per unit time, energy and volume element at the position r from neutralino, χ , annihilation processes is called the ‘source spectra’. It is given by the product of the neutralino pair number density $\mathcal{N}_\chi(r)$, neutralino annihilation rate $\langle \sigma V \rangle$, the production spectra $\frac{dN_i^f}{dF}$ and branching ratio B_f , i.e.,

$$Q_i(E, r) = \langle \sigma V \rangle \sum_f \frac{dN_i^f}{dE} B_f \mathcal{N}_\chi(r), \quad (4.5)$$

where i and f refer to the produced particle and the kinematically allowed annihilation final states each with branching ratio of B_f , respectively. The neutralino pair number density $\mathcal{N}_\chi(r)$ can be expressed as $\rho_{DM}^2/2m_\chi^2$, where the factor 2 in the denominator appears to take into account the annihilating pairs. The production spectra $\frac{dN_i^f}{dF}$ is obtained using DarkSUSY package ([Gondolo et al., 2004](#)).

The ‘electrons equilibrium spectra’ themselves are obtained from the ‘source spectra’ of the injected electrons by considering their energy loss by different mechanisms, and their spatial diffusion process as they pass through the atmosphere of the DM halo ([Longair, 1994](#)). This process is governed by the diffuse equation in the following form:

$$\frac{\partial}{\partial t} \frac{dn_e}{dE} = \nabla \left(D(E, r) \nabla \frac{dn_e}{dE} \right) + \frac{\partial}{\partial E} \left(b(E, r) \frac{dn_e}{dE} \right) + Q_e(E, r), \quad (4.6)$$

where $\frac{dn_e}{dE}$ is the electron/positron spectrum, $D(E, r)$ diffusion coefficient, $b(E, r)$ the energy loss factor and $Q_e(E, r)$ the electron ‘source spectra’.

A generic solution to the diffusion equation which in the case of galaxy clusters, where the effect of diffusions of electrons are negligible, is given by [Colafrancesco et al. \(2006\)](#). This solution which is the ‘electrons equilibrium spectra’ has the form:

$$\frac{dn_e}{dE} = \frac{1}{b(E)} \int_E^{M_\chi} Q_e(E', r) dE', \quad (4.7)$$

where E is the energy of the electrons and $b(E)$ is the energy loss term which is the sum of effects due to IC, synchrotron radiation, Coulomb losses and bremsstrahlung radiation ([Colafrancesco et al., 2006](#)). The ‘electrons equilibrium spectra’ can then be used in Eqns. [4.11](#), [4.18](#) and [4.22](#) to calculate the local emissivities and ultimately the fluxes. In the following sections I will formulate the required equations needed to calculate the radio and gamma-ray emissions from DM annihilation processes in galaxy clusters.

4.5.1 Synchrotron Emission Processes

Diffuse radio emission has been observed in a large number of clusters which is not associated with galaxies. The distribution of magnetic field, and energetic electrons in the wider region of galaxy clusters is believed to produce synchrotron radiation. Synchrotron radiation is emitted when an electron gyrates about magnetic field lines. For an amplitude of magnetic field B the average power radiated by electrons with an energy E from synchrotron processes at frequency ν is formulated as in [Longair \(1994\)](#):

$$P_{synch}(\nu, E, r, z) = \int_0^\pi d\theta \frac{\sin \theta^2}{2} 2\pi \sqrt{3} r_e m_e c \nu_g F_{synch} \left(\frac{\kappa}{\sin \theta} \right), \quad (4.8)$$

where m_e is the electron mass, $\nu_g = \frac{eB}{2\pi m_e}$ is the non-relativistic gyro-frequency, $r_e = \frac{e^2}{m_e c^2}$ is the classical electron radius, and the quantities κ and F_{synch} are defined as

$$\kappa = \frac{2\nu(1+z)}{3\nu_0 \gamma^2} \left(1 + \left(\frac{\gamma \nu_p}{\nu(1+z)} \right)^2 \right)^{\frac{3}{2}}, \quad (4.9)$$

and

$$F_{synch}(x) = x \int_x^\infty dy K_{5/3}(y) \simeq 1.25 x^{\frac{1}{3}} e^{-x} (648 + x^2)^{\frac{1}{12}}. \quad (4.10)$$

One can obtain the local synchrotron emissivity as a function of electron or positron equilibrium distribution and synchrotron power P_{synch} as

$$j_{synch}(\nu, r, z) = \int_{m_e}^{M_\chi} dE \left(\frac{dn_{e^-}}{dE} + \frac{dn_{e^+}}{dE} \right) P_{synch}(\nu, E, r, z). \quad (4.11)$$

The quantity $\frac{dn_{e^\mp}}{dE}$ is the electron or positron equilibrium spectra obtained after accounting for the energy loss of electron through the atmosphere of the galaxy cluster as the sum of effects such as inverse Compton, synchrotron emission, Coulomb losses and bremsstrahlung processes (see for e.g., Colafrancesco et al. (2006); Colafrancesco et al. (2015)).

Using the local synchrotron emissivity I I can express the flux density within radius r as follows:

$$S_{synch}(\nu, z) = \int_0^r d^3r' \frac{j_{synch}(\nu, r', z)}{4\pi D_L^2}, \quad (4.12)$$

where D_L is the luminosity distance to the halo.

4.5.2 Gamma-ray Emission Processes

In a DM annihilation process gamma-rays can be produced from pion decay, IC scattering and non-thermal bremsstrahlung processes. In the following I will briefly describe these processes and the formulation used to calculate the gamma-ray flux.

Pion Decay

When DM annihilation process produces neutral pions, these unstable particles decay into gamma-rays whose spectrum obeys a power law, i.e., they decay into less number of gamma-rays per energy of the photons at higher frequencies. The differential gamma-ray flux density from pion decay is then obtained by considering the annihilating DM pairs with mass M_χ , their velocity averaged annihilation cross-section $\langle \sigma V \rangle$ and integrating over volume integral of the DM density ρ_{DM} square along the line of site divided by area. Hence the differential flux which is number of gamma-ray photons per area per time and per energy at luminosity distance D_L is given by

$$\frac{dF}{dE} = \frac{\langle \sigma V \rangle}{2M_\chi^2} \frac{dN}{dE_\gamma} \int_0^r \frac{\rho_{DM}^2 dV}{4\pi D_L^2}, \quad (4.13)$$

where $\frac{dN}{dE_\gamma}$ is the initial gamma-ray spectrum which is obtained using DarkSUSY package (Gondolo et al., 2004). The gamma-ray flux from pion decay can then be obtained by integrating Eqn. 4.13 over E_γ , the energy of gamma-ray photons producing the gamma-ray spectrum.

IC Scattering Process

Relativistic electrons produced from charged pion from DM annihilation process scatter CMB photons and boost them to gamma-ray. The average IC power is given by

$$P_{IC}(E_\gamma, \gamma, r) = c E_\gamma \int_0^\infty d\epsilon n(\epsilon) \sigma(E_\gamma, \epsilon, \gamma), \quad (4.14)$$

where $n(\epsilon)$ is the black body spectrum of the CMB photons, and $\sigma(E_\gamma, \epsilon, \gamma)$ is the IC scattering cross-section given in [Longair \(1994\)](#) as

$$\sigma(E_\gamma, \epsilon, \gamma) = \frac{3\sigma_T}{4\epsilon\gamma^2} G(q, \Gamma_e), \quad (4.15)$$

where σ_T is the Thompson cross-section, γ is the electron Lorentz factor, and

$$G(q, \Gamma_e) = \left[2q \ln q + (1+2q)(1-q) + \frac{(\Gamma_e q)^2(1-q)}{2(1+\Gamma_e q)} \right], \quad (4.16)$$

with

$$\Gamma_e = 4\epsilon\gamma/(mc^2), q = E_\gamma/[\Gamma_e(\gamma mc^2 - E_\gamma)]. \quad (4.17)$$

The local emissivity is obtained by integrating the product of IC scattering power $P_{IC}(E_\gamma, \gamma, r)$ and electron equilibrium spectrum $N_e(\gamma, r)$ across all electron energy as

$$j_{IC}(E_\gamma, r) = \int_{\gamma_{min}}^{\gamma_{max}} d\gamma N_e(\gamma, r) P_{IC}(E_\gamma, \gamma, r). \quad (4.18)$$

The flux of gamma-rays from IC scattering process at luminosity distance D_L can then be calculated by

$$S_{IC}(E_\gamma) = \int_0^r d^3r' \frac{j_{IC}(E_\gamma, r')}{4\pi D_L^2}. \quad (4.19)$$

Non-thermal Bremsstrahlung Radiation

Non-thermal bremsstrahlung process produces gamma-rays radiations when secondary electrons are slowed by the electrostatic field of ions in the ICM and inter-stellar medium (ISM). The average power of non-thermal bremsstrahlung emission is calculated by considering the number density of ions $n_j(r)$

$$P_B(E_\gamma, \gamma, r) = cE_\gamma \sum_j n_j(r) \sigma_j(E_\gamma, E), \quad (4.20)$$

where the interaction cross-section is given in [Longair \(1994\)](#) as

$$\sigma(E_\gamma, E) = \frac{3}{8\pi} \alpha \sigma_T \left\{ \left[1 + \left(1 - \frac{E_\gamma}{E} \right)^2 \right] \phi_1 - \frac{2}{3} \left(1 - \frac{E_\gamma}{E} \right) \phi_2 \right\}, \quad (4.21)$$

with

$$\phi_u = 4 \left\{ \ln \left[\frac{2E}{mc^2} \left(\frac{E - E_\gamma}{E_\gamma} \right) \right] - \frac{1}{2} \right\}.$$

The local emissivity is obtained by integrating the product of IC scattering power $P_B(E_\gamma, \gamma, r)$ and electron equilibrium spectrum $N_e(\gamma, r)$ across all electron energy as

$$j_B(E_\gamma, r) = \int_{\gamma_{min}}^{\gamma_{max}} d\gamma N_e(\gamma, r) P_B(E_\gamma, \gamma, r). \quad (4.22)$$

The gamma-ray flux from non-thermal bremsstrahlung process at luminosity distance D_L is determined in a similar fashion to the above emission mechanisms by using the local emissivity as in

$$S_B(E_\gamma) = \int_0^r d^3r' \frac{j_B(E_\gamma, r')}{4\pi D_L^2}. \quad (4.23)$$

4.6 Summary

In this chapter I have presented the semi-analytical DM models, based on high resolution cosmological simulations of galaxy clusters, which will be used to calculate the radio and γ -ray emissions believed to be produced via neutralino DM annihilation processes in galaxy clusters. The fluxes which are determined using Eqn. 4.12 (for radio emissions) and Eqns. 4.13, 4.19 and 4.23 (for γ -ray emissions) will then provide vital information for an indirect detection of neutralino DM via their annihilation process, as they can be detected using sensitive telescopes tuned in the appropriate frequency range. In Chapter 5 and 6 I will provide the results of these predictions in galaxy clusters and high mass-to-light ratio DM dominated sub-halos, respectively.

Chapter 5

Multi-wavelength Emission from DM Annihilation Processes in Galaxy Clusters

5.1 Introduction

I base my studies of synchrotron and γ -ray emissions from DM annihilation processes in galaxy clusters by taking neutralinos to be primarily and dominantly composed of $b\bar{b}$ species and light and intermediate DM mass models as in [Colafrancesco et al. \(2011a\)](#). Thus I consider neutralinos mass of M_χ , 35 and 60 GeV taking the thermally averaged DM annihilation cross-section times velocity, $\langle\sigma V\rangle$, to be $1.0 \times 10^{-26} \text{ cm}^3 \text{ s}^{-1}$ from Fermi upper limit [Ackermann et al. \(2014\)](#). The synchrotron/radio and γ -ray emissions results obtained from DM annihilation processes in galaxy clusters will be presented in the following sections. The emission maps are generated based on the data set available from MUSIC cluster ([Sembolini et al., 2013](#)), a high-resolution cosmological simulation containing DM, gas, stars and feedback mechanisms. The emission maps are produced by dividing a 3-D cluster of 2 Mpc across into cubes of size 10 kpc. The synchrotron emission result will be presented along with the discussion in the first part of this chapter. The synchrotron emission calculations were made using the formulation given in Section 4.5.1 and the two magnetic field models (Model A and Model B) discussed in Section 4.4. In the second part of this chapter I will give the γ -ray emissions results along with their discussions. The γ -ray emission calculations were made using the formulations given in Section 4.5.2 by considering all the three relevant processes (i.e., pion decay, IC scattering and non-thermal bremsstrahlung radiation processes).

5.2 Radio Emission from DM Annihilation Processes in Galaxy Clusters

These synchrotron emission maps given in Figs. 5.1 and 5.2 show the radio flux values in units of Jy at 110 MHz and 1.4 GHz frequencies. These two frequencies were chosen to represent the SKA-low and SKA-mid frequencies. The synchrotron emission maps in both Figs. 5.1 and 5.2 are obtained using magnetic fields of model A. The central

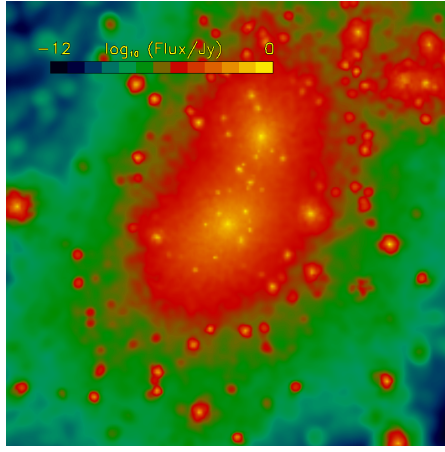


FIGURE 5.1: Radio emission map at 110 MHz using magnetic field of Model A and neutralino mass of 60 GeV.

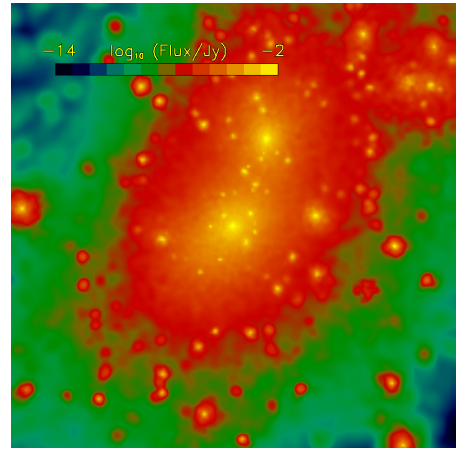


FIGURE 5.2: Radio emission map at 1.4 GHz using magnetic field of Model A and neutralino mass of 60 GeV.

region of the cluster in these maps shows a strong radio flux which is indicated in the brightest color in the color bar, this resulted because of having larger values of DM densities in these regions. The synchrotron emission flux calculation is able to resolve the contribution from DM dominated regions in the cluster, thus halos and substructures that are residing off center are clearly visible in the maps. The maps also show the presence of two main halos in the cluster which are approximately 0.5 Mpc apart.

Comparison between Fig. 5.1 and 5.2 (i.e., maps that are produced at 110 MHz and 1.4 GHz frequencies, respectively) do not show any noticeable difference on the background structure of the emission apart from the difference in the output flux at the two frequencies. Point-by-point comparison between the two radio emission maps show flux values at 110 MHz (Fig. 5.1) varies between 9 to 80 times that of flux at 1.4 GHz (Fig. 5.2).

Fig. 5.3 shows radial variation of flux with radius. It is obtained from the flux values in the maps of Figs. 5.1 and 5.2, by picking the flux values starting from the center of the map and moving to the bottom of the map. The variations in flux shown in these profiles indicate the flux from substructures are more dominant especially in the outer part of the cluster. The two solid lines in the top part of the figure are obtained for frequency of 110 MHz, and the bottom ones in the dotted lines are for frequency of 1.4 GHz. The flux profiles obtained with the two magnetic field models are indicated as Model A in red color and Model B in black color, respectively. In the inner region of the cluster the flux values based on Model A are slightly lower than that based on Model B and vice versa in the outer region. This is due to the magnetic field values of Model B which have higher values in the inner region of the cluster as shown in Fig. 4.4.

In Figs. 5.4 and 5.5 I provide emission maps for synchrotron processes that mimic the radio flux expected at SKA-low and SKA-mid frequencies detection limits using magnetic field of Model A. The maps are produced by subtracting out the sensitivity limit of SKA-low and SKA-mid at frequency 110 MHz and 1.4 GHz respectively. Both Figs. 5.4 and 5.5 show strong flux as indicated by the brightest color in the map coming from the dense central region of the cluster as well as substructures that are off center where the DM annihilation process is expected to be dominant.

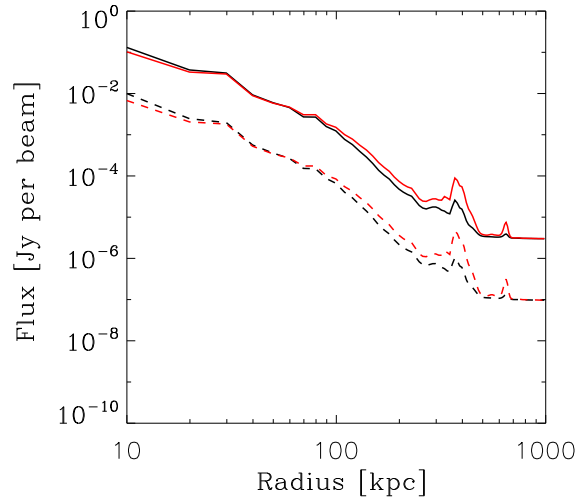


FIGURE 5.3: Flux profiles at 110 MHz (solid lines) and 1.4 GHz frequencies (dotted lines) obtained using magnetic field Model A (in red color) and Model B (in dark color) for neutralino mass of 60 GeV.

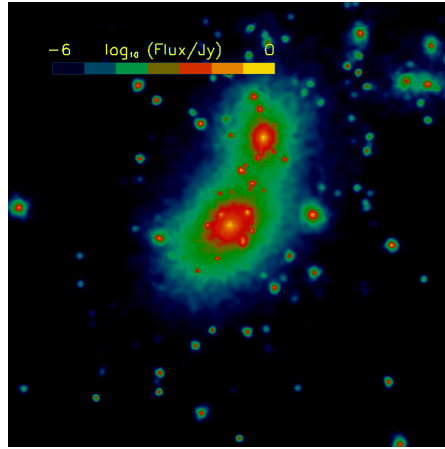


FIGURE 5.4: Radio emission map at 110 MHz with SKA-low sensitivity using magnetic field of Model A and neutralino mass of 60 GeV.

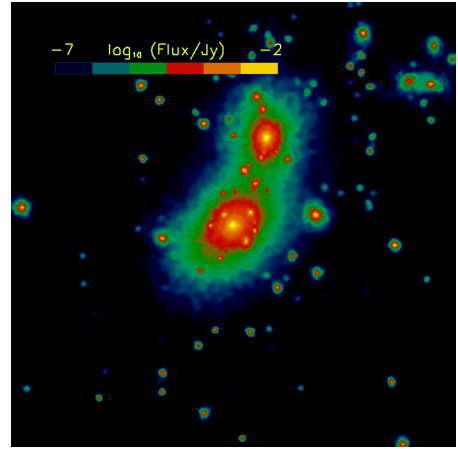


FIGURE 5.5: Radio emission map at 1.4 GHz with SKA-mid sensitivity using magnetic field of Model A and neutralino mass of 60 GeV.

In order to explore better the difference in the emission maps that are obtained using the two magnetic field models, I produce maps in Figs. 5.6 and 5.7 that are obtained using magnetic field Model B. A closer look between maps in Figs. 5.1 and 5.6 and/or Fig. 5.2 and 5.7 shows the emission maps obtained by taking magnetic field model A and B respectively shows the following difference. That is, the flux in the emission map of Figs. 5.6 and 5.7 are dominated with the flux from the central region of the cluster which is in contrast to a competitive emission observed coming from various points in the cluster as in maps of Figs. 5.1 and 5.2. A point-by-point comparison between the

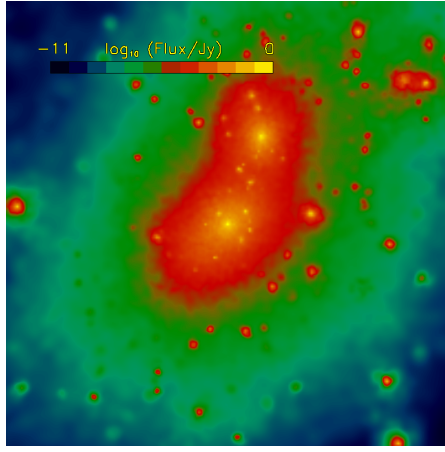


FIGURE 5.6: Radio emission map at 110 MHz using magnetic field of Model B and neutralino mass of 60 GeV.

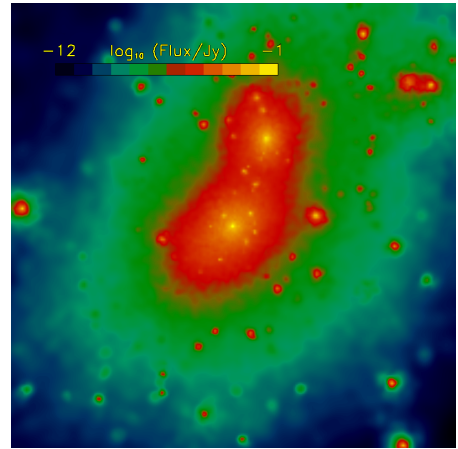


FIGURE 5.7: Radio emission map at 1.4 GHz using magnetic field of Model B and neutralino mass of 60 GeV.

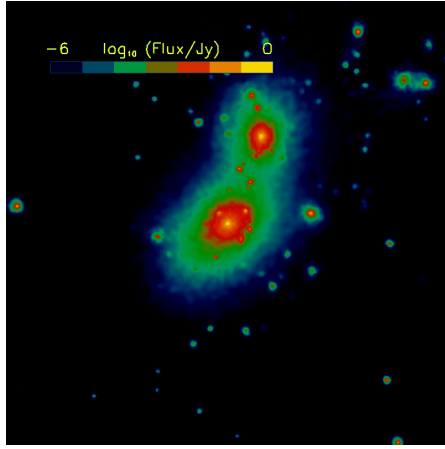


FIGURE 5.8: Radio emission map at 110 MHz with SKA-low sensitivity using magnetic field of Model B and neutralino mass of 60 GeV.

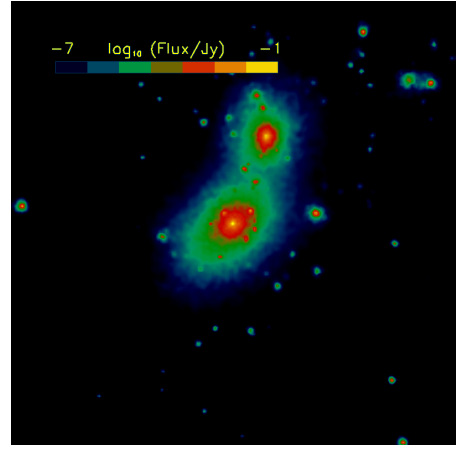


FIGURE 5.9: Radio emission map at 1.4 GHz with SKA-mid sensitivity using magnetic field of Model B and neutralino mass of 60 GeV.

two radio emission maps shows flux values at 110 MHz (Fig. 5.6) varies between 5.66 and 37.8 times that of flux at 1.4 GHz (Fig. 5.7).

Maps of Figs. 5.8 and 5.9 are obtained based on magnetic field model B. They are produced by subtracting out the flux values below the instrument sensitivity limit of SKA-low and SKA-mid at frequency 110 MHz and 1.4 GHz respectively. On comparing these maps, with Figs. 5.4 and 5.5 which are produced using magnetic field Model A, I see very little contribution to the flux from halos and substructures that are off center.

For the neutralino mass of 60 GeV used, I have mentioned above that a point-by-point comparison between the two radio emission maps that are obtained using magnetic field model A shows flux at 110 MHz (Fig. 5.1) varies between 9 and 80 times that of flux at 1.4 GHz (Fig. 5.2). On the other hand the flux values obtained using magnetic field Model B (Figs. 5.6 and 5.7) varies with smaller values between 5.67 and 37.8. Hence, a

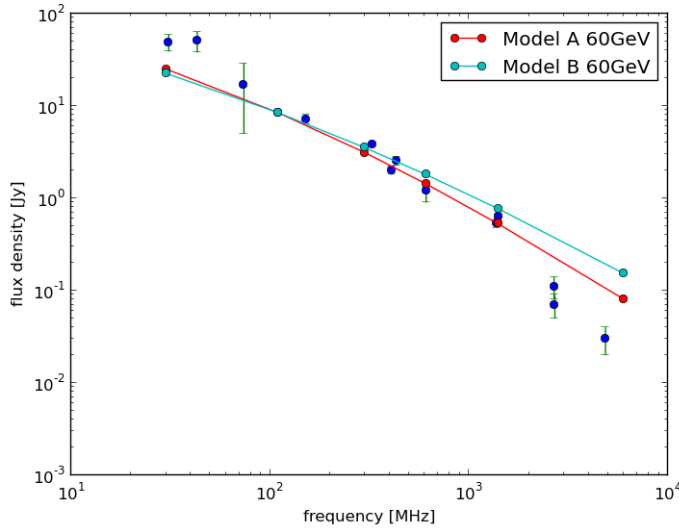


FIGURE 5.10: Flux density from synchrotron emission, taking mass of neutralino 60 GeV, with magnetic field Model A in red color and Model B in cyan color. The blue data points are the observational data of radio emission of Coma cluster from [Thierbach et al. \(2003\)](#).

flatter appearance of the flux density curve for magnetic field of Model B (cyan color) than that of Model A (red color) is observed as shown in Fig. 5.10.

We have also considered the case of neutralino mass of 35 GeV in our point-by-point comparisons. We have obtained the flux values in the emission maps of Figs. A.1 and A.2, which are obtained using magnetic field of Model A for the two frequencies of 110 and 1400 MHz, varies between 11.99 to 433, respectively. Whereas I obtained the flux variations for the emission maps which uses magnetic field Model B (Figs. A.3 and A.4) at the two frequencies of 110 and 1400 MHz, varies at smaller ranges of 6.98 to 77.17. To see what these variations obtained from point-by-point comparisons translate into, the spectral indexes of this four cases were calculated. Table 5.1 provides these results of our comparison of the spectral index for synchrotron flux densities that are calculated taking 110 and 1400 MHz frequencies for which I showed their emission maps in the above discussions. We found the highest negative value for spectral index of 35 GeV neutralino mass and magnetic field Model A as compared to that of 60 GeV neutralino mass and magnetic field Model A.

Neutralino Mass [GeV]	Magnetic Field Models	Spectral Index
35	Model A	-1.16
35	Model B	-0.98
60	Model A	-1.05
60	Model B	-0.91

TABLE 5.1: Comparison of the spectral index for radio flux densities using neutralino annihilation final product of $b\bar{b}$ species.

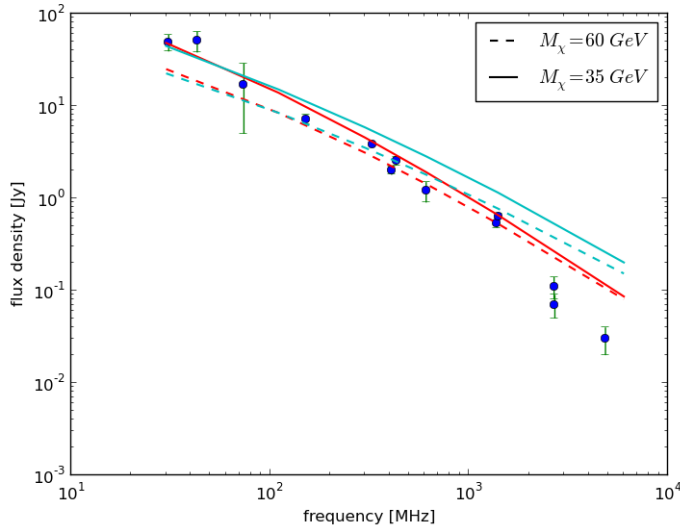


FIGURE 5.11: Flux density from synchrotron emission is compared with measured result of [Thierbach et al. \(2003\)](#), taking mass of neutralino 60 GeV, dotted lines and 35 GeV, solid lines. Magnetic field models used are indicated in red and cyan color for Model A and B, respectively.

In Fig. 5.11 I show the flux density from synchrotron emission in comparison with the observational data of radio emission from the Coma Cluster ([Thierbach et al., 2003](#)). Plots for the two masses of neutralinos used, 60 GeV and 35 GeV are indicated by dotted and solid lines. The magnetic field models, Model A and Model B, are shown in cyan and red color, respectively. As our result of the spectral index reflects in table 5.1 I see the steepest profile among the four cases for magnetic field Model A and 35 GeV neutralino mass. Hence the best fit to the observational result of [Thierbach et al. \(2003\)](#) is obtained taking neutralino mass of 35 GeV and magnetic field model A. This agreement was obtained without invoking any boost factor from DM substructures, which shows that the distribution of sub-structures is well described in the simulations and boosted the signals from DM annihilation processes exactly to the level of observed flux. Moreover, I have also observed the flux density for the radio halo spectrum obtained for neutralino mass of both $M_\chi = 60$ and 35 GeV as in Fig. 5.11 are flatter than the measured result of [Thierbach et al. \(2003\)](#) at higher frequency ranges. A more recent paper by [Marchegiani and Colafrancesco \(2016\)](#) has shown that the best agreement in the over all flux density spectrum is obtained using smaller values of neutralino mass of 9 GeV and magnetic field of Model B, this result can be tested by our model in the future.

We have made a deeper investigation to understand better why I see flatter flux spectrum when using magnetic field Model B by constraining the magnetic field values in Model B. That is, the flux densities for magnetic field Model B constrained are obtained by setting the magnetic field values which are above $7.0 \mu\text{G}$ to $7.0 \mu\text{G}$. As shown in Fig. 5.12 the flux densities of Model B constrained indicated in red line shows a steeper spectrum than that of Model B which is indicated in cyan color. We find that the high magnetic field effect of enhancing the radio flux density from the central region of the cluster is reduced by constraining the magnetic field as shown by using Model B constrained in the red line. This arise as some values of the radio flux densities at higher frequencies

get shifted to the values at lower frequencies. Over all this shows us both magnetic field models, Model A and Model B, are able to reproduce the radio flux spectrum. It is worth mentioning why I have not constrained the magnetic field according to the “beta-model”. The reason is that for the calculation of magnetic field using the electron density from the MUSIC simulation I wanted to see its variation following the gas density or equivalently the electron number density in through out the cluster (thus free from constraint).

However, the “beta-model” [Cavaliere and Fusco-Femiano \(1976\)](#) which is believed to trace well the distribution of the gas in the ICM (for more see discussion under Section [3.3.2](#)), uses the gas densities that are constrained with the relation in Eqn. [5.1](#) obtained from rotation measures

$$n(r) = n_{el,0} \left(1 + (r/r_c)^2\right)^{-\frac{3}{2}\beta}, \quad (5.1)$$

where β is a constant, $n_{el,0}$ is the central gas density, r is the radial distance from cluster center and r_c the cluster core radius.

It is worth mentioning the fact these simulated clusters I have used to study the DM annihilation processes in galaxy clusters, from the MUSIC cluster simulations, in general show higher values of gas densities in their central regions as they suffer from over cooling. Thus they give larger values of magnetic field based on the formulation of Eqn. [4.3](#). Despite this drawback the magnetic field calculations based on electron densities of magnetic field Model B show a fair agreement in large part of the cluster volume. In addition to this the formulation in Eqn. [4.3](#), unlike the electron number densities constrained as in Eqn. [5.1](#), will allow us to apply our magnetic field calculations for all the 282 clusters I studied. This simple modification I made thus has the following advantages: (i) it is able to give magnetic field values at each grid as compared to the constrained model which follows radial variation which assumes spherical symmetry in the cluster, (ii) it reduces model dependencies and, (iii) it allows a robust study of both magnetic field and emission processes from DM annihilation processes. Moreover, modeling the DM distribution as a single spherically symmetric halo does not reproduce the observed shape of the radio halo surface brightness ([Marchegiani and Colafrancesco, 2016](#)). This problems faced by previous DM models can be resolved by modeling the distribution of sub-structures more realistically. Our semi-analytical model which is based on high-resolution cosmological simulations, for example, can address this issue. Our results show the expected features emerging from a realistic distribution of DM sub-structures as shown in the emission maps, and their contribution to the overall DM annihilation signals in clusters.

5.3 Gamma-ray Emissions from DM Annihilation Processes in Galaxy Clusters

We have produced γ -ray emission maps and calculated the γ -ray flux densities by considering all important processes: pion decay, Inverse Compton (IC) scattering and non-thermal bremsstrahlung radiation processes (see Section [4.5.2](#)). Based on the result of Fig. [5.11](#) I chose neutralino mass $M_\chi = 35$ GeV and composition of $b\bar{b}$ which is the best fitting DM species and mass for DM annihilation models has also been suggested

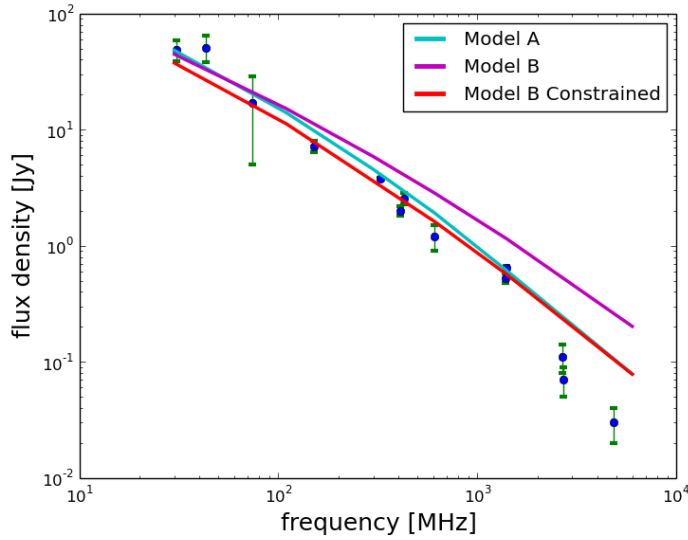


FIGURE 5.12: Flux density of synchrotron emission process for neutralino mass of 35 GeV (solid lines) is compared with observational result of the Coma Cluster (blue data points) from [Thierbach et al. \(2003\)](#). Magnetic field models used are indicated in cyan, magenta and red colors for Model A, Model B, and Model B constrained, respectively.

by the data of cosmic ray antiproton spectrum obtained by PAMELA ([Hooper et al., 2015](#)) which is in agreement with the result of [Marchegiani and Colafrancesco \(2016\)](#). In the following I provide the results obtained along with the discussion.

Figs. 5.13 and 5.14 show the gamma-ray emission maps obtained from non-thermal bremsstrahlung process at a photon energy of 100 MeV. These two gamma-ray emission maps are obtained using a varying thermal electron density assumed for the protons as given in Eqn. 4.4 from reference [Sembolini et al. \(2013\)](#) and a constant central electron density of the Coma Cluster $n_{e0} = 3.4 \times 10^{-3} \text{ cm}^{-3}$, respectively. We have used this central value of n_{e0} only for the purpose of comparison. The gamma-ray flux emanating from the dense central point of the cluster, shown in bright color of Fig. 5.13, is 10 times larger than that of Fig. 5.14, which resulted from the non-thermal bremsstrahlung power dependence on the thermal electron number density that has its peak in the center of the cluster. In Fig. 5.14 it is apparent to see a wide variation (11 orders of magnitude, 10^{-24} to 4×10^{-13}) between lower and higher values of differential gamma-ray flux in the color bar.

The gamma-ray emission maps obtained from pion decay and IC scattering processes at a photon energy of 100 MeV are shown in Figs. 5.15 and 5.16, respectively. The magnitude of the flux obtained from IC scattering processes is 15 orders of magnitude less than that of pion decay at gamma-ray photon energy of 100 MeV. It is expected that for neutralino mass used, 35 GeV, the IC scattering contribution is negligible above photon energy of 10 MeV.

We can also observe the energy dependence of the gamma-ray emission from the gamma-ray flux obtained at 1 and 10 GeV gamma-ray photon in Fig. 5.17 and 5.18, respectively.

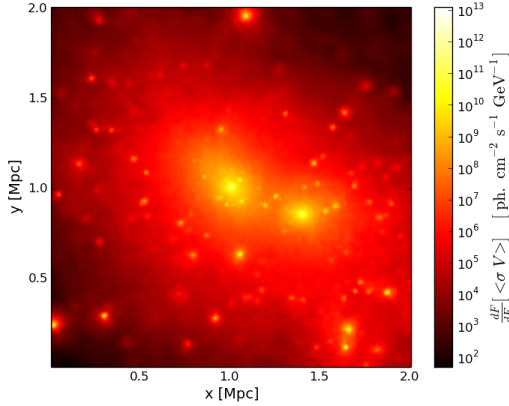


FIGURE 5.13: Gamma-ray from non-thermal bremsstrahlung process at 100 MeV using radially varying thermal electron density from reference [Sembolini et al. \(2013\)](#) in units of $\langle \sigma V \rangle$.

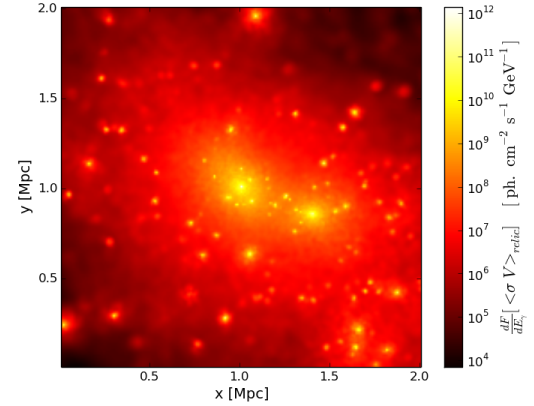


FIGURE 5.14: Gamma-ray from non-thermal bremsstrahlung process at 100 MeV using a constant average thermal electron density of the Coma Cluster. We have produced this emission map only for comparison.

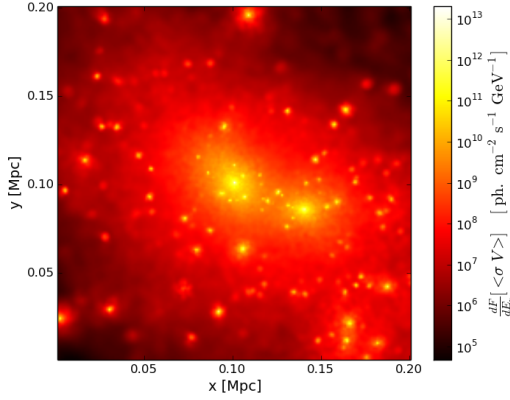


FIGURE 5.15: Gamma-ray from pion decay processes at 100 MeV in units of $\langle \sigma V \rangle$.

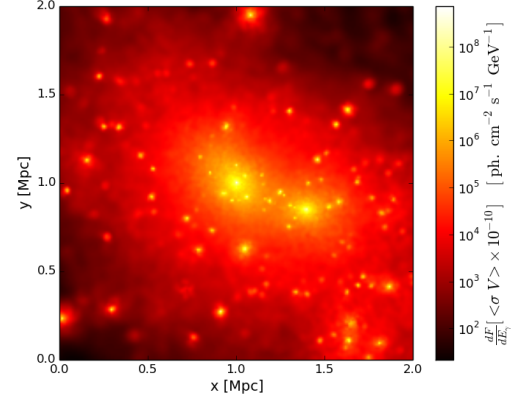


FIGURE 5.16: Gamma-ray emission from IC scattering process at 100 MeV in unit of $10^{-10} \langle \sigma V \rangle$.

The later map shows gamma-ray emissions mostly coming from relatively denser subhalos and 3 orders of magnitude less value of flux as compared to the gamma-ray flux in the former map.

In Fig. 5.19 I show the differential gamma-ray flux densities obtained from pion decay, non-thermal bremsstrahlung and IC scattering processes indicated in blue, green and pink colors, respectively. The frequencies range on the x-axis starts at mass of electron 0.511 MeV to a complete annihilation/decay of neutralino mass of 35 GeV used. The contribution of the gamma-ray flux from IC dominates at lower energies followed by bremsstrahlung process. At about 35 MeV pion decay takes over until it decays completely at the mass of neutralino 35 GeV. The shape of spectra obtained here for neutralino mass of 35 GeV and composition $b\bar{b}$ is in agreement with the recent work in reference [Marchegiani and Colafrancesco \(2016\)](#) of a similar (intermediate range) neutralino mass of 43 GeV composition $b\bar{b}$.

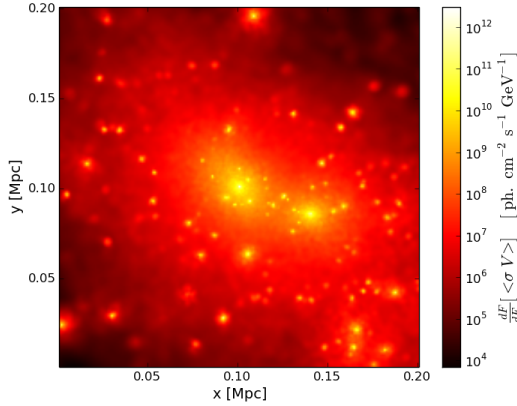


FIGURE 5.17: Gamma-ray from pion decay processes at 1 GeV in unit on the relic cross-section .

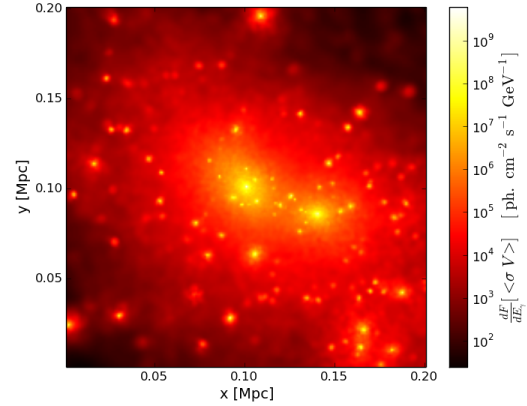


FIGURE 5.18: Gamma-ray from pion decay processes at 10 GeV in unit on the relic cross-section.

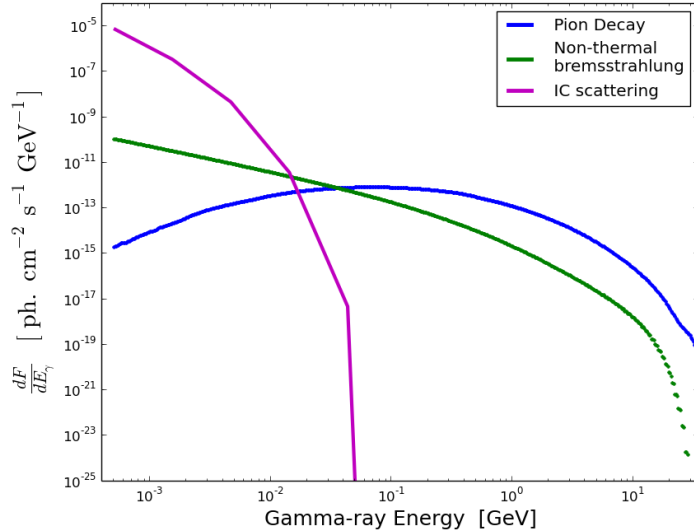


FIGURE 5.19: Differential gamma-ray flux densities from pion decay, non-thermal bremsstrahlung and IC scattering processes is given in the plot with blue, green and pink colors, respectively.

In table 5.2 I provide comparison of γ -ray integrated flux above 100 MeV, 1 GeV, and 10 GeV with the Fermi upper limits given in Ackermann et al. (2014); Ackermann et al. (2016). Our integrated γ -ray flux values are roughly 4 orders of magnitude less than the Fermi upper limits for the γ -ray energies above 0.1 and 10 GeV, and 3 orders of magnitude lesser for γ -ray energy above 1 GeV. Our integrated γ -ray flux result thus does not contradict with the constraint obtained from Fermi measurements.

Band GeV	Upper limit cm ⁻² s ⁻¹	Flux (35 GeV model) cm ⁻² s ⁻¹
> 0.1	4.2×10^{-9}	4.0×10^{-13}
> 1	1.13×10^{-10}	1.02×10^{-13}
> 10	6.0×10^{-12}	5.72×10^{-16}

TABLE 5.2: Gamma-ray upper limits set by Fermi for energies above 0.1 GeV ([Ackermann et al. \(2014\)](#)), 1 and 10 GeV ([Ackermann et al. \(2016\)](#)) and the comparison with our flux calculation using neutralino mass of 35 GeV and $b\bar{b}$ species.

5.4 Summary

In this chapter I have presented the results that were obtained for radio (synchrotron) and γ -ray emission from DM annihilation processes in galaxy clusters based on MUSIC cosmological simulation of galaxy clusters. We have calculated the synchrotron emission using magnetic field models that are determined from DM (Model A) and gas (Model B) properties. For neutralino velocity averaged annihilation cross-section, $\langle \sigma V \rangle$, of $1.0 \times 10^{-26} \text{ cm}^3 \text{ s}^{-1}$ I have compared cases of neutralino masses of 60 GeV and 35 GeV. We have obtained best fit to the observed flux density of Coma Cluster when using magnetic field Model A and DM mass of 35 GeV. This agreement was obtained without invoking any boost factor from DM substructures, which shows that the distribution of sub-structures is well described in the simulations and boosted the signals from DM annihilation processes exactly to the level of observed flux. The synchrotron emission maps also show an expected shape of radio halo surface brightness. I have also investigated deeply to understand why the spectrum gets flatter upon using magnetic field Model B. As was discussed based on the result of Fig. 5.12, the high magnetic field effect which is observed to enhance the radio flux density from the central region of the cluster can be reduced by constraining the magnetic field of Model B. Consequently some values of the radio flux densities at higher frequencies get shifted to the values at lower frequencies. Thus it can be deduced that both magnetic field models are equally applicable to reproduce both the morphology of radio halos in galaxy clusters and their flux spectrum.

For the same neutralino parameters given above I have also studied the gamma-ray emissions from pion decay, non-thermal bremsstrahlung and IC scattering processes. Our predictions show that the contribution to the overall gamma-ray flux density from IC dominates at lower energies. And the non-thermal bremsstrahlung will be the most prominent emission mechanism at intermediate gamma-ray energies, whereas at energies above ~ 35 MeV the pion decay process dominates. Moreover, the integrated gamma-ray flux densities do not exceed, thus not contradict with, the upper limits given by Fermi.

Taking advantage of the high resolution and large numbers of samples (282 clusters and thousands of groups) of the MUSIC clusters, in Chapter 6 I will focus on the study of the statistics and multi-wavelength emissions in DM sub-halos where the DM annihilation signals are expected to exceed ordinary emission (contaminating emissions from baryons which are not generated by DM annihilation process).

Chapter 6

Statistical Studies and Multi-wavelength Emissions from DM Annihilation Processes in DM Dominated Sub-halos

6.1 Introduction

When two galaxy clusters undergo merger they will leave the DM structure physically separated from the gas and stars (see for e.g., [Markevitch et al., 2004](#), and references therein). The DM structure resides in the outer part of the cluster making it a very suitable place to look for the DM annihilation signals. Another promising target to study DM annihilation emission process is to focus on DM sub-halos which contain very small proportions of gas and stars, or if possible DM sub-halos that are entirely devoid of gas and stars. Here I will consider the latter option to help us understand about the mysterious nature of DM using information obtained in the multi-wavelength emissions from self-annihilating neutralino DM particles using cosmological simulation.

The sub-halos are identified with a very efficient halo finder known as Rockstar, which make use of seven dimensions of information (phase space, (position and velocity) and time), [Behroozi et al. \(2013\)](#). Rockstar halo finder provides different halo properties, such as the halo masses at several radius, halo radius, halo center position and velocity, halo spin and angular momentum, etc. From all the 282 MUSIC clusters, a total of 466,621 sub-halos were found. Using the above mentioned properties those sub-halos containing a small fraction of gas and stellar content, which are dominantly composed of DM are isolated. As a primary test I over-plot the DM sub-halos in the region of the emission maps, cluster 2 Mpc across, discussed in the last chapter as shown in Fig. 6.1. These DM sub-halos, which are plotted in the filled black dots on the top of the synchrotron emission map, fit the brightest spot where the DM density enhancement is expected to be observed. I have also calculated the mass-to-light ratio (M/L) (i.e., the sum of the masses of gas, DM and star particles divided by the mass of the star particles) for each of these sub-halos in the cluster which are shown in the map of Fig. 6.1.

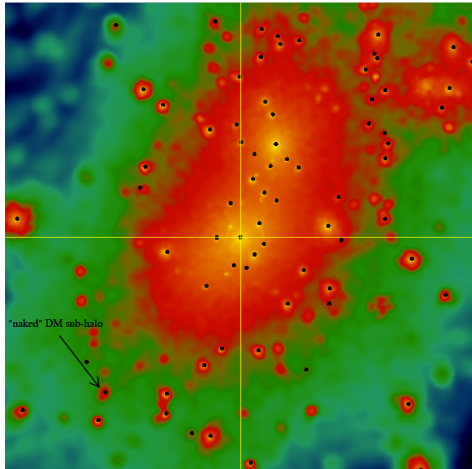


FIGURE 6.1: Identifying the DM sub-halos filled black dots on the top of the synchrotron emission.

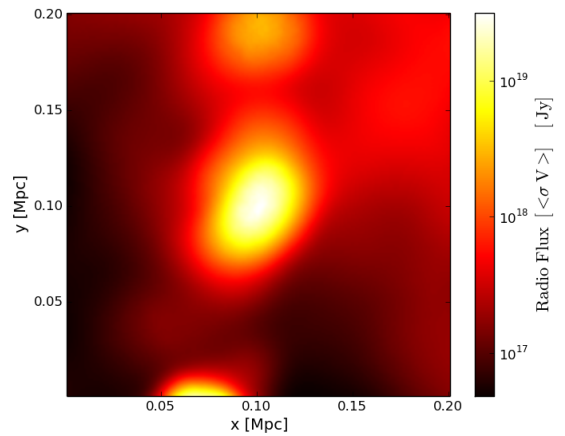


FIGURE 6.2: Synchrotron emission map at 110 MHz for the DM dominated sub-halo indicated by the arrow in Fig. 6.1.

From the over-plotted DM sub-halos in Fig. 6.1, for example, I conclude that having high M/L is not the only criteria required to single out promising DM sub-halos (i.e., targets where DM signals are expected to exceed ordinary emission). This is because sometimes tidal disruption can lead to having DM sub-halo like structure showing higher M/L value in the simulation. Thus it is important to look into the particle distribution of each DM sub-halo in a cubic section to see if the halos have better enhancement in their DM distribution. In doing so, the halo in third quadrant of the map (lower left) indicated by the arrow stand out to be the best candidate to study synchrotron emission from the DM annihilation process. This halo has M/L of 30.55, a gas fraction of $\sim 0.5\%$, stellar fraction of $\sim 3\%$ and shows a better enhancement in the DM distribution of all halos in the map.

For neutralino mass $M_\chi = 35$ GeV, DM annihilation cross-section $\langle \sigma V \rangle = 1.0 \times 10^{-26}$ $\text{cm}^3 \text{ s}^{-1}$ and magnetic field Model A discussed in Section 4.4, I produce synchrotron emission map for this DM sub-halo analyzed above. This high resolution ($L_x = L_y = 1$ kpc, and $L_z = 10$ kpc) emission map (0.2 Mpc across) is obtained by taking the DM sub-halo's central coordinates for its center. The synchrotron emission map at frequency of 110 MHz is shown in Fig. 6.2, the flux ranges from 4.79×10^{-10} to 3.16×10^{-7} Jy as shown in the color bar. The flux density for this DM sub-halo is given in Fig. 6.3, a rough comparison shows that it is in the range of SKA sensitivity limit (I will discuss this in depth at the end of section 6.4). The comparison of shape and slope of the flux density of this DM sub-halo with the host cluster and the Coma Cluster data of Thierbach et al. (2003), is given in Fig. 6.4. The scaled synchrotron flux spectrum of the DM sub-halo (red line) is steeper than its host (cyan line). Thus scaled DM sub-halo spectrum shows a better fit to the observational data of diffuse radio spectrum of the Coma Cluster (blue dots). To understand well the DM annihilation process and its signals from DM sub-halos I increased the samples by considering all the DM sub-halos in all the 282 MUSIC clusters. I will present results and discussion of the statistical and multi-wavelength studies of the high M/L DM sub-halos in the light of DM annihilation process in the proceeding sections.

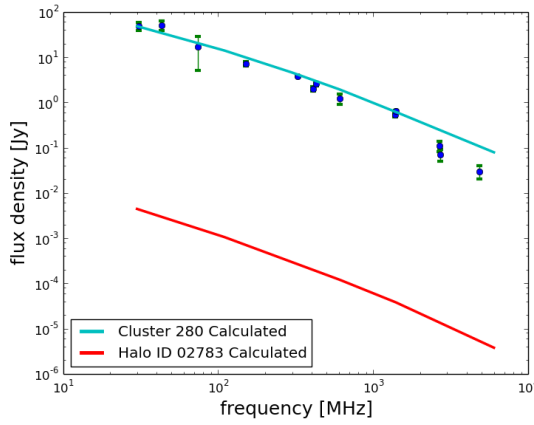


FIGURE 6.3: Radio flux density from the DM dominated sub-halo indicated by the arrow in Fig. 6.1 is compared with the host cluster and observational data of the Coma Cluster.

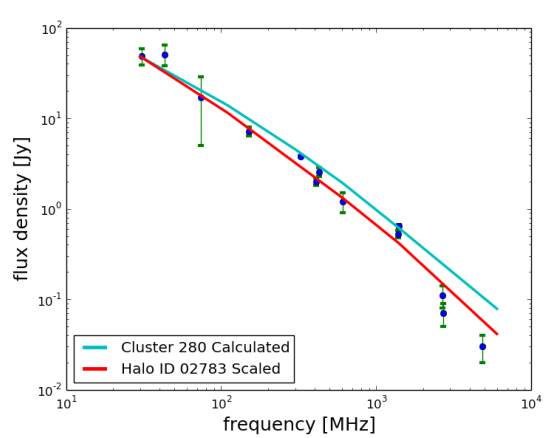


FIGURE 6.4: Slope comparison of the flux density for synchrotron emission of the best DM dominated halo with the host cluster and observational data of the Coma Cluster.

6.2 Statistical Study of High M/L DM Sub-halos

From all the 282 MUSIC clusters I have obtained a total of 466,621 sub-halos of which 132,614 are within $2.5 R_{200\text{crit}}$ ¹ of their host cluster, an approximate distance where resolved particles in the simulation can be obtained. A linear plot of the mass-to-light ratio (M/L) of all these halos plotted against their relative distance to their respective clusters (i.e., ratio of the sub-halo distance by the cluster radius they belong to ($R/R_{200\text{crit}}$)) is shown in Fig. 6.5. It is apparent to see some behavior of grouping of sub-halos showing high M/L ($\sim 360 \pm 70$) as indicated in the shaded region around $R \sim 0.5 \times R_{200\text{crit}}$ of there host clusters. In the following sections I will look deeper to find out whether these high M/L sub-halos are dominantly situated around the outer region of the cluster.

The scatter plot given in Fig. 6.6 shows M/L of the sub-halos plotted against the stars mass with in the sub-halos. I see that sub-halos which have single stars and less gas fraction are seen to be located on the left upper part of the plot. However, to choose the best candidates of “naked” (DM sub-halos with almost no baryonic content) DM sub-halos which are required for a robust study of the multi-wavelength emission from DM annihilation process, I first need to look closer into their particle distribution and identify if there is an enhanced structure in the DM particle distribution. More importantly one need to check on the gas and star content of the sub-halo. Applying all these search criteria I obtain a large number of promising DM sub-halos from which the top four best are analyzed from Section 6.3 to 6.5.

The scatter plot in Figs. 6.7 and 6.8 gives the relative distance of DM sub-halos in the clusters they belong identified based M/L and the star mass with in them. The DM sub-halos which have M/L above 50 and 100 are indicated in red, and the rest in blue, among all DM sub-halos identified with in radial distance of $2.5 R_{200\text{crit}}$ in Fig. 6.7 and

¹ $R_{200\text{crit}}$ is the cluster radius obtained at the over-density of 200 times critical density.

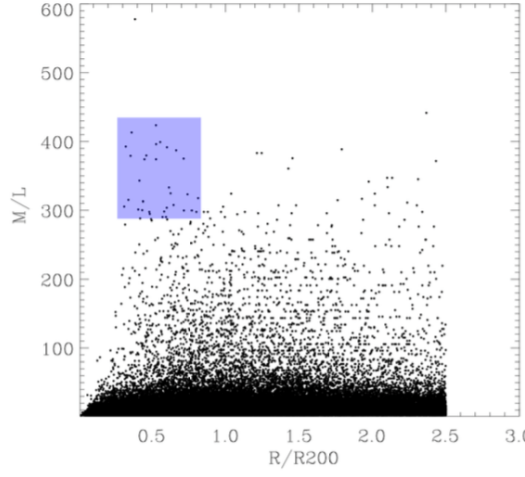


FIGURE 6.5: Scatter plot of DM sub-halos based on M/L and the ratio of their radial distance (R) to radius of their clusters (R_{200} or $R_{200\text{crit}}$).

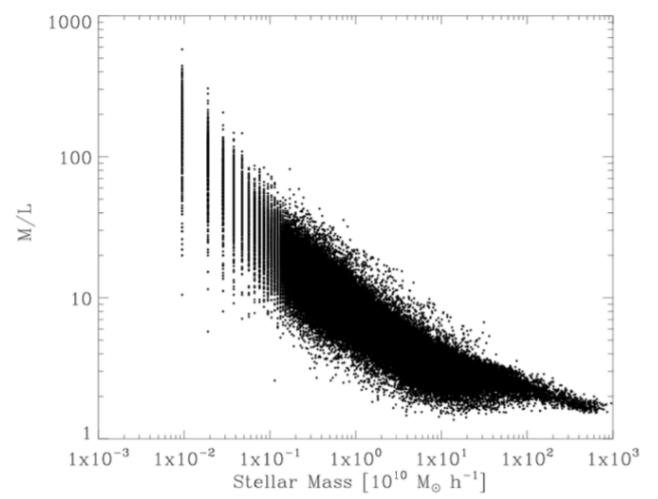


FIGURE 6.6: Scatter plot DM sub-halos based on M/L and star mass.

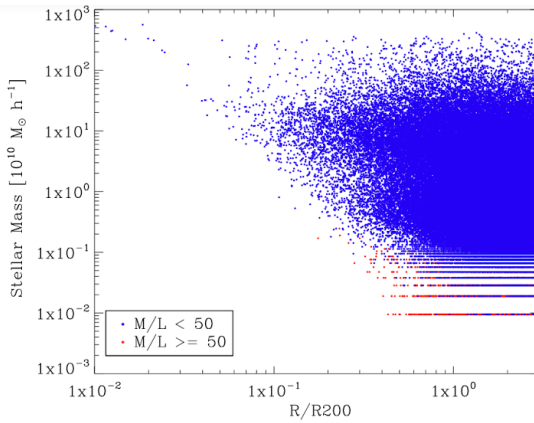


FIGURE 6.7: Scatter plot of DM sub-halos based on the star mass at M/L of 50.

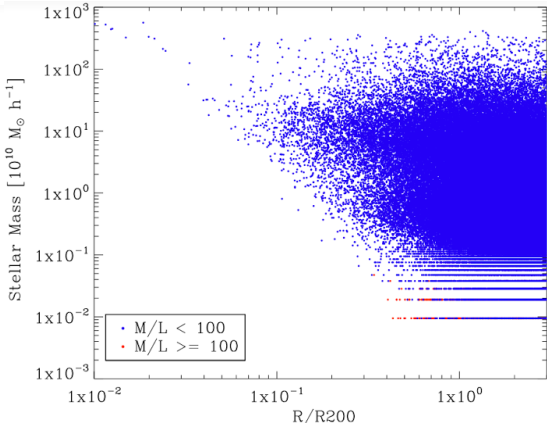


FIGURE 6.8: Scatter plot of DM sub-halos based on the star mass at M/L of 100.

6.8, respectively. The results from both plots can be interpreted simply as the high M/L DM sub-halos are very rare to be found in the inner volume of galaxy clusters.

Furthermore, it is also important to find where there is relatively high chance of finding these high M/L DM sub-halos. Accordingly, in Fig. 6.9 the normalized probability density function ($p(r)$) of finding sub-halos with in r ($R/R_{200\text{crit}}$) is shown for the case where M/L values are above 1, 50 and 100 as indicated in blue, green and red, respectively. The standard error for a count of the DM sub-halos is indicated by the error bar. In plot of M/L above 100 (red line) I observe a sharp decline in the lower values of r which do not overlap with all other halos. And I conclude that the distribution of high M/L DM sub-halos peaks at $r \sim R_{200\text{crit}}$, which may suggest the search for DM annihilation signals from sub-halos in clusters is most promising at $R_{200\text{crit}}$.

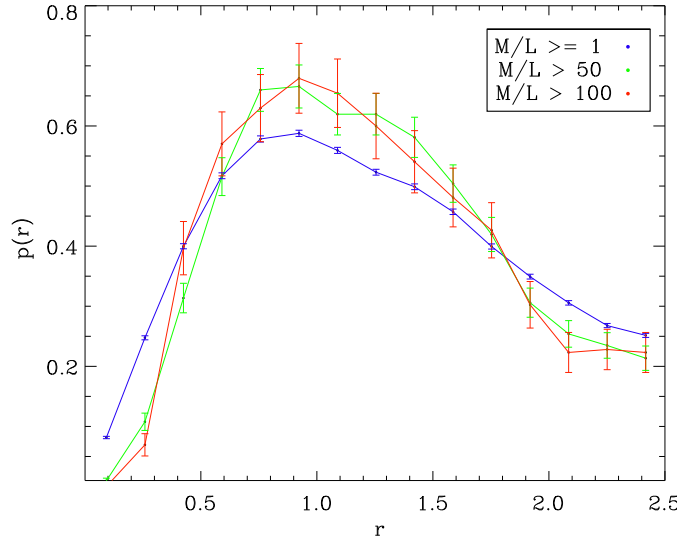


FIGURE 6.9: The probability distribution function of sub-halos based on their M/L at a relative distance r ($R/R_{200\text{crit}}$), the ratio of distances of each sub-halo from the center of the host cluster to the radius of the host cluster at 200 times the critical density of the Universe. Sub-halos with M/L above 1, 50 and 100 are shown in blue, green and red color, respectively.

6.3 Representative Samples of High M/L DM Sub-halos

For the five representative samples of high M/L DM sub-halos, some of whose properties are listed in the table B.1 and B.2 (see Appendix B), I present the DM and gas density square maps (see Appendix C). The maps are produced by calculating the densities using SPH kernel and projecting the density square values in the line-of-sight.

The DM and gas density square projected maps of DM sub-halo 1 are shown in Figs. C.1 and C.2. This halo shows the highest DM density as compared to all the five DM sub-halos. This sub-halo has very small gas content which has a very smooth distribution as indicated by the values in the color bar. The DM density square map of DM sub-halo 2 is shown in Fig. C.3. The structure of this halo is quite different from others. This halo has three structures with the highest DM density in the map which are located in different regions of the map. These structures are also offset to any noticeable dense structure in the gas of Fig. C.4. The DM and gas density square projected maps of DM sub-halo 3 is shown in Fig. C.5 and C.6. While the DM density map shows a prominent peak in the central region of the map which decreases outward, I find almost a smooth distribution in the gas. Figs. C.7 and C.8 show the DM and gas density square maps of the DM sub-halo 4, respectively. The DM map shows a well defined DM structure in the center but with relatively lower values as compared to the other three DM sub-halos. The gas content on the other hand is bigger next to that of DM sub-halo 2.

Features that are observed in these DM sub-halos, i.e., DM enhancement with a distinguishable peak in the center, lower gas content (which also means lower contaminations from signals generated other than by DM) as well as DM structures which are offset to the gas, make these samples quite fit for the study of the properties of DM. The radio

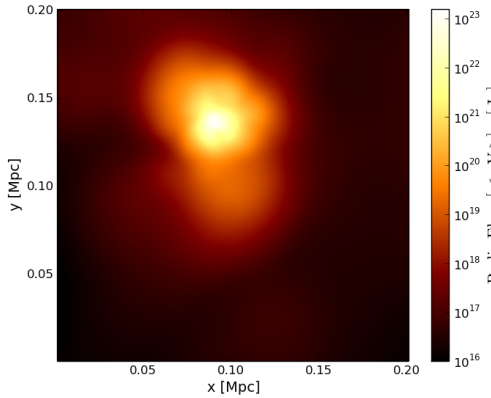


FIGURE 6.10: Synchrotron emission map of DM sub-halo 1 at 110 MHz.

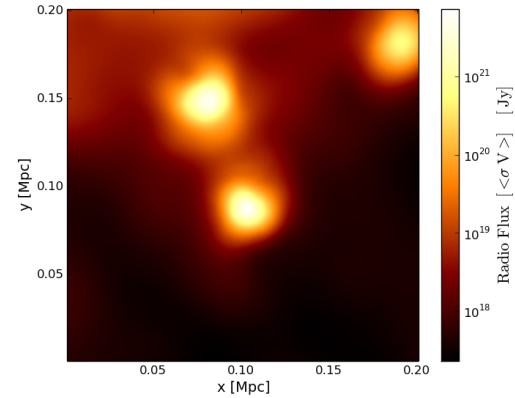


FIGURE 6.11: Synchrotron emission map of DM sub-halo 2 at 110 MHz.

and γ -ray emission results obtained for these DM sub-halos will be presented in the proceeding sections.

6.4 High M/L Sub-halos and the Radio Emission from DM Annihilation Processes.

Here I provide and discuss the results which are obtained for the synchrotron/radio emission processes using radio maps and flux densities for the four high M/L DM sub-halos discussed above. These calculations were made for neutralino mass of $M_\chi = 35$ GeV which is chosen based on the result in Chapter 5 and velocity averaged DM annihilation cross-section $\langle \sigma V \rangle = 1.0 \times 10^{-26} \text{ cm}^3 \text{ s}^{-1}$.

In Figs. 6.10 and 6.11 I show the synchrotron emission maps obtained at 110 MHz for DM sub-halo 1 and 2 given in units of $\langle \sigma V \rangle$ [Jy]. The synchrotron emission maps show similar features to their DM maps (Figs. C.1 and C.8) which is expected to arise from DM density square values used in the synchrotron flux formula. It is also apparent to observe that, in the same way to the DM square values in maps, the synchrotron flux values are the highest for DM sub-halo 1. Even though there is relatively large gas content in DM sub-halo 2 compared to the rest of the sample, it is situated offset to the region of high DM concentration.

Figs. 6.12 and 6.13 give the synchrotron emission maps of DM sub-halo 3 and 4 at 110 MHz, respectively. As the values in color map show these DM sub-halos have relatively lower radio flux DM sub-halo 4 being the lowest of all. These two DM sub-halos show similar appearance in their DM density distributions, i.e., they both show DM density enhancement as well as a centrally peaked radio flux value which decreases outward.

The flux densities are obtained by summing up the flux from all points which contain a contribution along the line of site that is plotted in the emission maps. Here, results obtained for the flux densities of the five DM sub-halos whose radio emission maps were shown in Figs. 6.10 to 6.13 and discussed above will be given. In the following I will also compare the flux densities and shapes of the spectrum of the five DM sub-halos and with the observational data of the Coma Cluster (Thierbach et al., 2003). In Fig.

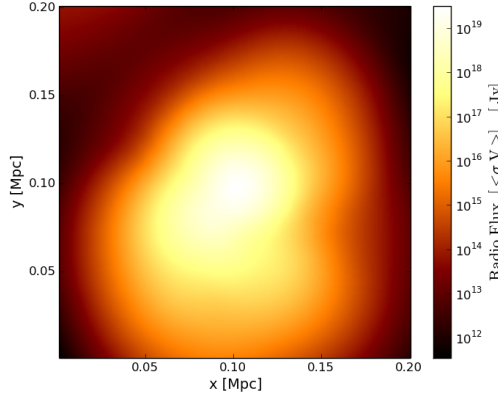


FIGURE 6.12: Synchrotron emission map of DM sub-halo 3 at 110 MHz.

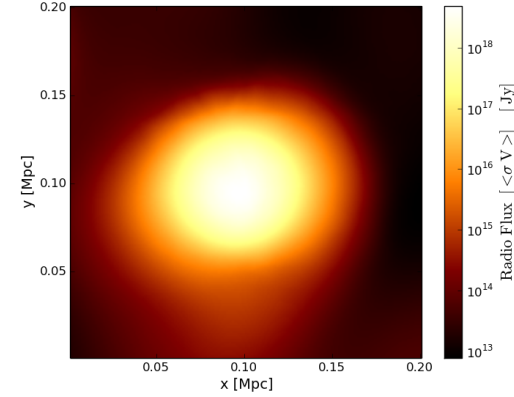


FIGURE 6.13: Synchrotron emission map of DM sub-halo 4 at 110 MHz.

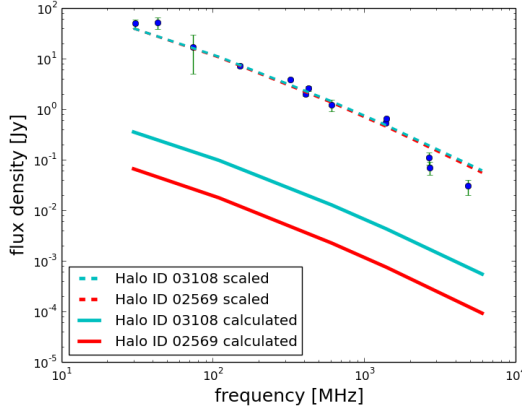


FIGURE 6.14: Comparison of the radio flux density of DM sub-halo 1 and 2 (Halo ID 03108 and 02569) and their spectral features with observational data of the Coma Cluster.

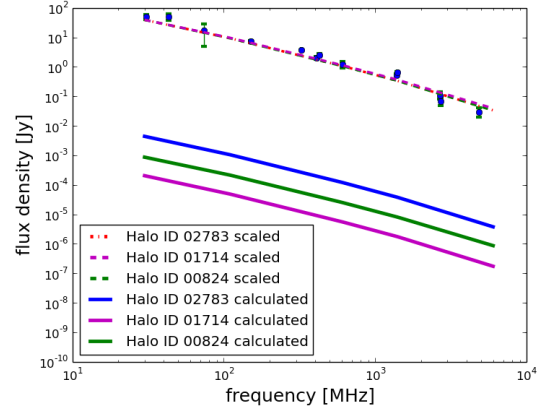


FIGURE 6.15: Comparison of the radio flux density of DM sub-halo 3, 4 and 5 (Halo ID 01714, 00824 and 02783) and their spectral features with observational data of the Coma Cluster.

6.14 I display the flux densities of DM sub-halo 1 and 2 which are given in cyan and red colored lines, respectively. The flux of these DM sub-halos is scaled for comparison as indicated by broken lines which are plotted on the top of the observational data points of the Coma Cluster (blue data points). I observe that their spectra fits very well over most of the data points with a slight deviation at higher frequencies. Fig. 6.15 shows the radio flux densities of DM sub-halo 3, 4 and 5 given in magenta, green and blue lines along with the observational data of the Coma Cluster (blue data points). The flux densities of these three DM sub-halos are lower than that of DM sub-halo 1 and 2 as clearly seen in Fig. 6.16. This is in agreement with the total masses obtained for the five DM sub-halos by the halo finder with in 30 kpc as given in table B.1. One can see that both the total mass and flux density of DM sub-halos 3 and 4 are lower than that of sub-halos 1 and 2.

I show the scaled comparison of spectral feature of the five DM sub-halos with observational data of the Coma Cluster in Fig. 6.17. A closer look shows a deviation between

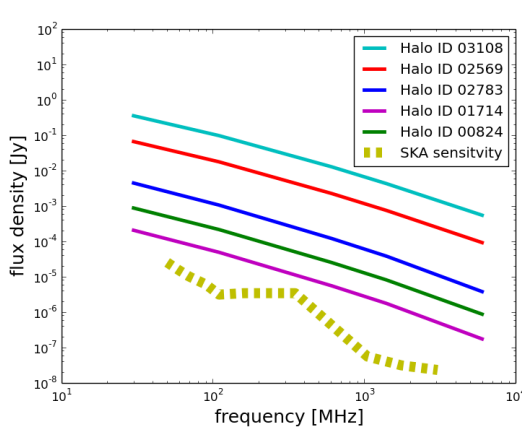


FIGURE 6.16: The radio flux densities of the five high M/L DM sub-halos.

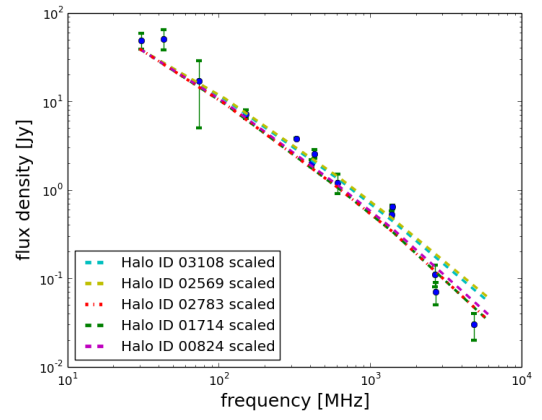


FIGURE 6.17: Scaled comparison of spectral feature of the five DM sub-halos with observational data of the Coma Cluster.

the flux density of all the five sub-halos, more massive ones having a larger deviation from the observational data. Overall the scaled radio flux densities of DM sub-halos show a better fit on the observational data as compared to the radio flux density of clusters as shown in this work for the case of the Coma-like simulated clusters discussed in Chapter 5 shown in Fig. 5.11. Moreover, from Fig. 6.16 I see that the flux densities of all the five DM sub-halos are above the Square Kilometer Array (SKA) sensitivity (broken line in yellow color) obtained with an integration time of 1000 hours which is a reasonable observation time that can be achieved. This result thus suggests observing DM dominated sub-halos using high resolution instruments like SKA to learn about the nature and properties of DM via signals from DM annihilation process. In fact this point can be tested in the future by comparing these spectra with that of objects showing a peak in their DM densities that resemble DM dominated sub-halos among an identified lists of objects.

6.5 High M/L Sub-halos and the Gamma-ray Emission from DM Annihilation Processes.

In the following I discuss some of the results that are obtained for the gamma-ray emission maps and flux densities for the five high M/L DM sub-halos chosen previously, whose properties were listed in table B.1 and B.2. The calculations were performed using neutralino mass of M_χ , 35 GeV and velocity averaged DM annihilation cross-section $\langle \sigma V \rangle = 1.0 \times 10^{-26} \text{ cm}^3 \text{ s}^{-1}$ from Fermi upper limit [Ackermann et al. \(2014\)](#).

We have seen (see Chapter 4) that neutral pions are produced as a result of DM annihilation process and they decay into gamma-rays. This signal is often said to form the cleanest signal. One reason, for example, is the fact that gamma-rays pass undeflected by the magnetic fields in their path from/between their emission (the sources) to observation (the detectors). In Fig. 6.18 to 6.21 I show the gamma-ray emission maps at 100 MeV obtained from pion decay process for DM sub-halo 1 to 4. In all of these maps I see enhanced features (bright regions in the map) looking exactly like the corresponding DM density square maps. In fact this is expected as the gamma-ray flux from pion decay

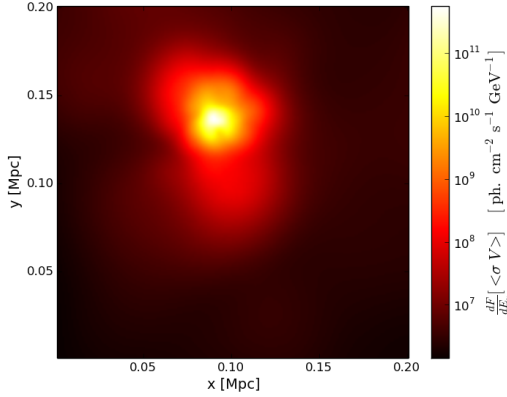


FIGURE 6.18: Gamma-ray emission map from pion decay at 100 MeV for DM sub-halo 1.

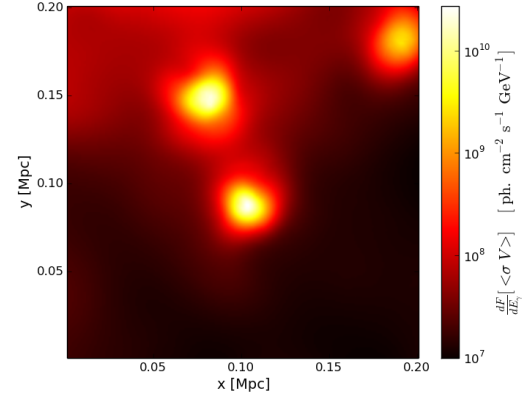


FIGURE 6.19: Gamma-ray emission map from pion decay at 100 MeV for DM sub-halo 2.

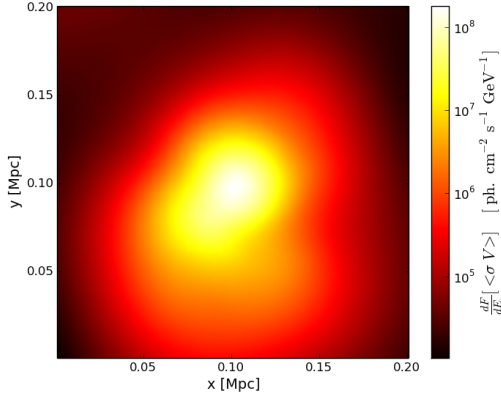


FIGURE 6.20: Gamma-ray emission map from pion decay at 100 MeV for DM sub-halo 3.

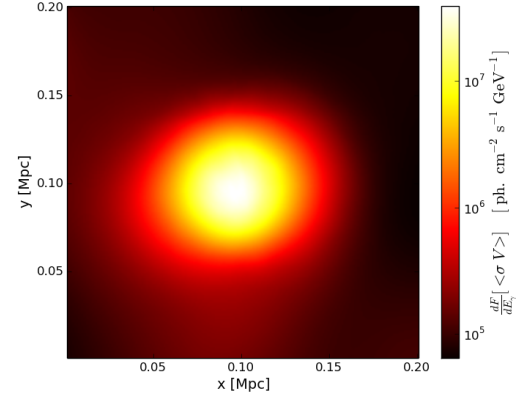


FIGURE 6.21: Gamma-ray emission map from pion decay at 100 MeV for DM sub-halo 4.

is the DM density square integrated over volume in the line-of-sight multiplied by just some constants (see Eqn. 4.13).

Another process that needs to be considered for the gamma-rays is the non-thermal bremsstrahlung radiation obtained from secondary electrons discussed at the end of Chapter 4. The gamma-ray emission maps obtained via this process are given in Fig. D.2 to D.3 (Appendix D). Unlike pion decay these maps show less peculiar features this is believed to arise from lower values of number densities in the thermal protons which is considered to be equal to the thermal electron number densities. In Fig. 6.22 and 6.23 I give the pion decay and non-thermal bremsstrahlung gamma-ray emission for DM sub-halo 5. DM sub-halo 5 has relatively high gas content as compared to the four DM sub-halos, due to this it has shown 6 orders of difference in the flux between the two emission processes. The gamma-ray differential flux from pion decay and non-thermal bremsstrahlung process for the five DM sub-halos is shown in Fig. 6.24. The gamma-ray flux from pion decay process from DM sub-halo 1 (cyan color) is higher than that of DM sub-halo 2 (red color) and vice versa for gamma-ray flux from non-thermal bremsstrahlung process. This is due to the lower values of thermal electron densities

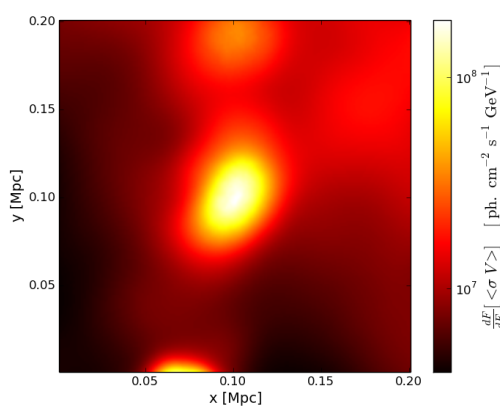


FIGURE 6.22: Gamma-ray emission map from pion decay process at 100 MeV for DM sub-halo 5.

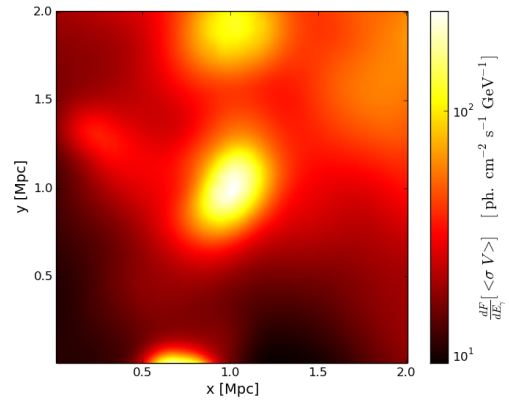


FIGURE 6.23: Gamma-ray emission map from non-thermal bremsstrahlung process at 100 MeV for DM sub-halo 5.

which is used in the formula of the gamma-ray flux from non-thermal bremsstrahlung process (see Eqn. 4.4). The pion decay spectrum shown by the solid lines in Fig. 6.24 stays above the non-thermal bremsstrahlung gamma-ray flux values shown in broken lines for almost all energies between the mass of electron, m_e , 5.11×10^{-4} MeV and the mass of neutralino M_χ , 35 GeV for all the five DM sub-halos. The gamma-ray flux densities of high M/L DM sub-halos show relatively lower values of gamma-ray flux from non-thermal bremsstrahlung process especially for those DM sub-halos in the sample which have very low gas content. Overall, the total gamma-ray flux spectrum from all DM sub-halo looks very similar to the gamma-ray spectrum from pion decay process.

6.6 Summary

Making use of different halo properties obtained by Rockstar halo finder (Behroozi et al., 2013) I studied a large number of sub-halos obtained from the 282 MUSIC clusters (Sembolini et al., 2013). I have selected sub-halos which show: (i) high values of M/L, (ii) enhanced structure in the DM particle distribution, (iii) very small or almost no baryonic content (“naked” DM sub-halos), and (iv) DM and baryons offset each other. These sub-halos are expected to be good candidates for studying the nature of DM via indirect detections of signals from secondary electrons and gamma-ray radiation from neutral pion decay process. From the statistical studies of all the sub-halos I have found that the radial distribution of the high M/L DM sub-halos is more strongly peaked at $\sim R_{200\text{crit}}$. This may suggest that the search for DM annihilation signals from sub-halos in clusters is most promising at $R_{200\text{crit}}$.

For the study of the radio and γ -ray emission from DM annihilation process, I choose a representative sample of five high M/L DM Sub-halos. And I determine the radio flux using neutralino masses of 35 GeV, magnetic field Model A and $\langle \sigma V \rangle = 1.0 \times 10^{-26}$ $\text{cm}^3 \text{s}^{-1}$. I observe that their scaled spectra fits very well over most of the observational data of the Coma Cluster as compared to the radio flux density of their host clusters. This is also in agreement with a relative deviation I find between the flux densities of

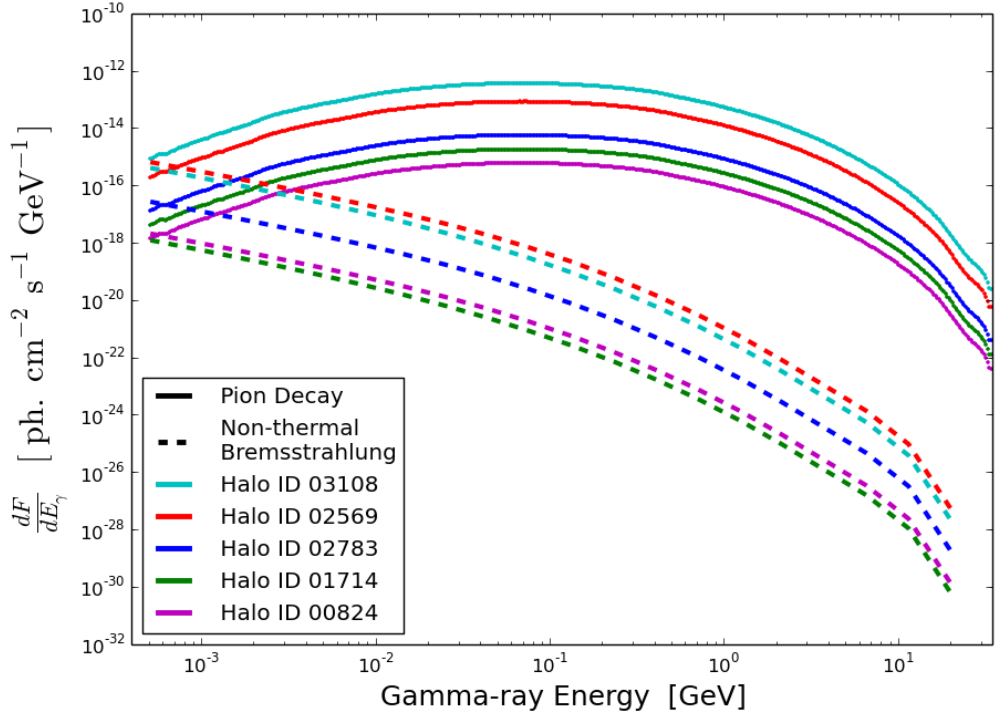


FIGURE 6.24: Differential gamma-ray flux densities of the five high M/L DM sub-halos from pion decay and non-thermal bremsstrahlung processes.

the five sub-halos where by more massive ones showed relatively higher deviation from the observational data. The radio flux densities for the five high M/L DM sub-halos are all above the sensitivity limit of the Square Kilometer Array (SKA) with an integration time of 1000 hours.

Taking the same neutralino parameters as in radio, I have calculated the γ -ray flux densities of the five high M/L sub-halos. Their γ -ray flux densities show relatively lower values of γ -ray flux from non-thermal bremsstrahlung process especially for those DM sub-halos in the sample which have very low gas content. In some cases their non-thermal bremsstrahlung spectrum stays below the pion decay spectrum at almost all energies. Consequently, the overall γ -ray flux spectrum from high M/L sub-halos is dominated by γ -ray emission from pion decay process. In the next chapter I will provide the concluding remarks for my studies of “multi-wavelength emissions from DM annihilation processes in galaxy clusters and high M/L DM sub-halos using cosmological simulations”.

Chapter 7

Concluding Remarks

Most of the matter in the Universe is in the form of non-luminous DM. The particle nature of DM is still unknown. DM self-annihilation would provide a mechanism for an indirect detection via electromagnetic emissions from secondary electrons production. The spectral features of the emission are expected to be closely related to the nature, composition and mass of the DM particles (Colafrancesco et al., 2006). I determine the radio and gamma-ray emissions from neutralino DM annihilation processes considering two neutralino masses, $M_\chi = 35$ GeV and 60 GeV along with two different models of magnetic fields.

Using the Marenostrum-MultiDark Simulation of galaxy Clusters (MUSIC) (Sembolini et al., 2013), I develop semi-analytical models which provide multi-wavelength emission maps from DM annihilation processes in galaxy clusters and sub-halos. The high resolution and number of MUSIC clusters allows us to single out DM sub-halos where it can be expected that the DM annihilation signal exceeds ordinary emission. Applying a Smooth Particle Hydrodynamics (SPH) kernel allows us to determine the DM density at arbitrary locations within the cluster volume which is used to focus on the contribution of sub-halos to the multi-wavelength emission maps of clusters.

The DM radio flux densities for a neutralino mass of 35 GeV and the magnetic field based on Model A match best the observed diffuse radio emission of the Coma Cluster (Thierbach et al., 2003). The fact that the flux density shows a very good agreement with the observed one without invoking a boost factor from DM sub-structures shows that the distribution of sub-structures is described well in the simulations. Our model also predicts gamma-ray emission from pion decay, non-thermal bremsstrahlung and IC scattering processes. The contribution to the overall gamma-ray flux from IC dominates at low energies. Non-thermal bremsstrahlung is most prominent at intermediate energies. At energies above ~ 35 MeV pion decay dominates.

In order to investigate the annihilation signal from “naked” sub-halos I select sub-halos with exceptionally high mass-to-light (M/L) ratios from all the 282 MUSIC clusters. These sub-halos are expected to be good candidates for studying the nature of DM via indirect detections of signals from secondary electrons and gamma-ray radiation from neutral pion decay process. The radial distribution of high M/L DM sub-halos is more strongly peaked at $\sim R_{200\text{crit}}$ compared to the overall distribution of sub-halos.

I demonstrate that the radio flux densities for the five selected high M/L sub-halos are above the sensitivity limit of the Square Kilometer Array (SKA) with an integration time of 1000 hours. The gamma-ray flux densities of high M/L sub-halos show relatively low gamma-ray flux from non-thermal bremsstrahlung. In some cases their non-thermal bremsstrahlung spectrum stays below the pion decay spectrum at almost all energies. Consequently, the overall gamma-ray flux spectrum from high M/L sub-halos is dominated by the pion decay process.

In the current work I have considered the energy loss of secondary electrons as they interact with the ICM. However, I have not taken into account the diffusion of secondary electrons which would be required for a more realistic study of DM annihilation signal from sub-halos. Also, small amounts of baryons in the high M/L sub-halos may contaminate the annihilation signal which needs to be determined quantitatively. Finally, comparison of these results with observations in the gamma-ray band is required to confirm the DM annihilation signal predictions. Very recently, a gamma-ray detection from a DM sub-halo has been reported by [Wang et al. \(2016\)](#). The γ -ray spectrum they present is consistent with DM annihilation into final state $b\bar{b}$ which is also used in the DM models of this work. This opens the opportunity for a future comparison with these DM models predictions.

Appendix A

Emission Maps for DM model 35 GeV

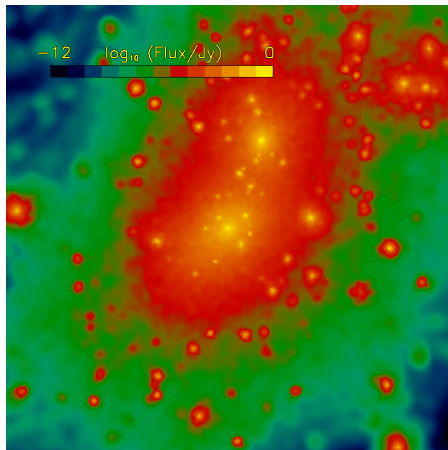


FIGURE A.1: Radio emission map at 110 MHz using magnetic field of Model A for DM model 35 GeV.

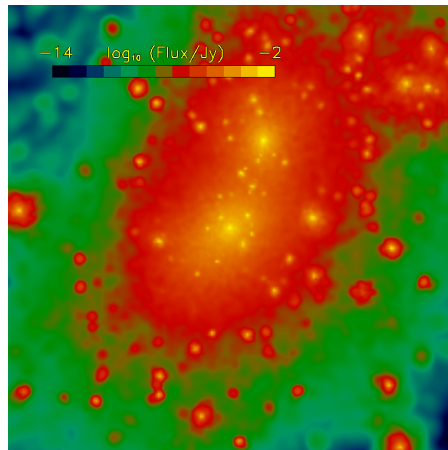


FIGURE A.2: Radio emission map at 1400 MHz using magnetic field of Model A for DM model 35 GeV.

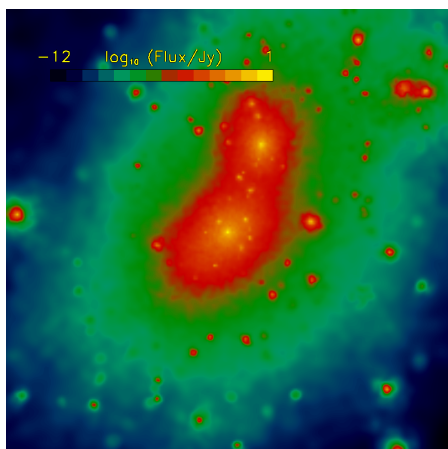


FIGURE A.3: Radio emission map at 110 MHz using magnetic field of Model B for DM model 35 GeV.

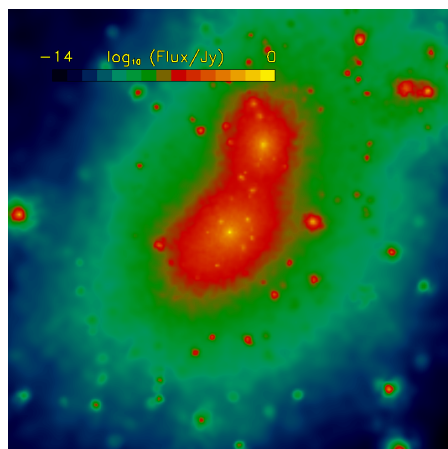


FIGURE A.4: Radio emission map at 1400 MHz using magnetic field of Model B for DM model 35 GeV.

Appendix B

Properties of Representative Samples of High M/L DM Sub-halos

Halo ID	M/L	Maximum density of DM [$M_{\odot} \text{ kpc}^{-3}$]	Total mass of the halo in 30 kpc radius [M_{\odot}]
1	324	2.8×10^7	3.07×10^{10}
2	317	5.8×10^6	3.01×10^{10}
3	334	3.2×10^5	3.16×10^{10}
4	307	1.3×10^6	2.91×10^{10}
5	30.5	3.4×10^5	3.18×10^{10}

TABLE B.1: Halo ID, maximum DM density summed along the line of sight and total mass with in 30 kpc radius for the five high M/L DM sub-halos considered in our study.

Halo ID	gas fraction	star fraction	DM fraction	radial distance [Mpc]
1	0.00000000	0.00308502	0.99691500	1.4273890
2	0.00944456	0.00314819	0.98740700	1.2760991
3	0.00000000	0.00299714	0.99700300	3.6156359
4	0.00651171	0.00325586	0.99023200	1.9817620
5	0.00594977	0.03272370	0.96132700	0.9785210

TABLE B.2: Halo ID, fraction of gas, star and DM in the halo with in 30 kpc radius, and radial distance from the center of the cluster for the five high M/L DM sub-halos considered in our study.

Appendix C

DM and Gas Density Square Maps of High M/L DM Sub-halos

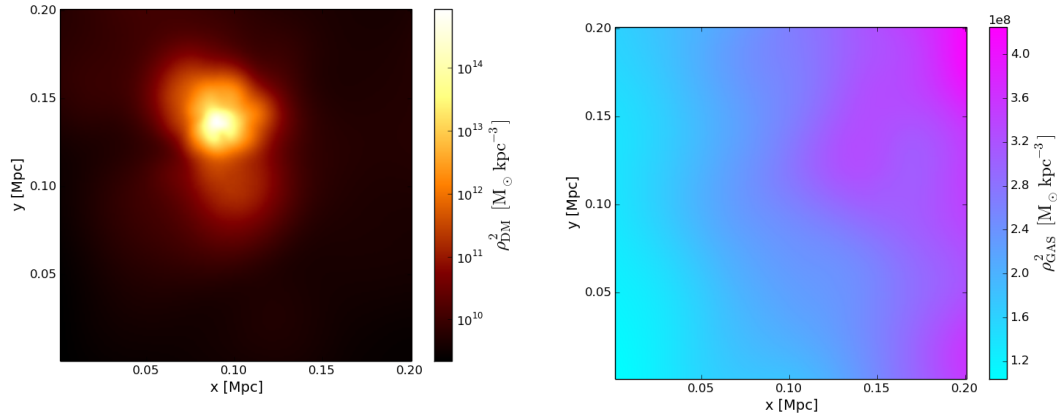


FIGURE C.1: DM density square of DM sub-halo 1 integrated along the line-of-sight.

FIGURE C.2: Gas density square of DM sub-halo 1 integrated along the line-of-sight.

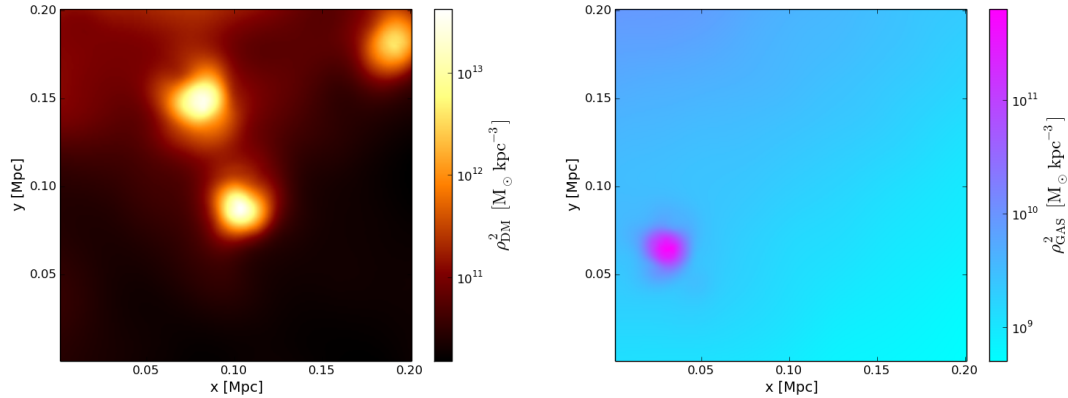


FIGURE C.3: DM density square of DM sub-halo 2 integrated along the line-of-sight.

FIGURE C.4: Gas density square of DM sub-halo 2 integrated along the line-of-sight.

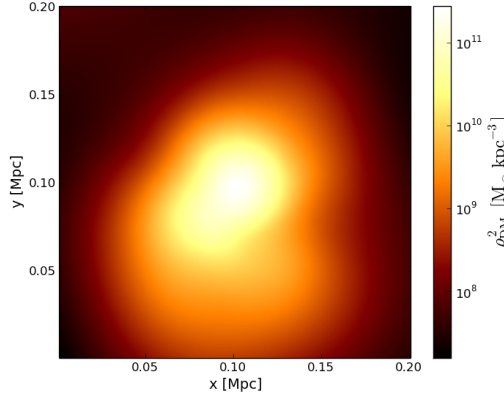


FIGURE C.5: DM density square of DM sub-halo 3 integrated along the line-of-sight.

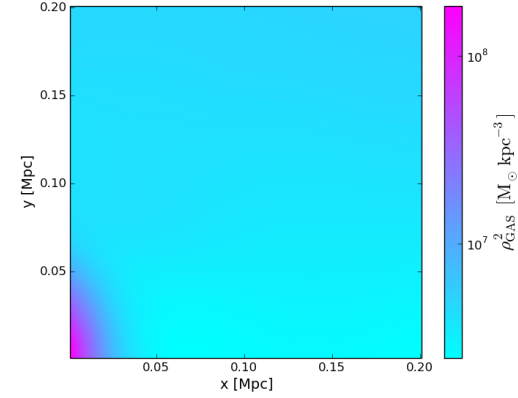


FIGURE C.6: Gas density square of DM sub-halo 3 integrated along the line-of-sight.

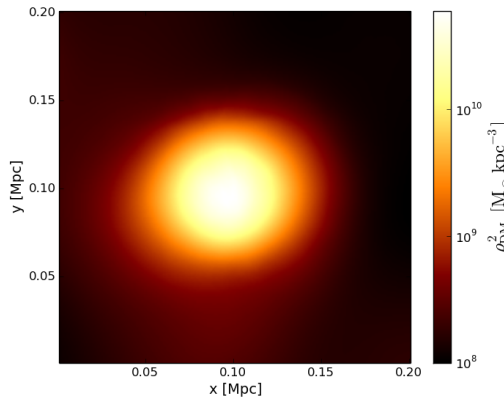


FIGURE C.7: DM density square of DM sub-halo 4 integrated along the line-of-sight.

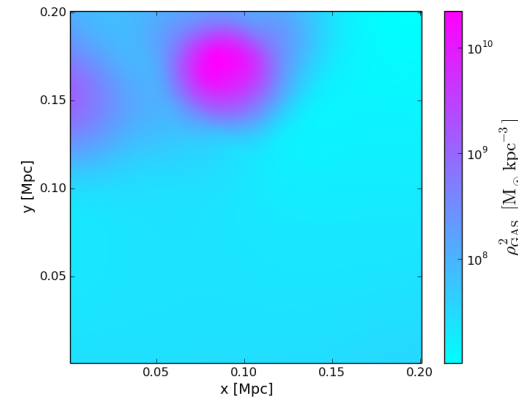


FIGURE C.8: Gas density square of DM sub-halo 4 integrated along the line-of-sight.

Appendix D

Gamma-ray Emission Maps from Non-thermal Bremsstrahlung Process

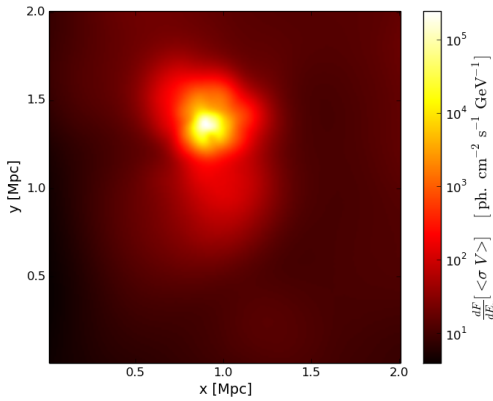


FIGURE D.1: Gamma-ray emission map from non-thermal bremsstrahlung process at 100 MeV for DM sub-halo 1.

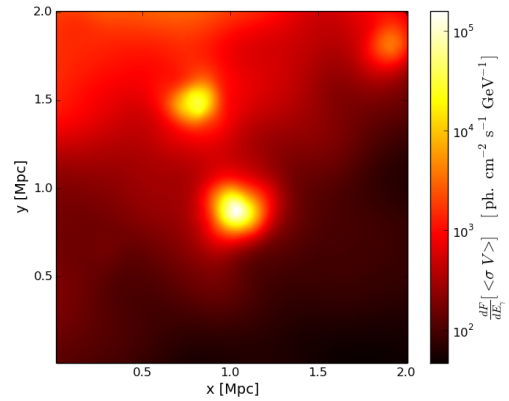


FIGURE D.2: Gamma-ray emission map from non-thermal bremsstrahlung process at 100 MeV for DM sub-halo 2.

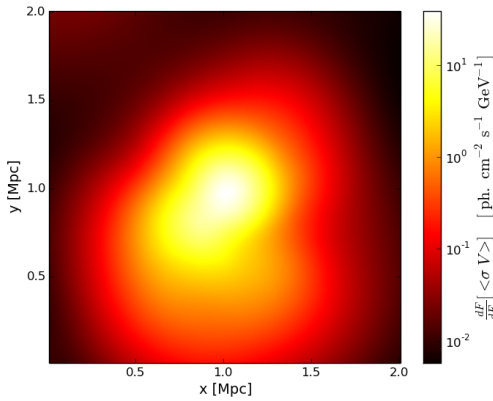


FIGURE D.3: Gamma-ray emission map from non-thermal bremsstrahlung process at 100 MeV for DM sub-halo 3.

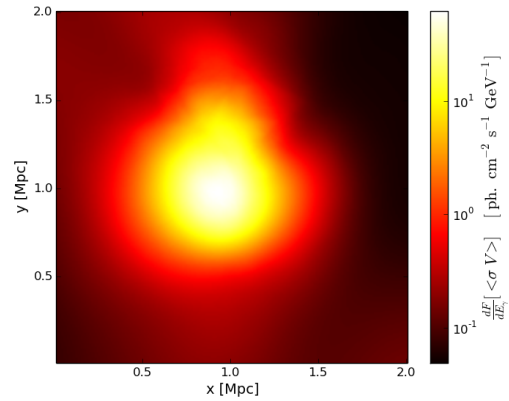


FIGURE D.4: Gamma-ray emission map from non-thermal bremsstrahlung process at 100 MeV for DM sub-halo 4.

Bibliography

- W. L. Freedman, B. F. Madore, B. K. Gibson, L. Ferrarese, D. D. Kelson, S. Sakai, J. R. Mould, R. C. Kennicutt, Jr., H. C. Ford, J. A. Graham, J. P. Huchra, S. M. G. Hughes, G. D. Illingworth, L. M. Macri, and P. B. Stetson. Final Results from the Hubble Space Telescope Key Project to Measure the Hubble Constant. *ApJ*, 553: 47–72, May 2001. doi: 10.1086/320638.
- D. J. Fixsen, E. S. Cheng, J. M. Gales, J. C. Mather, R. A. Shafer, and E. L. Wright. The Cosmic Microwave Background Spectrum from the Full COBE FIRAS Data Set. *ApJ*, 473:576, December 1996. doi: 10.1086/178173.
- S. Burles and D. Tytler. The Deuterium Abundance toward Q1937-1009. *ApJ*, 499: 699–712, May 1998a.
- S. Burles and D. Tytler. The Deuterium Abundance toward QSO 1009+2956. *ApJ*, 507: 732–744, November 1998b. doi: 10.1086/306341.
- M. S. Turner and J. A. Tyson. Cosmology at the millennium. *Reviews of Modern Physics Supplement*, 71:S145–S164, March 1999. doi: 10.1103/RevModPhys.71.S145.
- A. G. Riess, A. V. Filippenko, P. Challis, A. Clocchiatti, A. Diercks, P. M. Garnavich, R. L. Gilliland, C. J. Hogan, S. Jha, R. P. Kirshner, B. Leibundgut, M. M. Phillips, D. Reiss, B. P. Schmidt, R. A. Schommer, R. C. Smith, J. Spyromilio, C. Stubbs, N. B. Suntzeff, and J. Tonry. Observational Evidence from Supernovae for an Accelerating Universe and a Cosmological Constant. *AJ*, 116:1009–1038, September 1998. doi: 10.1086/300499.
- Saul Perlmutter, G Aldering, G Goldhaber, RA Knop, P Nugent, PG Castro, S Deustua, S Fabbro, A Goobar, DE Groom, et al. Measurements of ω and λ from 42 high-redshift supernovae. *The Astrophysical Journal*, 517(2):565, 1999.
- D. P. Roy. Basic Constituents of the Visible and Invisible Matter - A Microscopic View of the Universe. *ArXiv Physics e-prints*, July 2000.
- M. Watanabe, K. Yamashita, A. Furuzawa, H. Kunieda, Y. Tawara, and H. Honda. Temperature Map of the Coma Cluster of Galaxies. *ApJ*, 527:80–85, December 1999. doi: 10.1086/308084.
- V. Luković, P. Cabella, and N. Vittorio. Dark matter in cosmology. *International Journal of Modern Physics A*, 29:1443001, July 2014. doi: 10.1142/S0217751X14430015.
- J. L. Feng. Dark Matter Candidates from Particle Physics and Methods of Detection. *ARA&A*, 48:495–545, September 2010. doi: 10.1146/annurev-astro-082708-101659.

- T. Marrodán Undagoitia and L. Rauch. Dark matter direct-detection experiments. *Journal of Physics G Nuclear Physics*, 43(1):013001, January 2016. doi: 10.1088/0954-3899/43/1/013001.
- E. A. Baltz, M. Battaglia, M. E. Peskin, and T. Wizansky. Determination of dark matter properties at high-energy colliders. *Phys. Rev. D*, 74(10):103521, November 2006. doi: 10.1103/PhysRevD.74.103521.
- J. L. Feng. ILC Cosmology. *ArXiv High Energy Physics - Phenomenology e-prints*, September 2005.
- G. Beck and S. Colafrancesco. A Multi-frequency analysis of dark matter annihilation interpretations of recent anti-particle and γ -ray excesses in cosmic structures. *J. Cosmology Astropart. Phys.*, 5:013, May 2016. doi: 10.1088/1475-7516/2016/05/013.
- J. M. Gaskins. A review of indirect searches for particle dark matter. *Contemporary Physics*, 57:496–525, October 2016. doi: 10.1080/00107514.2016.1175160.
- S. Brown and L. Rudnick. Diffuse radio emission in/around the Coma cluster: beyond simple accretion. *MNRAS*, 412:2–12, March 2011. doi: 10.1111/j.1365-2966.2010.17738.x.
- C. L. Sarazin. The Energy Spectrum of Primary Cosmic-Ray Electrons in Clusters of Galaxies and Inverse Compton Emission. *ApJ*, 520:529–547, August 1999. doi: 10.1086/307501.
- M. Thierbach, U. Klein, and R. Wielebinski. The diffuse radio emission from the Coma cluster at 2.675 GHz and 4.85 GHz. *A&A*, 397:53–61, January 2003. doi: 10.1051/0004-6361:20021474.
- S. Colafrancesco, R. Lieu, P. Marchegiani, M. Pato, L. Pieri, and R. Buonanno. Dark matter interpretation of the origin of non-thermal phenomena in galaxy clusters. *A&A*, 527:A80, March 2011a. doi: 10.1051/0004-6361/201014738.
- S. Colafrancesco, S. Profumo, and P. Ullio. Multi-frequency analysis of neutralino dark matter annihilations in the Coma cluster. *A&A*, 455:21–43, August 2006. doi: 10.1051/0004-6361:20053887.
- F. Sembolini, G. Yépes, M. De Petris, S. Gottlöber, L. Lamagna, and B. Comis. The MUSIC of galaxy clusters - I. Baryon properties and scaling relations of the thermal Sunyaev-Zel'dovich effect. *MNRAS*, 429:323–343, February 2013. doi: 10.1093/mnras/sts339.
- S. Weinberg. *Gravitation and Cosmology: Principles and Applications of the General Theory of Relativity*. July 1972.
- A. Einstein. Zur allgemeinen Relativitätstheorie. *Sitzungsberichte der Königlich Preußischen Akademie der Wissenschaften (Berlin)*, Seite 778-786., 1915.
- M. Bartelmann. TOPICAL REVIEW Gravitational lensing. *Classical and Quantum Gravity*, 27(23):233001, December 2010. doi: 10.1088/0264-9381/27/23/233001.
- A. Friedmann. Über die Krümmung des Raumes. *Zeitschrift fur Physik*, 10:377–386, 1922. doi: 10.1007/BF01332580.
- P. J. E. Peebles. Principle of Physical Cosmology. 1993.

- A. A. Penzias and R. W. Wilson. A measurement of excess antenna temperature at 4080 MHz. *ApJ*, 142:419–421, 1965.
- J. C. Mather, E. S. Cheng, R. E. Eplee, Jr., R. B. Isaacman, S. S. Meyer, and et al. 354: L37, 1990.
- S. Sarkar. *Reports on Progress in Physics*, 59:1493, 1996.
- B. Ryden. *Introduction to cosmology*. 2003.
- J. A. Peacock. Inflationary cosmology and structure formation. *ArXiv Astrophysics e-prints*, January 1996.
- A. H. Guth. Inflationary universe: A possible solution to the horizon and flatness problems. *Phys. Rev. D*, 23:347–356, January 1981. doi: 10.1103/PhysRevD.23.347.
- A. R. Liddle. An Introduction to Cosmological Inflation. In A. Masiero, G. Senjanovic, and A. Smirnov, editors, *High Energy Physics and Cosmology, 1998 Summer School*, page 260, 1999.
- Planck Collaboration, P. A. R. Ade, N. Aghanim, M. Arnaud, M. Ashdown, J. Aumont, C. Baccigalupi, A. J. Banday, R. B. Barreiro, and R. Barrena. Planck 2015 results. XXVII. The Second Planck Catalogue of Sunyaev-Zeldovich Sources. *ArXiv e-prints*, February 2015.
- F. Zwicky. Die Rotverschiebung von extragalaktischen Nebeln. *Helvetica Physica Acta*, 6:110–127, 1933.
- M. Colless and A. M. Dunn. Structure and Dynamics of the Coma Cluster. *ApJ*, 458: 435, February 1996. doi: 10.1086/176827.
- T. Padmanabhan. Modelling the non-linear gravitational clustering in the expanding Universe. *MNRAS*, 278:L29–L33, January 1996. doi: 10.1093/mnras/278.2.L29.
- J. H. Oort. The force exerted by the stellar system in the direction perpendicular to the galactic plane and some related problems. *Bull. Astron. Inst. Netherlands*, 6:249, August 1932.
- F. D. Kahn and L. Woltjer. Intergalactic Matter and the Galaxy. *ApJ*, 130:705, November 1959. doi: 10.1086/146762.
- C. Muñoz. Dark Matter Detection in the Light of Recent Experimental Results. *International Journal of Modern Physics A*, 19:3093–3169, 2004. doi: 10.1142/S0217751X04018154.
- J. F. Navarro, C. S. Frenk, and S. D. M. White. The Structure of Cold Dark Matter Halos. *ApJ*, 462:563, May 1996. doi: 10.1086/177173.
- J. O. Bennett, M. Donahue, N. Schneider, and M. Voit. *The Cosmic Perspective, 6th Edition*. 2010.
- S. Colafrancesco. Dark Matter in Modern Cosmology. In S. K. Chakrabarti, A. I. Zhuk, and G. S. Bisnovatyi-Kogan, editors, *American Institute of Physics Conference Series*, volume 1206 of *American Institute of Physics Conference Series*, pages 5–26, January 2010. doi: 10.1063/1.3292511.

- J. P. Ostriker and P. Steinhardt. New Light on Dark Matter. *Science*, 300:1909–1914, June 2003. doi: 10.1126/science.1085976.
- B. Sadoulet. Deciphering the nature of dark matter. *Reviews of Modern Physics Supplement*, 71:S197–S204, March 1999. doi: 10.1103/RevModPhys.71.S197.
- C. Afonso et al. Limits on galactic dark matter with 5 years of eros smc data. *Astron. Astrophys.*, 400:951–956, 2003.
- L. Bergström. Dark matter candidates. *New Journal of Physics*, 11(10):105006, October 2009. doi: 10.1088/1367-2630/11/10/105006.
- C. Weinheimer. The neutrino mass direct measurements. *ArXiv High Energy Physics - Experiment e-prints*, June 2003.
- E. Aliu, S. Andringa, S. Aoki, J. Argyriades, K. Asakura, R. Ashie, H. Berns, H. Bhang, A. Blondel, S. Borghi, et al. Evidence for Muon Neutrino Oscillation in an Accelerator-Based Experiment. *Physical Review Letters*, 94(8):081802, March 2005. doi: 10.1103/PhysRevLett.94.081802.
- G. Bertone, D. Hooper, and J. Silk. Particle dark matter: evidence, candidates and constraints. *Phys. Rep.*, 405:279–390, January 2005. doi: 10.1016/j.physrep.2004.08.031.
- E. Komatsu, J. Dunkley, M. R. Nolta, C. L. Bennett, B. Gold, G. Hinshaw, N. Jarosik, D. Larson, M. Limon, L. Page, D. N. Spergel, M. Halpern, R. S. Hill, A. Kogut, S. S. Meyer, G. S. Tucker, J. L. Weiland, E. Wollack, and E. L. Wright. Five-Year Wilkinson Microwave Anisotropy Probe Observations: Cosmological Interpretation. *ApJS*, 180:330–376, February 2009. doi: 10.1088/0067-0049/180/2/330.
- Simon DM White, CS Frenk, and Marc Davis. Clustering in a neutrino-dominated universe. *The Astrophysical Journal*, 274:L1–L5, 1983.
- R. D. Peccei and H. R. Quinn. CP conservation in the presence of pseudoparticles. *Physical Review Letters*, 38:1440–1443, June 1977. doi: 10.1103/PhysRevLett.38.1440.
- G. G. Raffelt. Astrophysical Axion Bounds. In M. Kuster, G. Raffelt, and B. Beltrán, editors, *Axions*, volume 741 of *Lecture Notes in Physics*, Berlin Springer Verlag, page 51, 2008.
- L. Bergström. Non-baryonic dark matter: observational evidence and detection methods. *Reports on Progress in Physics*, 63:793–841, May 2000. doi: 10.1088/0034-4885/63/5/2r3.
- G. Jungman, M. Kamionkowski, and K. Griest. Supersymmetric dark matter. *Phys. Rep.*, 267:195–373, March 1996. doi: 10.1016/0370-1573(95)00058-5.
- M. Lisanti. Lectures on Dark Matter Physics. In J. Polchinski and et al., editors, *New Frontiers in Fields and Strings (TASI 2015) - Proceedings of the 2015 Theoretical Advanced Study Institute in Elementary Particle Physics. Edited by POLCHINSKI JOSEPH ET AL. Published by World Scientific Publishing Co. Pte. Ltd., 2017. ISBN #9789813149441*, pp. 399-446, pages 399–446, 2017. doi: 10.1142/9789813149441_0007.

- Planck Collaboration, P. A. R. Ade, N. Aghanim, M. Arnaud, M. Ashdown, J. Aumont, C. Baccigalupi, A. J. Banday, R. B. Barreiro, J. G. Bartlett, and et al. Planck 2015 results. XIII. Cosmological parameters. *A&A*, 594:A13, September 2016a. doi: 10.1051/0004-6361/201525830.
- M. Cirelli. Status of Indirect (and Direct) Dark Matter searches. *ArXiv e-prints*, November 2015.
- B. C. Allanach, G. Belanger, F. Boudjema, and A. Pukhov. Requirements on collider data to match the precision of WMAP on supersymmetric dark matter. *Journal of High Energy Physics*, 12:020, December 2004. doi: 10.1088/1126-6708/2004/12/020.
- T. Moroi, Y. Shimizu, and A. Yotsuyanagi. Reconstructing dark matter density with e^+e^- linear collider in focus-point supersymmetry [rapid communication]. *Physics Letters B*, 625:79–87, October 2005. doi: 10.1016/j.physletb.2005.07.068.
- A. Birkedal, K. Matchev, J. Alexander, K. Ecklund, L. Fields, R. C. Gray, D. Hertz, C. D. Jones, and J. Pivarski. Testing Cosmology at the ILC. *ArXiv High Energy Physics - Phenomenology e-prints*, July 2005.
- J. D. Lewin and P. F. Smith. Review of mathematics, numerical factors, and corrections for dark matter experiments based on elastic nuclear recoil. *Astroparticle Physics*, 6: 87–112, December 1996. doi: 10.1016/S0927-6505(96)00047-3.
- R. Bernabei, P. Belli, F. Cappella, R. Cerulli, C. J. Dai, A. D’Angelo, H. L. He, A. Incicchitti, H. H. Kuang, J. M. Ma, F. Montecchia, F. Nozzoli, D. Prosperi, X. D. Sheng, and Z. P. Ye. First results from DAMA/LIBRA and the combined results with DAMA/NaI. *European Physical Journal C*, 56:333, August 2008. doi: 10.1140/epjc/s10052-008-0662-y.
- G. Bertone and D. Hooper. A History of Dark Matter. *ArXiv e-prints*, May 2016.
- M. Klasen, M. Pohl, and G. Sigl. Indirect and direct search for dark matter. *Progress in Particle and Nuclear Physics*, 85:1–32, November 2015. doi: 10.1016/j.ppnp.2015.07.001.
- A. Abramowski, F. Aharonian, F. Ait Benkhali, A. G. Akhperjanian, E. Angüner, M. Backes, S. Balenderan, A. Balzer, A. Barnacka, Y. Becherini, and et al. Search for dark matter annihilation signatures in H.E.S.S. observations of dwarf spheroidal galaxies. *Phys. Rev. D*, 90(11):112012, December 2014. doi: 10.1103/PhysRevD.90.112012.
- S. Colafrancesco, P. Marchegiani, and G. Beck. Evolution of dark matter halos and their radio emissions. *J. Cosmology Astropart. Phys.*, 2:032, February 2015. doi: 10.1088/1475-7516/2015/02/032.
- Planck Collaboration, P. A. R. Ade, N. Aghanim, M. Arnaud, M. Ashdown, J. Aumont, C. Baccigalupi, A. J. Banday, R. B. Barreiro, J. G. Bartlett, and et al. Planck 2015 results. XIII. Cosmological parameters. *A&A*, 594:A13, September 2016b. doi: 10.1051/0004-6361/201525830.
- A. Drlica-Wagner, A. Albert, K. Bechtol, M. Wood, L. Strigari, M. Sánchez-Conde, L. Baldini, R. Essig, J. Cohen-Tanugi, B. Anderson, et al. Search for Gamma-Ray Emission from DES Dwarf Spheroidal Galaxy Candidates with Fermi-LAT Data. *ApJ*, 809:L4, August 2015. doi: 10.1088/2041-8205/809/1/L4.

- I. Cholis and D. Hooper. Dark matter and pulsar origins of the rising cosmic ray positron fraction in light of new data from the AMS. *Phys. Rev. D*, 88(2):023013, July 2013. doi: 10.1103/PhysRevD.88.023013.
- D. Hooper and T. Linden. Origin of the gamma rays from the Galactic Center. *Phys. Rev. D*, 84(12):123005, December 2011. doi: 10.1103/PhysRevD.84.123005.
- D. Hooper, T. Linden, and P. Mertsch. What does the PAMELA antiproton spectrum tell us about dark matter? *J. Cosmology Astropart. Phys.*, 3:021, March 2015. doi: 10.1088/1475-7516/2015/03/021.
- F. Calore, I. Cholis, C. McCabe, and C. Weniger. A tale of tails: Dark matter interpretations of the Fermi GeV excess in light of background model systematics. *Phys. Rev. D*, 91(6):063003, March 2015. doi: 10.1103/PhysRevD.91.063003.
- M. Regis, S. Colafrancesco, S. Profumo, W. J. G. de Blok, M. Massardi, and L. Richter. Local Group dSph radio survey with ATCA (III): constraints on particle dark matter. *J. Cosmology Astropart. Phys.*, 10:016, October 2014. doi: 10.1088/1475-7516/2014/10/016.
- A. Abramowski, F. Acero, F. Aharonian, A. G. Akhperjanian, G. Anton, A. Barnacka, U. Barres de Almeida, A. R. Bazer-Bachi, Y. Becherini, J. Becker, et al. Search for a Dark Matter Annihilation Signal from the Galactic Center Halo with H.E.S.S. *Physical Review Letters*, 106(16):161301, April 2011. doi: 10.1103/PhysRevLett.106.161301.
- D. Hooper, C. Kelso, and F. S. Queiroz. Stringent constraints on the dark matter annihilation cross section from the region of the Galactic Center. *Astroparticle Physics*, 46:55–70, June 2013. doi: 10.1016/j.astropartphys.2013.04.007.
- G. A. Gomez-Vargas, M. A. Sánchez-Conde, J.-H. Huh, M. Peiró, F. Prada, A. Morselli, A. Klypin, D. G. Cerdeño, Y. Mambrini, and C. Muñoz. Constraints on WIMP annihilation for contracted dark matter in the inner Galaxy with the Fermi-LAT. *J. Cosmology Astropart. Phys.*, 10:029, October 2013a. doi: 10.1088/1475-7516/2013/10/029.
- A. A. Abdo, M. Ackermann, M. Ajello, L. Baldini, J. Ballet, G. Barbiellini, D. Bastieri, K. Bechtol, R. Bellazzini, B. Berenji, et al. Constraints on cosmological dark matter annihilation from the Fermi-LAT isotropic diffuse gamma-ray measurement. *J. Cosmology Astropart. Phys.*, 4:014, April 2010. doi: 10.1088/1475-7516/2010/04/014.
- G. A. Gomez-Vargas, A. Cuoco, T. Linden, M. A. Sanchez-Conde, J. M. Siegal-Gaskins, for the Fermi-LAT Collaboration, T. Delahaye, M. Fornasa, E. Komatsu, F. Prada, and J. Zavala. Dark Matter implications of Fermi-LAT measurement of anisotropies in the diffuse gamma-ray background. *ArXiv e-prints*, March 2013b.
- Z. Hou, H. Zhu, G.-Y. Xiang, C.-F. Li, and G.-C. Guo. Achieving quantum precision limit in adaptive qubit state tomography. *npj Quantum Mechanics*, 2:16001, February 2016. doi: 10.1038/npjqi.2016.1.
- G. Bertone, M. Cirelli, A. Strumia, and M. Taoso. Gamma-ray and radio tests of the e^\pm excess from DM annihilations. *J. Cosmology Astropart. Phys.*, 3:009, March 2009. doi: 10.1088/1475-7516/2009/03/009.

- R. M. Crocker, N. F. Bell, C. Balázs, and D. I. Jones. Radio and gamma-ray constraints on dark matter annihilation in the Galactic center. *Phys. Rev. D*, 81(6):063516, March 2010. doi: 10.1103/PhysRevD.81.063516.
- M. Cirelli and G. Giesen. Antiprotons from Dark Matter: current constraints and future sensitivities. *J. Cosmology Astropart. Phys.*, 4:015, April 2013. doi: 10.1088/1475-7516/2013/04/015.
- A. Dekel and J. P. Ostriker. *in the book: “Formation of Structure in the Universe”, p.135.* April 1999.
- M. Colless, G. Dalton, S. Maddox, W. Sutherland, P. Norberg, S. Cole, J. Bland-Hawthorn, T. Bridges, R. Cannon, C. Collins, W. Couch, N. Cross, K. Deeley, R. De Propris, S. P. Driver, G. Efstathiou, R. S. Ellis, C. S. Frenk, K. Glazebrook, C. Jackson, O. Lahav, I. Lewis, S. Lumsden, D. Madgwick, J. A. Peacock, B. A. Peterson, I. Price, M. Seaborne, and K. Taylor. The 2dF Galaxy Redshift Survey: spectra and redshifts. *MNRAS*, 328:1039–1063, December 2001. doi: 10.1046/j.1365-8711.2001.04902.x.
- D. J. Eisenstein, D. H. Weinberg, E. Agol, H. Aihara, C. Allende Prieto, S. F. Anderson, J. A. Arns, É. Aubourg, S. Bailey, E. Balbinot, and et al. SDSS-III: Massive Spectroscopic Surveys of the Distant Universe, the Milky Way, and Extra-Solar Planetary Systems. *AJ*, 142:72, September 2011. doi: 10.1088/0004-6256/142/3/72.
- E. W. Kolb and M. S. Turner. *The early universe.* 1990.
- A. Liddle. *An Introduction to Modern Cosmology, Second Edition.* May 2003.
- T. Padmanabhan. *Structure Formation in the Universe.* May 1993.
- J. S. Bagla and T. Padmanabhan. Cosmological N-body simulations. *Pramana*, 49:161, August 1997. doi: 10.1007/BF02845853.
- J. E. Gunn and J. R. Gott, III. On the Infall of Matter Into Clusters of Galaxies and Some Effects on Their Evolution. *ApJ*, 176:1, August 1972. doi: 10.1086/151605.
- W. H. Press and P. Schechter. Formation of Galaxies and Clusters of Galaxies by Self-Similar Gravitational Condensation. *ApJ*, 187:425–438, February 1974. doi: 10.1086/152650.
- R. W. Hockney and J. W. Eastwood. *Computer Simulation Using Particles.* 1981.
- G. Efstathiou, M. Davis, S. D. M. White, and C. S. Frenk. Numerical techniques for large cosmological N-body simulations. *ApJS*, 57:241–260, February 1985. doi: 10.1086/191003.
- A. W. Appel. An Efficient Program for Many-Body Simulation. *SIAM Journal on Scientific and Statistical Computing*, vol. 6, no. 1, January 1985, p. 85-103., 6:85–103, January 1985.
- J. Barnes and P. Hut. A hierarchical $O(N \log N)$ force-calculation algorithm. *Nature*, 324:446–449, December 1986. doi: 10.1038/324446a0.
- L. Hernquist. Performance characteristics of tree codes. *ApJS*, 64:715–734, August 1987. doi: 10.1086/191215.

- A. V. Kravtsov, A. A. Klypin, and A. M. Khokhlov. Adaptive Refinement Tree: A New High-Resolution N-Body Code for Cosmological Simulations. *ApJS*, 111:73–94, July 1997. doi: 10.1086/313015.
- E. Bertschinger. Cosmological Perturbation Theory and Structure Formation. *ArXiv Astrophysics e-prints*, December 2001.
- Volker Springel, Simon DM White, Adrian Jenkins, Carlos S Frenk, Naoki Yoshida, Liang Gao, Julio Navarro, Robert Thacker, Darren Croton, John Helly, et al. Simulations of the formation, evolution and clustering of galaxies and quasars. *nature*, 435 (7042):629–636, 2005.
- G. O. Abell. The Distribution of Rich Clusters of Galaxies. *ApJS*, 3:211, May 1958. doi: 10.1086/190036.
- M. Girardi and A. Biviano. Optical Analysis of Cluster Mergers. In L. Feretti, I. M. Gioia, and G. Giovannini, editors, *Merging Processes in Galaxy Clusters*, volume 272 of *Astrophysics and Space Science Library*, pages 39–77, June 2002. doi: 10.1007/0-306-48096-4_2.
- A. Vikhlinin, A. Kravtsov, W. Forman, C. Jones, M. Markevitch, S. S. Murray, and L. Van Speybroeck. Chandra Sample of Nearby Relaxed Galaxy Clusters: Mass, Gas Fraction, and Mass-Temperature Relation. *ApJ*, 640:691–709, April 2006. doi: 10.1086/500288.
- M. Elvis. *MNRAS*, 177:7p, 1976.
- A. Cavaliere and R. Fusco-Femiano. X-rays from hot plasma in clusters of galaxies. *A&A*, 49:137–144, May 1976.
- I. J. Parrish, E. Quataert, and P. Sharma. Anisotropic Thermal Conduction and the Cooling Flow Problem in Galaxy Clusters. *ApJ*, 703:96–108, September 2009. doi: 10.1088/0004-637X/703/1/96.
- C. Jones and W. Forman. Imaging the Hot Intra Cluster Medium. In A. C. Fabian, editor, *NATO Advanced Science Institutes (ASI) Series C*, volume 366 of *NATO Advanced Science Institutes (ASI) Series C*, page 49, 1992.
- M. S. Longair. *High energy astrophysics. Volume 2. Stars, the Galaxy and the interstellar medium.* 1994.
- J. R. Peterson and A. C. Fabian. X-ray spectroscopy of cooling clusters. *Phys. Rep.*, 427:1–39, April 2006. doi: 10.1016/j.physrep.2005.12.007.
- Lieu R. Mittaz J. P. D. Bleeker J. A. M. Mewe R. Colafrancesco S. Kaastra, J. S. and F. J. Lockman. *ApJ*, 519:L119, 1999.
- J. R. Peterson, S. M. Kahn, F. B. S. Paerels, J. S. Kaastra, T. Tamura, J. A. M. Bleeker, C. Ferrigno, and J. G. Jernigan. High-Resolution X-Ray Spectroscopic Constraints on Cooling-Flow Models for Clusters of Galaxies. *ApJ*, 590:207–224, June 2003. doi: 10.1086/374830.
- B. R. McNamara and P. E. J. Nulsen. Heating Hot Atmospheres with Active Galactic Nuclei. *ARA&A*, 45:117–175, September 2007. doi: 10.1146/annurev.astro.45.051806.110625.

- S. Colafrancesco, A. Dar, and A. De Rújula. Cooling flows or warming rays? *A&A*, 413:441–452, January 2004. doi: 10.1051/0004-6361:20031509.
- S. Colafrancesco and P. Marchegiani. Warming rays in cluster cool cores. *A&A*, 484: 51–65, June 2008. doi: 10.1051/0004-6361:20078428.
- C. Ferrari, F. Govoni, S. Schindler, A. M. Bykov, and Y. Rephaeli. Observations of Extended Radio Emission in Clusters. *Space Sci. Rev.*, 134:93–118, February 2008. doi: 10.1007/s11214-008-9311-x.
- L. Feretti, G. Giovannini, F. Govoni, and M. Murgia. Clusters of galaxies: observational properties of the diffuse radio emission. *A&A Rev.*, 20:54, May 2012. doi: 10.1007/s00159-012-0054-z.
- B. M. Deiss, W. Reich, H. Lesch, and R. Wielebinski. The large-scale structure of the diffuse radio halo of the Coma cluster at 1.4GHz. *A&A*, 321:55–63, May 1997.
- H. Liang, R. W. Hunstead, M. Birkinshaw, and P. Andreani. A Powerful Radio Halo in the Hottest Known Cluster of Galaxies 1E 0657-56. *ApJ*, 544:686–701, December 2000. doi: 10.1086/317223.
- M. Bacchi, L. Feretti, G. Giovannini, and F. Govoni. Deep images of cluster radio halos. *A&A*, 400:465–476, March 2003. doi: 10.1051/0004-6361:20030044.
- F. Govoni, T. A. Enßlin, L. Feretti, and G. Giovannini. A comparison of radio and X-ray morphologies of four clusters of galaxies containing radio halos. *A&A*, 369:441–449, April 2001. doi: 10.1051/0004-6361:20010115.
- S. Colafrancesco, M. S. Emritte, N. Mhlahlo, and P. Marchegiani. Multifrequency constraints on the nonthermal pressure in galaxy clusters. *A&A*, 566:A42, June 2014. doi: 10.1051/0004-6361/201321605.
- F. Govoni, C. Ferrari, L. Feretti, V. Vacca, M. Murgia, G. Giovannini, R. Perley, and C. Benoist. Detection of diffuse radio emission in the galaxy clusters A800, A910, A1550, and CL 1446+26. *A&A*, 545:A74, September 2012. doi: 10.1051/0004-6361/201219151.
- D. Ryu, H. Kang, E. Hallman, and T. W. Jones. Cosmological Shock Waves and Their Role in the Large-Scale Structure of the Universe. *ApJ*, 593:599–610, August 2003. doi: 10.1086/376723.
- L. Bravi, M. Gitti, and G. Brunetti. Do radio mini-halos and gas heating in cool-core clusters have a common origin? *MNRAS*, 455:L41–L45, January 2016. doi: 10.1093/mnrasl/slv137.
- M. Murgia, F. Govoni, M. Markevitch, L. Feretti, G. Giovannini, G. B. Taylor, and E. Carretti. Comparative analysis of the diffuse radio emission in the galaxy clusters A1835, A2029, and Ophiuchus. *A&A*, 499:679–695, June 2009. doi: 10.1051/0004-6361/200911659.
- D. Ryu, D. R. G. Schleicher, R. A. Treumann, C. G. Tsagas, and L. M. Widrow. Magnetic Fields in the Large-Scale Structure of the Universe. *Space Sci. Rev.*, 166: 1–35, May 2012. doi: 10.1007/s11214-011-9839-z.
- R. M. Kulsrud and E. G. Zweibel. On the origin of cosmic magnetic fields. *Reports on Progress in Physics*, 71(4):046901, April 2008. doi: 10.1088/0034-4885/71/4/046901.

- A. Neronov and I. Vovk. Evidence for Strong Extragalactic Magnetic Fields from Fermi Observations of TeV Blazars. *Science*, 328:73, April 2010. doi: 10.1126/science.1184192.
- L. Biermann. Über den Ursprung der Magnetfelder auf Sternen und im interstellaren Raum (miteinem Anhang von A. Schläuter). *Zeitschrift Naturforschung Teil A*, 5:65, 1950.
- K. Subramanian, A. Shukurov, and N. E. L. Haugen. Evolving turbulence and magnetic fields in galaxy clusters. *MNRAS*, 366:1437–1454, March 2006. doi: 10.1111/j.1365-2966.2006.09918.x.
- F. F. Gardner and J. B. Whiteoak. Polarization of Radio Sources and Faraday Rotation Effects in the Galaxy. *Nature*, 197:1162–1164, March 1963. doi: 10.1038/1971162a0.
- C. L. Carilli and G. B. Taylor. Cluster Magnetic Fields. *ARA&A*, 40:319–348, 2002. doi: 10.1146/annurev.astro.40.060401.093852.
- K.-T. Kim, P. P. Kronberg, P. E. Dewdney, and T. L. Landecker. The halo and magnetic field of the Coma cluster of galaxies. *ApJ*, 355:29–37, May 1990. doi: 10.1086/168737.
- L. Feretti, D. Dallacasa, G. Giovannini, and A. Tagliani. The magnetic field in the Coma cluster. *A&A*, 302:680, October 1995.
- A. Bonafede, L. Feretti, M. Murgia, F. Govoni, G. Giovannini, D. Dallacasa, K. Dolag, and G. B. Taylor. The Coma cluster magnetic field from Faraday rotation measures. *A&A*, 513:A30, April 2010. doi: 10.1051/0004-6361/200913696.
- Y. Rephaeli. Relativistic electrons in the intracluster space of clusters of galaxies - The hard X-ray spectra and heating of the gas. *ApJ*, 227:364–369, January 1979. doi: 10.1086/156740.
- M. Markevitch, A. H. Gonzalez, L. David, A. Vikhlinin, S. Murray, W. Forman, C. Jones, and W. Tucker. A Textbook Example of a Bow Shock in the Merging Galaxy Cluster 1E 0657-56. *ApJ*, 567:L27–L31, March 2002. doi: 10.1086/339619.
- D. Clowe, M. Bradač, A. H. Gonzalez, M. Markevitch, S. W. Randall, C. Jones, and D. Zaritsky. A Direct Empirical Proof of the Existence of Dark Matter. *ApJ*, 648:L109–L113, September 2006. doi: 10.1086/508162.
- R. Barrena, M. Girardi, and W. Boschin. The puzzling merging cluster Abell 1914: new insights from the kinematics of member galaxies. *MNRAS*, 430:3453–3464, April 2013. doi: 10.1093/mnras/stt144.
- Bullet Cluster. Bullet Cluster, <http://apod.nasa.gov/apod/ap060824.html>, accessed on Friday January 27 09:01:40,. 2017.
- P. Blasi, S. Gabici, and G. Brunetti. Gamma Rays from Clusters of Galaxies. *International Journal of Modern Physics A*, 22:681–706, 2007. doi: 10.1142/S0217751X0703529X.
- P. Blasi and S. Colafrancesco. High energy phenomena in clusters of galaxies. *Nuclear Physics B Proceedings Supplements*, 70:495–499, January 1999. doi: 10.1016/S0920-5632(98)00481-2.

- S. Colafrancesco and P. Blasi. Clusters of galaxies and the diffuse gamma-ray background. *Astroparticle Physics*, 9:227–246, October 1998. doi: 10.1016/S0927-6505(98)00018-8.
- P. Marchegiani, G. C. Perola, and S. Colafrancesco. Testing the cosmic ray content in galaxy clusters. *A&A*, 465:41–49, April 2007. doi: 10.1051/0004-6361:20065977.
- P. Marchegiani and S. Colafrancesco. The role of Dark Matter sub-halos in the non-thermal emission of galaxy clusters. *ArXiv e-prints*, October 2016.
- M. Ackermann, M. Ajello, A. Albert, A. Allafort, W. B. Atwood, L. Baldini, J. Ballet, G. Barbiellini, D. Bastieri, K. Bechtol, et al. Search for Cosmic-Ray-induced Gamma-Ray Emission in Galaxy Clusters. *ApJ*, 787:18, May 2014. doi: 10.1088/0004-637X/787/1/18.
- B. Huber, C. Tchernin, D. Eckert, C. Farnier, A. Manalaysay, U. Straumann, and R. Walter. Probing the cosmic-ray content of galaxy clusters by stacking Fermi-LAT count maps. *A&A*, 560:A64, December 2013. doi: 10.1051/0004-6361/201321947.
- F. Vazza and M. Brüggen. Do radio relics challenge diffusive shock acceleration? *MNRAS*, 437:2291–2296, January 2014. doi: 10.1093/mnras/stt2042.
- F. Vazza, M. Brüggen, D. Wittor, C. Gheller, D. Eckert, and M. Stubbe. Constraining the efficiency of cosmic ray acceleration by cluster shocks. *MNRAS*, 459:70–83, June 2016. doi: 10.1093/mnras/stw584.
- M. Bonamente, R. Lieu, M. K. Joy, and J. H. Nevalainen. The Soft X-Ray Emission in a Large Sample of Galaxy Clusters with the ROSAT Position Sensitive Proportional Counter. *ApJ*, 576:688–707, September 2002. doi: 10.1086/341806.
- S. Bowyer. EUV and Soft X-ray Emission in Clusters of Galaxies. *Journal of Korean Astronomical Society*, 37:295–297, December 2004. doi: 10.5303/JKAS.2004.37.5.295.
- J. N. Bregman and E. J. Lloyd-Davies. On the Lack of a Soft X-Ray Excess from Clusters of Galaxies. *ApJ*, 644:167–173, June 2006. doi: 10.1086/503551.
- R. Lieu, J. P. D. Mittaz, S. Bowyer, J. O. Breen, F. J. Lockman, E. M. Murphy, and C.-Y. Hwang. Diffuse Extreme-Ultraviolet Emission from the Coma Cluster: Evidence for Rapidly Cooling Gases at Submegakelvin Temperatures. *Science*, 274:1335–1338, November 1996. doi: 10.1126/science.274.5291.1335.
- C. L. Sarazin and R. Lieu. Extreme-Ultraviolet Emission from Clusters of Galaxies: Inverse Compton Radiation from a Relic Population of Cosmic Ray Electrons? *ApJ*, 494:L177–L180, February 1998a. doi: 10.1086/311196.
- Y. Rephaeli. On Compton and thermal models for X-ray emission from clusters of galaxies. *ApJ*, 218:323–332, December 1977. doi: 10.1086/155686.
- M. Rossetti and S. Molendi. Is there a hard tail in the Coma Cluster X-ray spectrum? *A&A*, 414:L41–L44, January 2004. doi: 10.1051/0004-6361:20031749.
- D. Eckert, A. Neronov, T. J.-L. Courvoisier, and N. Produit. South-West extension of the hard X-ray emission from the Coma cluster. *A&A*, 470:835–841, August 2007. doi: 10.1051/0004-6361:20077268.

- C. L. Sarazin and R. Lieu. Extreme-Ultraviolet Emission from Clusters of Galaxies: Inverse Compton Radiation from a Relic Population of Cosmic Ray Electrons? *ApJ*, 494:L177–L180, February 1998b. doi: 10.1086/311196.
- T. A. Enßlin, R. Lieu, and P. L. Biermann. Non-thermal origin of the EUV and HEX excess emission of the Coma cluster - the nature of the energetic electrons. *A&A*, 344: 409–420, April 1999.
- C. L. Sarazin and J. C. Kempner. Nonthermal Bremsstrahlung and Hard X-Ray Emission from Clusters of Galaxies. *ApJ*, 533:73–83, April 2000. doi: 10.1086/308649.
- P. Blasi. Stochastic Acceleration and Nonthermal Radiation in Clusters of Galaxies. *ApJ*, 532:L9–L12, March 2000. doi: 10.1086/312551.
- V. Petrosian. On the Nonthermal Emission and Acceleration of Electrons in Coma and Other Clusters of Galaxies. *ApJ*, 557:560–572, August 2001. doi: 10.1086/321557.
- M. Ajello, P. Rebusco, N. Cappelluti, O. Reimer, H. Böhringer, J. Greiner, N. Gehrels, J. Tueller, and A. Moretti. Galaxy Clusters in the Swift/Burst Alert Telescope Era: Hard X-rays in the Intracluster Medium. *ApJ*, 690:367–388, January 2009. doi: 10.1088/0004-637X/690/1/367.
- F. Gastaldello, D. R. Wik, S. Molendi, N. J. Westergaard, A. Hornstrup, G. Madejski, D. D. M. Ferreira, S. E. Boggs, F. E. Christensen, W. W. Craig, et al. A NuSTAR Observation of the Center of the Coma Cluster. *ApJ*, 800:139, February 2015. doi: 10.1088/0004-637X/800/2/139.
- R. A. Sunyaev and Y. B. Zeldovich. Small-Scale Fluctuations of Relic Radiation. *Ap&SS*, 7:3–19, April 1970. doi: 10.1007/BF00653471.
- S. Colafrancesco, P. Marchegiani, and E. Palladino. The non-thermal Sunyaev-Zel'dovich effect in clusters of galaxies. *A&A*, 397:27–52, January 2003. doi: 10.1051/0004-6361:20021199.
- S. Colafrancesco, P. Marchegiani, and R. Buonanno. Untangling the atmosphere of the Bullet cluster with Sunyaev-Zel'dovich effect observations. *A&A*, 527:L1, March 2011b. doi: 10.1051/0004-6361/201016037.
- S. Colafrancesco, P. Mazzotta, Y. Rephaeli, and N. Vittorio. Cosmic microwave background anisotropy induced by gas in clusters of galaxies. *ApJ*, 433:454–463, October 1994. doi: 10.1086/174657.
- S. Colafrancesco, P. Mazzotta, and N. Vittorio. Is the Cluster Temperature Function a Reliable Test for Ω_0 ? *ApJ*, 488:566–571, October 1997. doi: 10.1086/304749.
- M. Birkinshaw. The Sunyaev-Zel'dovich effect: an update. In L. Maiani, F. Melchiorri, and N. Vittorio, editors, *3K cosmology*, volume 476 of *American Institute of Physics Conference Series*, pages 298–309, May 1999. doi: 10.1063/1.59334.
- J. E. Carlstrom, M. Joy, L. Grego, G. Holder, W. L. Holzapfel, S. LaRoque, J. J. Mohr, and E. D. Reese. The Sunyaev-Zel'dovich Effect: Results and Future Prospects. *ArXiv Astrophysics e-prints*, March 2001.
- S. Colafrancesco, P. Marchegiani, P. de Bernardis, and S. Masi. A multi-frequency study of the SZE in giant radio galaxies. *A&A*, 550:A92, February 2013. doi: 10.1051/0004-6361/201117376.

- S. Colafrancesco and P. Marchegiani. On the ability of the spectroscopic Sunyaev-Zeldovich effect measurements to determine the temperature structure of galaxy clusters. *A&A*, 520:A31, September 2010. doi: 10.1051/0004-6361/200913115.
- D. A. Prokhorov and S. Colafrancesco. The first measurement of temperature standard deviation along the line of sight in galaxy clusters. *MNRAS*, 424:L49–L53, July 2012. doi: 10.1111/j.1745-3933.2012.01284.x.
- M. Shehzad Emritte, S. Colafrancesco, and P. Marchegiani. Polarization of the Sunyaev-Zel'dovich effect: relativistic imprint of thermal and non-thermal plasma. *J. Cosmology Astropart. Phys.*, 7:031, July 2016. doi: 10.1088/1475-7516/2016/07/031.
- S. Colafrancesco, P. Marchegiani, and M. S. Emritte. Probing the physics and history of cosmic reionization with the Sunyaev-Zel'dovich effect. *A&A*, 595:A21, October 2016. doi: 10.1051/0004-6361/201424904.
- L. Feretti, C. Burigana, and T. A. Enßlin. Diffuse radio emission from the intracluster medium. *New A Rev.*, 48:1137–1144, December 2004. doi: 10.1016/j.newar.2004.09.025.
- T. A. Ensslin, P. L. Biermann, P. P. Kronberg, and X.-P. Wu. Cosmic-Ray Protons and Magnetic Fields in Clusters of Galaxies and Their Cosmological Consequences. *ApJ*, 477:560–567, March 1997.
- H. J. Völk, F. A. Aharonian, and D. Breitschwerdt. The Nonthermal Energy Content and Gamma-Ray Emission of Starburst Galaxies and Clusters of Galaxies. *Space Sci. Rev.*, 75:279–297, January 1996. doi: 10.1007/BF00195040.
- H. J. Völk and A. M. Atoyan. Early Starbursts and Magnetic Field Generation in Galaxy Clusters. *ApJ*, 541:88–94, September 2000. doi: 10.1086/309395.
- P. C. Tribble. Radio haloes, cluster mergers, and cooling flows. *MNRAS*, 263:31–36, July 1993. doi: 10.1093/mnras/263.1.31.
- L. O. Drury. An introduction to the theory of diffusive shock acceleration of energetic particles in tenuous plasmas. *Reports on Progress in Physics*, 46:973–1027, August 1983. doi: 10.1088/0034-4885/46/8/002.
- R. Blandford and D. Eichler. Particle acceleration at astrophysical shocks: A theory of cosmic ray origin. *Phys. Rep.*, 154:1–75, October 1987. doi: 10.1016/0370-1573(87)90134-7.
- W. J. Jaffe. Upper limits on nuclear radio emission from some Coma cluster spirals. *ApJ*, 216:212, August 1977. doi: 10.1086/155463.
- G. Brunetti. Modelling the Non-Thermal Emission from Galaxy Clusters. In S. Bowyer and C.-Y. Hwang, editors, *Matter and Energy in Clusters of Galaxies*, volume 301 of *Astronomical Society of the Pacific Conference Series*, page 349, 2003.
- B. Wolfe and F. Melia. Covariant Kinetic Theory with an Application to the Coma Cluster. *ApJ*, 638:125–137, February 2006. doi: 10.1086/498227.
- F. Miniati, T. W. Jones, H. Kang, and D. Ryu. Cosmic-Ray Electrons in Groups and Clusters of Galaxies: Primary and Secondary Populations from a Numerical Cosmological Simulation. *ApJ*, 562:233–253, November 2001a. doi: 10.1086/323434.

- T. A. Ensslin, P. L. Biermann, U. Klein, and S. Kohle. Cluster radio relics as a tracer of shock waves of the large-scale structure formation. *A&A*, 332:395–409, April 1998.
- G. Brunetti, G. Setti, L. Feretti, and G. Giovannini. Particle reacceleration in the Coma cluster: radio properties and hard X-ray emission. *MNRAS*, 320:365–378, January 2001. doi: 10.1046/j.1365-8711.2001.03978.x.
- Y. Fujita, M. Takizawa, and C. L. Sarazin. Nonthermal Emissions from Particles Accelerated by Turbulence in Clusters of Galaxies. *ApJ*, 584:190–202, February 2003. doi: 10.1086/345599.
- E. Fermi. On the Origin of the Cosmic Radiation. *Physical Review*, 75:1169–1174, April 1949. doi: 10.1103/PhysRev.75.1169.
- G. Brunetti, P. Blasi, O. Reimer, L. Rudnick, A. Bonafede, and S. Brown. Probing the origin of giant radio haloes through radio and γ -ray data: the case of the Coma cluster. *MNRAS*, 426:956–968, October 2012. doi: 10.1111/j.1365-2966.2012.21785.x.
- G. Brunetti, P. Blasi, R. Cassano, and S. Gabici. Alfvénic reacceleration of relativistic particles in galaxy clusters: MHD waves, leptons and hadrons. *MNRAS*, 350:1174–1194, June 2004. doi: 10.1111/j.1365-2966.2004.07727.x.
- B. Dennison. Formation of radio halos in clusters of galaxies from cosmic-ray protons. *ApJ*, 239:L93–L96, August 1980. doi: 10.1086/183300.
- V. S. Berezinsky, P. Blasi, and V. S. Ptuskin. Clusters of Galaxies as Storage Room for Cosmic Rays. *ApJ*, 487:529–535, October 1997. doi: 10.1086/304622.
- F. Miniati, D. Ryu, H. Kang, and T. W. Jones. Cosmic-Ray Protons Accelerated at Cosmological Shocks and Their Impact on Groups and Clusters of Galaxies. *ApJ*, 559:59–69, September 2001b. doi: 10.1086/322375.
- T. Enßlin, C. Pfrommer, F. Miniati, and K. Subramanian. Cosmic ray transport in galaxy clusters: implications for radio halos, gamma-ray signatures, and cool core heating. *A&A*, 527:A99, March 2011. doi: 10.1051/0004-6361/201015652.
- G. Giovannini, M. Tordi, and L. Feretti. Radio halo and relic candidates from the NRAO VLA Sky Survey. *New A*, 4:141–155, March 1999. doi: 10.1016/S1384-1076(99)00018-4.
- S. Colafrancesco and B. Mele. Neutralinos and the Origin of Radio Halos in Clusters of Galaxies. *ApJ*, 562:24–41, November 2001. doi: 10.1086/323427.
- M. A. Pérez-Torres, F. Zandanel, M. A. Guerrero, S. Pal, S. Profumo, F. Prada, and F. Panessa. The origin of the diffuse non-thermal X-ray and radio emission in the Ophiuchus cluster of galaxies. *MNRAS*, 396:2237–2248, July 2009. doi: 10.1111/j.1365-2966.2009.14883.x.
- R. Gavazzi, C. Adami, F. Durret, J.-C. Cuillandre, O. Ilbert, A. Mazure, R. Pelló, and M. P. Ulmer. A weak lensing study of the Coma cluster. *A&A*, 498:L33–L36, May 2009. doi: 10.1051/0004-6361/200911841.
- N. Okabe, T. Futamase, M. Kajisawa, and R. Kuroshima. Subaru Weak-lensing Survey of Dark Matter Subhalos in the Coma Cluster: Subhalo Mass Function and Statistical Properties. *ApJ*, 784:90, April 2014. doi: 10.1088/0004-637X/784/2/90.

- F. Prada, A. A. Klypin, A. J. Cuesta, J. E. Betancort-Rijo, and J. Primack. Halo concentrations in the standard Λ cold dark matter cosmology. *MNRAS*, 423:3018–3030, July 2012. doi: 10.1111/j.1365-2966.2012.21007.x.
- E. Komatsu, K. M. Smith, J. Dunkley, C. L. Bennett, B. Gold, G. Hinshaw, N. Jarosik, D. Larson, M. R. Nolta, L. Page, D. N. Spergel, M. Halpern, R. S. Hill, A. Kogut, M. Limon, S. S. Meyer, N. Odegard, G. S. Tucker, J. L. Weiland, E. Wollack, and E. L. Wright. Seven-year Wilkinson Microwave Anisotropy Probe (WMAP) Observations: Cosmological Interpretation. *ApJS*, 192:18, February 2011. doi: 10.1088/0067-0049/192/2/18.
- A. Klypin, A. V. Kravtsov, J. S. Bullock, and J. R. Primack. Resolving the Structure of Cold Dark Matter Halos. *ApJ*, 554:903–915, June 2001. doi: 10.1086/321400.
- V. Springel. The cosmological simulation code GADGET-2. *MNRAS*, 364:1105–1134, December 2005. doi: 10.1111/j.1365-2966.2005.09655.x.
- V. Springel and L. Hernquist. Cosmological smoothed particle hydrodynamics simulations: a hybrid multiphase model for star formation. *MNRAS*, 339:289–311, February 2003. doi: 10.1046/j.1365-8711.2003.06206.x.
- P. Gondolo and G. Gelmini. Cosmic abundances of stable particles: improved analysis. *Nuclear Physics B*, 360:145–179, August 1991. doi: 10.1016/0550-3213(91)90438-4.
- V. Springel. Smoothed Particle Hydrodynamics in Astrophysics. *ARA&A*, 48:391–430, September 2010. doi: 10.1146/annurev-astro-081309-130914.
- P. Gondolo, J. Edsjö, P. Ullio, L. Bergström, M. Schelke, and E. A. Baltz. DarkSUSY: computing supersymmetric dark matter properties numerically. *J. Cosmology Astropart. Phys.*, 7:008, July 2004. doi: 10.1088/1475-7516/2004/07/008.
- M. Ackermann, M. Ajello, A. Albert, W. B. Atwood, L. Baldini, J. Ballet, G. Barbiellini, D. Bastieri, K. Bechtol, R. Bellazzini, et al. Search for Gamma-Ray Emission from the Coma Cluster with Six Years of Fermi-LAT Data. *ApJ*, 819:149, March 2016. doi: 10.3847/0004-637X/819/2/149.
- M. Markevitch, A. H. Gonzalez, D. Clowe, A. Vikhlinin, W. Forman, C. Jones, S. Murray, and W. Tucker. Direct Constraints on the Dark Matter Self-Interaction Cross Section from the Merging Galaxy Cluster 1E 0657-56. *ApJ*, 606:819–824, May 2004. doi: 10.1086/383178.
- P. S. Behroozi, R. H. Wechsler, and H.-Y. Wu. The ROCKSTAR Phase-space Temporal Halo Finder and the Velocity Offsets of Cluster Cores. *ApJ*, 762:109, January 2013. doi: 10.1088/0004-637X/762/2/109.
- Y.-P. Wang, K.-K. Duan, P.-X. Ma, Y.-F. Liang, Z.-Q. Shen, S. Li, C. Yue, Q. Yuan, J.-J. Zang, Y.-Z. Fan, and J. Chang. Testing the dark matter subhalo hypothesis of the gamma-ray source 3FGL J 2212.5 +0703. *Phys. Rev. D*, 94(12):123002, December 2016. doi: 10.1103/PhysRevD.94.123002.